REPAIR WELDING MANUAL

Welding Institute of Canada
Institut de Soudage du Canada

WELDING INSTITUTE OF CANADA
INSTITUT DE SOUDAGE DU CANADA

CONTRACT SERIAL NUMBER OSR84-00219
CONTRACT REQUISITION NUMBER 23440-4-9270
CONTRACTOR: WELDING INSTITUTE OF CANADA

FUNDAMENTAL STUDY OF HAZ CORROSION: THE EFFECT OF MICROSTRUCTURE

Welding Institute of Canada Report RC213

"Purchase of a Subscription to a Limited Edition of a series of Reports on an Evaluation of Steels, Welding Consumables and Procedures for optimum corrosion behaviour in Arctic Marine Application".

DSS Serial No. DSQ84-00219
DSS File No. 5SQ - 23440 - 4 - 9270
WIC Ref. RC 213

Prepared by: Dr. S.R. Bala
Dr. T.W. Lau
September 1988

MICROMEDIA

10899

HEAD OFFICE / SIEGE SOCIAL: 391 Burnhamthorpe Road East, Oakville, Ont. L6J 6C9 — Ph: (416) 845-9881 Fax: (416) 845-9886
CENTRE DU QUEBEC / QUEBEC CENTRE: 2399 rue de la Province, Longueuil, Que. J4G 1G3 — Ph: (514) 651-5086 Fax: (514) 651-5089

ACKNOWLEDGEMENT

This was a 50/50 Government (DSS) funded project and has been managed by the Welding Institute of Canada. The corrosion testing of the weldments and Gleeble specimens has been subcontracted out to University of Toronto and carried out at the Department of Metallurgy and Materials science (Prof. K.T. Aust and Prof. G.C. Weatherly, the principal investigators). Gratitude is in order to our sponsors: Nippon Steel U.S.A. Inc. (Mr. N. Taniguchi), Stelco Inc., (Mr. D.B. McCutcheon) and the Algoma Steel Corp. Ltd. (Mr. M. McLean). Thanks are also due to Messrs. Ian Montgomery and Mike Irvine for their technical help, Dr. J. Bowker and Mr. Murray Letts of CANMET for Gleeble treatment as well as Mrs. Catherine Neal and Mrs. Kathy Smith for putting this report together.

TABLE OF CONTENTS

		Page
1.0	Introduction	1
1.1	Scope	1
2.0	Review of the Relevant Literature	1
2.1	Corrosion of C-Mn Steel Weldments	1
3.0	Experimental Procedure	5
3.1	Materials Processing	5
3.2	Welding of the Base Materials	6
3.3	Gleeble Specimen Preparation	6
3.4	Microstructure Characterization	6
3.5	Corrosion Tests	8
	3.5.1 The Constant Potential Anodic Dissolution Tests	8
	3.5.2. Microelectrode Tests	10
4.0	Results	11
4.1	Microstructural Characterization	11
4.2	Corrosion Tests	12
	4.2.1 Four Day Constant Potential Tests	12
	4.2.1.a Results of Weldment	12
	4.2.1.b Results of Gleeble Samples	14
4.3	Microelectrode Experiments	15
	4.3.1 Summary of Microelectrode Experimental Results	18
5.0	Discussion	19
5.1	Metallography and Effects of Microstructure	19
5.2	Chemistry Effect	20
5.3	The Gleeble Specimens	23
5.4	Analysis of Factorial Experiments	24
5.5	Micro-Electrode Experiments	25
6.0	Summary and Conclusions	26
7.0	Recommendations	27
8.0	References	27

LIST OF TABLES

Table 1 Table of Steel Composition

Table 2 Table of Welding Parameters

Table 3a Quantitative Microstructural Analysis at the Fusion Line (1 kJ/mm)

Table 3b Quantitative Microstructural Analysis at the Mid-Point of HAZ (1 kJ/mm)

Table 3c Quantitative Microstructural Anlaysis at the A_{c1} Region of HAZ (1 kJ/mm)

Table 4a Quantitative Microstructural Analysis at the Fusion Line (3 kJ/mm)

Table 4b Quantitative Microstructural Analysis at the Mid-Point of HAZ (3 kJ/mm)

Table 4c Quantitative Microstructural Anlaysis at the A_{c1} Region of HAZ (3 kJ/mm)

Table 5 Summary of Available Grain Size Numbers at the Fusion Line of the HAZ

Table 6a Quantitative Microstructural Analysis of Central Region of Gleeble Samples

Table 6b Quantitative Microstructural Analysis of Gleeble Samples: Mid-point Region of Transformed Zone (5 s)

Table 6c Quantitative Microstructural Analysis: Gleeble, Edge of Transformed Zone (5 s)

Table 7a Quantitative Microstructural Analysis of the Gleeble Samples: Central Region (20s)

Table 7b Quantitative Microstructural Analysis of Gleeble Samples: Mid point region (20s)

Table 7c Quantitative Microstructural Anlaysis of Gleeble Samples: Edge of Transformed Zone (20 s)

Table 8a Quantitative Microstructural Analysis (128 s)

Table 8b Quantitative Microstructural Analysis Gleeble Sample: Mid Point (128 s)

Table 8c Quantitative Microstructural Anlaysis Edge of Gleeble (128 s)

Table 9 Summary of Grain Size Measurements (20 s)

Table 10 Summary of Grain Size Measurements (128 s)

Table 11 Microstructure and Corrosion Groove Depth of HAZ

Table 12 Summary of Corrosion Results of the Gleeble Simulated Samples

LIST OF FIGURES

Figure 1. Showing three types of Weldment corrosion a) Weld metal corrosion, b) HAZ corrosion, c) fusion line attack.

Figure 2. Showing the effect of Mn and heat input on HAZ corrosion on various C-Mn steels (after Saarinen (2)).

Figure 3. Typical microstructures in Gleeble sample of steel 1 (t_{8-5} = 20 s), Mag. 200 X.

Figure 4. Typical microstructures observed in HAZ of steel 3 at 3 kJ/mm heat input, Mag. 500 X.

Figure 5. Typical microstructures observed in steel 1 Gleeble sample (t_{8-5} = 20 s) Mag. 750 X.

Figure 6. Typical microstructures observed in steel 8 Gleeble samples (t_{8-5} = 5 s) Mag. 250 X.

Figure 7. Typical microstructures observed in steel 1, Gleeble sample (t_{8-5} = 5 s). Mag. 250 X.

Figure 8. Typical microstructures observed at edge of HAZ, steel 1, heat input = 3 kJ/mm. Mag 1000 X.

Figure 9. Experimental apparatus used in Micro-electrode testing.

Figure 10a. As-corroded 1 - 1 kJ/mm (40x).

Figure 10b. Microstructure of Region A of Figure 10a for 1-1kJ/mm (500 X).

Figure 11a. As-corroded 1-3 kJ/mm (40X).

Figure 11b. Microstructure of the grain growth region A for 1-3 kJ/mm (200 X).

Figure 12a. As-corroded 1a-1 kJ/mm (40 X).

Figure 12b. As-corroded 1a - 3 kJ/mm (40 X).

Figure 13a. As-corroded 3-1 kJ/mm (40 X).

Figure 13b. Microstructure of Region A of Figure 13a (500 X).

Figure 14a. As-corroded 3-3kJ/mm (40 X)

Figure 14b. Microstructure of Region A of Figure 14a for 3-3 kJ/mm (200 X).

Figure 15a. As-corroded 3a-1 kJ/mm (40 X).

Figure 15b. As-corroded 3a-3kJ/mm (40 X).

Figure 16a. As-corroded 5-1 kJ/mm (40 X).

Figure 16b. Microstructure of Region A of Figure 16a for 5-1 kJ/mm (500 X).

Figure 17a. As-corroded 5-3 kJ/mm (40 X).

Figure 17b. Microstructure of Region A of Figure 17a for 5-3 kJ/mm (500 X).

Figure 18a. As-corroded 7-1 kJ/mm (40 X).

Figure 18b. Microstructure of Region A of Figure 18a for 7-1 kJ/mm (500 X).

Figure 19a. As-corroded 7-3 kJ/mm (40 X).

Figure 19b. Microstructure of Region A of Figure 19a for 7-3 kJ/mm (500 X)

Figure 20a. As-corroded 6-1 kJ/mm (40 X).

Figure 20b. Microstructure of Region A of Figure 20a for 6-1 kJ/mm (500 X).

Figure 21a. As-corroded 6-3 kJ/mm (40 X).

Figure 21b. Microstructure of Region B of Figure 21a for 6-3 kJ/mm (500 X).

Figure 22a. As-corroded 8-1 kJ/mm (40 X).

Figure 22b. Microstructure of Region A of Figure 22a for 8-1 kJ/mm (500 X).

Figure 23a. As-corroded 8-3 kJ/mm (40 X).

Figure 23b. Microstructure of Region B of Figure 23a for 8-3 kJ/mm (500 X).

Figure 24a. As-corroded 2-1 kJ/mm (40 X).

Figure 24b. Microstructure of Region A of Figure 24a for 2-1 kJ/mm (500 X).

Figure 25a. As-corroded 2-3 kJ/mm (16 X).

Figure 25b. Microstructure of Region A of Figure 25a for 2-3 kJ/mm (500 X).

Figure 26a. As-corroded 4-1 kJ/mm (40 X).

Figure 26b. Microstructure of Region A of Figure 26a for 4-1 kJ/mm (500 X).

Figure 27a. As-corroded 4-3 kJ/mm (40 X).

Figure 27b. Microstructure of region A of Figure 27a for 4-3 kJ/mm (500 X).

Figure 28. Gleeble specimen profile after corrosion. Sample 3-20s. Specimen checked longitudinally (for 50 mm), at a randomly selected circumference (50 X).

Figure 29. Gleeble specimen profile after corrosion - Sample 4 - 20s. Specimen checked longitudinally (for 50 mm) at a randomly selected circumference (50 X).

Figure 30. Profile of Gleeble specimen after corrosion - Sample 8-20s. Specimen checked longitudinally (for 50 mm) at a randomly selected circumference (50 X).

Figure 31. Position/Potential profile of weldment 1a-1 kJ/mm, as a function of weldment potential (vSCE) in 0.5 N NaCl.

Figure 32. Position/Potential profile of weldment 3a-1 kJ/mm, as a function of Weldment potential (vSCE) in 0.5 N NaCl.

Figure 33. Position/Potential profile of weldment 1a-3 kJ/mm, as a function of Weldment potential (vSCE) in 0.5 N NaCl.

Figure 34. Position/Potential profile of Weldment 3a-3 kJ/mm, as a function of weldment potential (vSCE) in 0.5 N NaCl.

Figure 35. Position/Potential profile of weldment 3-1 kJ/mm as a function of time at a Weldment potential of -500 (vSCE) in 0.5 N NaCl. Δ -2 hours, + -4 hours, * -6 hours, ◘ - 8 hours.

Figure 36. Position/Potential profile of weldment 4-1 kJ/mm as a function of time at a Weldment potential of -500 mV (vSCE) in 0.5 N NaCl. Δ -2 hours, + -4 hours, * -8 hours, ◘ -12 hours, x -24 hours.

Figure 37. Graph of total current leaving the specimen versus time for weldment 2-1 kJ/mm at a potential of -600 mV (vSCE).

Figure 38a. Position/Potential profile of weldment 2-1 kJ/mm as a function of time at a potential of -600 mV (vSCE) in 0.5 N NaCl. Δ- 2 hours, + -4 hours, * -8 hours, ◘ -12 hours, x -24 hours.

Figure 38b. Position/Potential profile of weldment 2-1 kJ/mm as a function of time at a potential of -600 mV (vSCE) in 0.5 N NaCl. □ - 48 hours, ◊ -72 hours, ◙ - 96 hours, ◘ - 120 hours, 1 - 146 hours.

Figure 39. Graph of total current leaving the specimen versus time for weldment 7-3 kJ/mm at a potential of 600 mV.

Figure 40a. Position/Potential profile of weldment 7-3 a function of time at a potential of -600 mV (vSCE) in 0.5 N NaCl. Δ- 2 hours, + - 4 hours, * -8 hours, ◘ - 12 hours.

Figure 40b. Position/Potential profile of weldment 7-3 kJ/mm as a function of time at a potential of -600 mV (vSCE) in 0.5 N NaCl. ◊ - 72 hours, ◙ - 96 hours, ◘ - 120 hours.

Figure 41. Schematic diagram of the surface of specimen 7-3 kJ/mm a) after 8 hours, b) 48 hours at a potential of -600 mV (vSCE) in 0.5 N NaCl.

Figure 42. Graph of total current versus time for weldment 5-1 kJ/mm at a potential of -600 mV (vSCE) in 0.5 N NaCl.

Figure 43a. Position/Potential profile as a function of time for weldment 5-1 kJ/mm at a potential of -600 mV (vSCE) in 0.5 N NaCl * - 8 hours, ◘ - 12 hours, x - 24 hours.

Figure 43b. Position/Potential profile for weldment 5-1 kJ/mm after 72 hours exposure at a potential of -600 mV in 0.5 N NaCl.

Figure 44. Position/Potential profile as a function of time for weldment 4-1 kJ/mm at a potential of -600 mV (vSCE) in 0.5 N NaCl. ▲ - 2 hours,, + - 4 hours, * - 8 hours, ◘ - 12 hours, x - 24 hours.

Figure 45. Position/Potential profile as a function of time for weldment 6-1 kJ/mm at a potential of -600 mV (vSCE) in 0.5 N NaCl. ▲- 2 hours, + - 4 hours, * - 8 hours, ◘ - 12 hours, x - 24 hours.

Figure 46. Position/Potential profile as a function of time for weldment 7-1 kJ/mm at a potential of -600 mV (vSCE) in 0.5 N NaCl. ▲- 2 hours, + - 4 hours, * - 8 hours, ◘ - 12 hours, x - 24 hours.

Figure 47. Position/Potential profile as a function of time for weldment 8-3 kJ/mm at a potential of -600 mV (vSCE) in 0.5 N NaCl. ▲- 2 hours, + - 4 hours, * - 8 hours, ◘ - 12 hours, x - 24 hours.

Figure 48a. As-corroded annealed 8-1 kJ/mm (40 X).

Figure 48b. Microstructure of Region A of Figure 48a for annealed 8-1 kJ/mm (200 X).

Figure 49. Graph of Mn Enrichment + 4*Nb Enrichment, assuming total dissolution of Nb(CN) in the lower carbon steels.

ABSTRACT

The effect of HAZ microstructure and base plate composition on HAZ corrosion was investigated in 0.5 N NaCl solution using micro-electrode and four day constant potential anodic dissolution testing. It was determined that there was no systematic effect of microstructure of the coarse grain region on HAZ corrosion. However, increasing the Mn content in all the steels tested increased the depth of the corrosion groove in the HAZ. Nb additions to the higher carbon (.12 wt%) steel had little effect on the HAZ corrosion in the weldments but increased the HAZ corrosion in the lower carbon (.06 wt%) steel weldments. It seemed possible that C is playing a role in tying portions of the HAZ, Mn or/and Nb allowing the excess of the latter elements to be dissolved in the ferrite phase. It was postulated that severe HAZ corrosion is the result of soluble Mn and Nb enrichment in the ferrite phase in the HAZ. The effect of heat input was to generally decrease the HAZ corrosion in the weldments as the HI increased.

FUNDAMENTAL STUDY OF HAZ CORROSION: THE EFFECT OF MICROSTRUCTURE

Welding Institute of Canada Report RC213

1.0 Introduction

It is generally accepted that the corrosion of steel in neutral environments is limited by oxygen diffusion and that the composition and microstructure of a C steel has little effect on the corrosion behaviour. One form of localized dissolution that occurs in the region around a weld is known as heat affected zone (HAZ) corrosion. However, microstructure and compositional effects may be important in such localized corrosion. This is particularly a serious problem in ice breakers in that the abrasion caused by the ice makes cathodic protection and coating schemes difficult.

1.1 Scope

The aim of this program was to determine the effect of base plate composition and HAZ microstructure on the HAZ corrosion behaviour of C-Mn steels. Thus, corrosion experiments were performed on actual weldments and Gleeble simulated specimens. The actual weldments were bead-on-plate welds prepared using filler materials containing 3% Ni to ensure that the weld metal was more noble. Gleeble simulated specimens eliminated the effects of the weld metal composition. Hence, by comparing the Gleeble specimens and the actual weldment, the importance of microstructures could be evaluated.

44n

2.0 Review of the Relevant Literature

2.1 Corrosion of C-Mn Steel Weldments

Three types of weldment corrosion have been classified as shown in Figure 1 (1). The first type is the selective corrosion of the weld metal (see Figure 1A). The second, (Figure 1B) is

the preferential dissolution of the HAZ. The third, (Figure 1C) is fusion line attack. Of these three, the preferential corrosion of the HAZ is the least understood. Selective corrosion of the weld metal is accepted as being caused by a lower corrosion potential of the weld metal, which can be overcome by alloying the filler metal with more noble metals such as Ni or Cu. Fusion line attack was the result of active Mn(Fe)S segregation into the fusion zone of the HAZ. The solution for this problem was either to reduce the S level or to bind the S with elements such as Ce, Ti, and Zr (1).

HAZ corrosion has been attributed both to microstructure (1, 2, 3) as well as to the composition of the protective oxide (4). According to Saarinen (3) the corrosion susceptibility of the HAZ was increased in ship building steels when austenite decomposed in the HAZ at low temperatures. He proposed that the rate of the HAZ corrosion in sea water was high when, the Mn content was high, the heat input was low, and/or the welding temperature was low. Figure 2 shows the effect of Mn on the HAZ corrosion of various steels with a carbon content ranging from 0.13-0.18 wt% after rotating for three months in a tank containing artificial sea water (2). Saarinen (2) pointed out that those heat affected zones which corroded at a high rate contained large uniform areas of martensite and lower bainite, or areas of upper bainite.

Adrain et al (5) supported Saarien's view having stated that corrosion of the HAZ was attributable to metastable structures. Lundin and Utterberg (6) have stated that the worst corrosion resistance was exhibited by a microstructure which consisted of either untempererd high carbon martensite or high carbon retained austenite in a ferrite matrix. The high carbon martensite acted as a local cathode contributing to the localized corrosion (6). Raty and co-workers (7) used a current ratio test. They hypothesized that HAZ corrosion susceptibility was the result of "quenched in" carbon in the ferrite lattice (7). The term quenched in carbon refers to the excess carbon in solution in the ferrite phase when compared to a slowly cooled microstructure. The effect of Mn was therefore indirect since it tended to increase the amount of "quenched in" carbon in ferrite.

Backman and co-workers (8) tested several combinations of C-Mn steels and weld metal compositions. They found that either the weld metal corrosion or HAZ corrosion depended on

the combination choice of weld metal and parent plate. Ing and Steffens (9) determined that the presence of a fine grained zone in the HAZ appeared to have contributed to a lowering of the resistance to corrosion in their specimens. They used a micro-corrosion technique and found that the potential of the HAZ was more negative than either the weld metal or the base material. Consequently, local cells formed in the HAZ. These electronegative constituents corroded preferentially (9).

Strommen (10) galvanically coupled martensitic microstructures with various steels having a ferrite/pearlite microstructure. The corrosion was observed to have initiated as pitting on both electrodes of the couples. However, the corrosion rate of active martensite microstructures was increased by galavincally coupling them to ferrite/pearlite structures. They also observed that a change in polarity occurred in many of the couples; the martensitic structure initially behaved cathodically then changed to anodic behaviour (10).

Itoh and co-workers (4) determined that the effect of microstructure on the HAZ corrosion of bainitic type steels was weak. They suggested that the Cu and Ni existing in the weld material, concentrated in the oxide and facilitated the formation of tighter corrosion products; this made the weld material more noble. This in turn created the proper electrochemical conditions for HAZ corrosion. From regression analysis of the samples tested in their work they proposed that if the following equation was negative HAZ corrosion would occur, if positive weld metal corrosion would occur.

E_e = dCu*3.8 + dNi*1.1 + 0.3

dCu: difference in Cu content between the base metal and weld metal (Cu plate - Cu weld)

dNi: difference in Ni content between the base metal and weld metal (Ni plate - Ni weld)

Chernov and Chichkin (11) mathematically modeled the corrosion current distribution over the surface of a welded joint. They assumed discrete values of corrosion potential in each of the weld seam, heat affected zone, and parent metal. Solving Laplace's Equation, they determined the corrosion current distribution over the surface of the weldment as follows:

$$i(x) = \frac{\phi_{HAZ} - \phi_S}{\alpha \Pi} \left[f(X_1) + f(X_2) \right]$$

$$- \frac{\phi_{HAZ}}{\alpha \Pi} \left[f(X_3) + f(X_4) \right]$$

where $X_1 = \frac{x_S - x}{\alpha \delta}$, $X_2 = \frac{x_{HAZ} + x}{\alpha \delta}$

$$X_3 = \frac{x_{HAZ} - x}{\alpha \delta}, \quad X_4 = \frac{x_{HAZ} + x}{\alpha \delta}$$

$$f(x) = \cos x \int_x^\infty \frac{\sin z}{z} dz - \sin x \int_x^\infty \frac{\cos z}{z} dz.$$

The parameters of importance were, the polarizability coefficient *a*, the potentials of the weld seam ϕ, and of the HAZ ϕ_{HAZ}, (the potential of the plate was taken as zero), position on the surface x, and the conductivity of the electrolyte σ.

An anodic region in the HAZ will be promoted if ϕ, > ϕ_{HAZ} as well as an increase in the size of the weld seam and HAZ. They also concluded that a decrease in either the conductivity of the electrolyte or polarizability of the steel will make the current distribution over the individual heterogeneous regions of the weldment more nonuniform.

In summary, it is apparent that there is some controversy as to the mechanisms of the HAZ corrosion (12). HAZ corrosion has been attributed to active microstructural dissolution (1, 2, 3, 5) local compositional changes resulting in greater corrosion susceptibility of the HAZ (7) and to oxide film formation creating the proper electrochemical conditions for HAZ corrosion (4). Given the wide variety and the complexity of the steels used in many of these studies it is understandable that a single theory has not been proposed as to the cause of the HAZ corrosion.

3.0 Experimental Procedure

3.1 Materials Processing

The steel compositions studied in this program were selected by the sponsor committee and were based on a 2^3 factorial experiment design with two levels of carbon, manganese and niobium. The steels were vacuum cast by CANMET to control the impurity levels such as oxygen and nitrogen. Table 1 shows the composition of the steels. Steels 1a and 3a were steels cast before CANMET experienced technical difficulties with their furnace. These two steels were then corrosion tested to show the effects of minor changes in composition on corrosion.

All the steels were hot rolled to a thickness of 25 mm and a width of 150 mm. For each steel, two lengths of approximately 1 m were available. The base materials were fully characterized, these include:

1) Grain size measurement
2) Quantitative microstructural analysis
3) Room temperature tensile tests, and
4) Charpy tests at -10°, -50° and -80°C.

The base material characterization, showed that the laboratory steels were comparable to typical commercial grades (Appendix 1).

3.2 Welding of the Base Materials

Bead on plate welds, using the submerged arc welding process were made to prepare actual HAZ specimens for corrosion. The Oerlikon SD1-3Ni filler wire, in combination with Oerlikon OP121TT flux were used to ensure that the weld metal is more noble than the HAZ (13). The beads were laid along the centre-line of the plates, each typically 380 mm long. Two different heat inputs were used for each steel by changing the travel speed while keeping the current and voltage constant. The bead profiles obtained were similar. The welding parameters are listed in Table 2. A total of 20 welds were made. The minimum 1.2 kJ/mm heat input was dictated by the fact that higher welding speeds could not produce acceptable bead profiles. The 3 kJ/mm heat input represents the typical heat input used in North America for welding offshore materials. Corrosion specimens were cut from the weldments.

3.3 Gleeble Specimen Preparation

A partial CCT diagram was developed for Steel 3a to assist in the selection of Gleeble simulation parameters. Using this information, cooling times between 800°C and 500°C (t_{8-5}) of 5, 20 and 128 seconds were selected to produce martensitic, bainitic and ferritic microstructures respectively. It was found a typical Gleeble specimen size (10 x 10 x 800 mm), could not cool fast enough to achieve a 5 second span between 800°C and 500°C. The centre section was reduced to 5 mm diameter to achieve the 5 second cooling rate. Three Gleeble specimens were prepared at each cooling rate for each steel. These specimens were used in the constant potential dissolution test.

3.4 Microstructure Characterization

The continuous transformation phenomenon occurring during the cooling of the HAZ from 800°C to 500°C lead to a range of microstructures. These microstructures were very complex, and over the years, efforts to identify and characterize these microstructures have been made

by several workers. Dolby (14) emphasized simplicity and the use of the optical microscope. He proposed that the fundamental structures formed in a weldment (weld metal and HAZ) are: primary ferrite, acicular ferrite like, ferritic-carbidic aggregate and martensite. Kasugai and Inagakim (15) used both optical and electron microscopes and distinguished five types of ferrite (polyhedric, massive, sideplate, lath and acicular) and three types of bainite (one type of lower bainite and two types of upper bainite), among other structures.

From a theoretical point of view, except for martensite, the microstructure morphologies are the result of the diffusion process and kinetic factors, and the change from one microstructure morphology to another is not abrupt, but transitional. Based on a study of the literature (14-20) and the observations made in this project, the following terminology and classifications were used:

Grain Boundary Ferrite (GF) - ferrite that is associated with prior austenite grain boundaries (Figures 3 and 4).

Sideplate Ferrite (SF) - parallel ferrite laths nucleated at prior austenite boundaries and growing into the austenite grains. M.A. (martensitic and austenitic) phase and/or carbide phase may be observed between ferrite laths (Figures 3 and 4).

Acicular Ferrite like (AF) - ferrite like laths nucleated inside a prior austenite grain. Acicular ferrite like phase observed in the HAZ is generally much coarser than its counterpart in the weld metal (Figure 4). Occasional blocky intragranular ferrite grains are also included in this category (Figure 4).

Degenerated Pearlite (GP) - a pearlite phase observed inside prior austenite grains. The ferrite/carbide lamellae are irregular due to the fast cooling rates involved (Figures 3, 4 and 5).

Bainite (B) - comprises parallel ferrite laths with continuous or particular second phase (M-A, or carbide) in between. No attempt was made to distinguish between the upper and lower

bainite. However, most of the bainite observed resembles the classical description of upper bainite (Figures 6 and 7).

Martensite (M) - two types of martensite are identified; sheet martensite (SM) and tetragonal martensite (TM). The latter is the more common phase and is acicular in nature (Figures 6 and 7).

The term ferrite and carbide grains (F-C) is also used to describe the ferrite carbide phases observed in the fine grain zone of the HAZ or in the parent metal (Figure 8).

The samples used for metallographic analyses were etched with 2% nital. Quantitative microstructural analysis was performed using the point counting technique. At each region seven 9 x 9 grids, giving a total of 567 points, were counted. The magnification used varied from one region to another, depending on the requirements. Whenever possible, grain size measurement was performed and the method utilized was the linear technique. Again, the magnification used depended on the heat input and the regions studied. There are cases where reliable and accurate grain sizes cannot be estimated due to the complex microstructures present.

3.5 Corrosion Tests

In order to determine the more active portion, constant potential anodic dissolution experiments were utilized. In these experiments, the test pieces (actual welds) were first drilled and then a copper lead wire attached. The weldment was coated with paraffin wax so that only the top surface of the weldment was exposed to the electrolyte. All tests were performed in 0.5 moles/litre NaCl solution to approximate a sea water environment. This environment was chosen because it reduced the number of dissolved species interacting with the steel samples and it was also found by Itoh et al (4) to be more corrosive to steel.

3.5.1 The Constant Potential Anodic Dissolution Tests

In the constant potential anodic dissolution tests the weldment was held at a potential of -500mV versus saturated calomel electrode (vSCE) for four days using a Model 371 EGG Potentiostat. Four days were required to create sufficient damage for comparison between samples. An over-potential of -500 mV (vSCE) was chosen since this corresponds to the corrosion potential of steel in fast moving sea water (10 m/s) (3), environment of some importance in the application of the steels used in this study. The actual specimen size was 50 mm in length and 25 mm wide, symmetrical about the weld.

As mentioned earlier, the Gleeble specimens were 10 mm x 10 mm x 80 mm bars. The corrosion results were complicated by the geometry of the Gleeble specimens due to edge effects. Consequently, the Gleeble specimens having cooling times of 20 s and 128 s, were machined to cylinders of approximately 9 mm in diameter. Reproducible results were not obtained for the Gleeble specimens having cooling times of 5 s, probably due to the complicated geometry. Hence, detailed corrosion tests of these specimens were not pursued.

The test chamber consisted of two compartments, made from two concentric cylinders of plexiglass. The inner working electrode chamber was 115 mm in diameter, 155 mm high, and having a 3 mm thick wall. In order to provide an electrical bridge between the two chambers and to effect a good current path, 16 symmetrical holes, 6 mm in diameter were drilled into the cylinder at a height of 1088 mm from the bottom of the chamber. A micro-porous plastic sheet was then epoxied onto the inner surface of the cylinder to separate it from the counter-electrode chamber. This outer chamber was a plexi-glass cylinder with an inner diameter of 140 mm, and a height of 155 mm. A hole 10 mm in diameter drilled into this outer chamber 12 mm from the top acted as an overflow. Two litres of fresh electrolyte were fed into the working electrode chamber from a head tank to ensure there were no large changes in electrolyte composition. A pump circulated the electrolyte from a reservoir to the head tank. A stainless steel tube was used as a counter electrode. The cell design was similar to Figure 9. The outer chamber of the cell was cleaned once a day of accumulated corrosion product.

3.5.2. Microelectrode Tests

The aim of these tests was to determine the effect of over-potential and time, on the Position/Potential profiles. The same cell design was used as in the constant potential anodic dissolution studies, the exception being four pegs were used in the centre of the cell to house the sample. It was critical in these experiments that the sample surface be as flat as possible. In order to achieve this the specimen, with an attached lead wire, was first glued to a flat plexi-glass plate using rubber cement. The specimen was coated with Amercoat 90_R, which had some success preventing crevice corrosion in metallic glasses (21). A cylindrical piece of plastic 1.5mm in thickness, 75 mm in diameter was placed around the sample and the joint between the plastic and the plexi-glass sealed with paraffin wax, thus forming a mold into which Hysol $Epoxy_R$ could be poured. The ratio of resin to hardener used was 12 to 1. After 24 hours the hardened epoxy could be pried away from the plexiglass to expose an extremely flat mounted specimen. Four holes were drilled into the epoxy to house the pegs in the test cell. The bottom surface was sometimes ground in places to ensure a parallel sample.

The potential of the micro-electrode specimens was controlled by an EGG model 173 potentiostat. A modified Hokuto Denko HE 106 electrometer was used to measure the potential between the microelectrode and a SCE placed away from the sample surface. The voltmeter had an output impedance of 10^{14} ohms with an accuracy of 0.1 mV. In order to avoid line interference, isolation transformers were connected to both the electrometer and to the potentiostat.

Movement of the specimen with respect to both the calomel reference electrode and the microelectrode was performed manually. A microscope stage allowed controlled movements in the X-Y plane. The micro electrode was adjusted in the Z direction with an attached micrometer. A schematic diagram of the apparatus used is shown in Figure 9.

The microelectrodes were essentially of an Ag/AgCl type used in previous studies by Tsuru et al (22, 23). The procedure for their construction was as follows. Fine glass capillaries were made with tip diameters less than .15 mm. Two types of Ag/AgCl microelectrodes could then

be made from these glass capillaries. The first of these used a fine silver wire, less than 0.1 mm in diameter. These electrodes were made by soldering the silver wire to a copper lead wire. The junction between the two was coated with lacquer. A heated liquid solution of 0.2 - 0.3 moles $AgNO_3$, 2.93 moles KNO_3, 0.9 - 1.2g agar and 30 ml distilled water was allowed to infiltrate into the glass capillary to a height of approximately 5 mm above the fine portion of the capillary tube.

In order to increase the surface area of the silver, dendritic silver was grown in the microelectrode by cathodic reduction of silver nitrate. The electrode was finally chloridized by immersion into a solution of NaCl.

The second type of microelectrode was of the string variety. A segment of cotton string was wrapped around an Ag wire 2mm in diameter. The cotton was soaked in the aforementioned Agar solution. $AgNO_3$ was then cathodically reduced to Ag and the assembly was placed in a capillary tube and partly filled with the test solution. Both electrode types were allowed to stabilize for 24 hours in the test solution. Since the microelectrode experiments were very sensitive to prior surface treatment it was necessary to remove the deformed surface layer (formed due to polishing) on the steel surfaces electrolytically (24 hours at -500mV over potential (vSCE)) before microelectrode testing.

4.0 Results

4.1 Microstructural Characterization

Detailed quantitative microstructural analyses and grain size measurements were done on both the HAZ of the bead on plate welds and on the Gleeble specimens. The primary goal of this project was to correlate microstructure with corrosion behaviour. Three regions in each specimen were studied. They are the fusion line region (in the case of Gleeble samples, this is the constant temperature region), A_{c1} region (outer limit of the HAZ), and the mid point between the above two regions.

Tables 3a to 3c summarize the quantitative microstructural analysis data obtained at the fusion line, mid-point and the A_{c1} region of the HAZ at 1kJ/mm heat input. Similarly, Tables 4a to 4c show the data obtained for the 3kJ/mm heat input weld metals. The intergranular ferrite observed in the HAZ is mainly acicular ferrite like in nature. However, as one moves away from the fusion line, the aspect ratio of the ferrite decreases. At the A_{c1} region of the HAZ, a variety of microstructures were observed, including some partially transformed microstructures that led to difficulties during quantitative analysis.

A complex continuous transformation produced complex packets of microstructural features in the HAZ. This made grain size measurement extremely difficult, hence, not all grain size values could be measured. Table 5 summarized grain size numbers which were determined with a reasonable degree of confidence.

Tables 6 to 8 summarize the quantitative microstructures observed for the Gleeble simulated HAZ specimens with 800° - 500°C cooling time (t_{8-5}) of 5, 20 and 128 s. The microstructures observed were similar to those found in the HAZ of actual welds. A cooling time (t_{8-5}) of 20s in a Gleeble simulation was roughly equal to a heat input of 3 kJ/mm during welding.

Tables 9 and 10 present the grain size measurements made on Gleeble samples with the cooling times of 20s and 128s respectively. The 5s cooling time Gleeble samples contained primarily martensite, and accurate grain size measurement was not possible.

4.2 Corrosion Tests

4.2.1 Four Day Constant Potential Tests

4.2.1.a Results of Weldment

Examination of the anodic dissolution samples showed that the coarse grained region of the HAZ was generally more heavily corroded. In some steels, preferential corrosion extended beyond the coarse grained region of the HAZ. The maximum depth of the corroded region was measured by using a dial gauge on the focus rack of the stereo microscope at 50 X

magnification. The fusion boundary was taken as a zero reference to compare the relative depth of the corroded zone.

Figures 10 and 11 are corroded welds with the microstructures observed in the coarse grained regions of weldments 1-1 (i.e. steel 1 with 1 kJ/mm weld) and 1-3 (i.e. steel with 3 kJ/mm weld). These weldments were characterized by limited attack in the coarse grained region of the HAZ. The attack in this steel was even less at the higher heat input.

Figure 12 shows the corrosion profile of weldments 1a-1 and 1a-3. The attack on this steel was very similar to Steel 1, showing that a minor variation in composition has little effect on localized corrosion.

Weldments 3-1 and 3-3 (steels with high C, and high Mn) were characterized by heavy dissolution of the HAZ, which were not exclusively confined to the coarse grained region (see Figures 13 and 14). The corrosion attack was relatively unaffected with increase in heat input. Figure 15 shows the corrosion attack profiles for weldments 3a-1 and 3a-3. Although the profile was similar to Steel 3-1, an increase in the heat input reduced the damage as in Steel 1 weldments. Steel 3a has slightly higher Mn than Steel 3, but the silicon level was significantly 25% lower.

Steel 5 (low C, low Mn) weldments 5-1 and 5-3 were characterized by a smaller corrosion groove on the HAZ, and confined to the coarse grain region of the HAZ. With increasing heat input, the depth of attack in the HAZ diminished (Figures 16 and 17).

Steel 7 (low C, high Mn) weldments 7-1 and 7-3 had grooves which were not exclusively confined to the coarse grained region of the HAZ. The groove in each of these weldments was very similar in appearance to that of Steel 3 which had a similar Mn content. At higher heat inputs the groove became deeper with somewhat more dissolution at the CG HAZ (Figures 18 and 19).

When Nb was added to the low carbon steels, the dissolution of the HAZ became more severe in both the low Mn steel 6 (Weldments 6-1 and 6-3) and in the high Mn steel 8 (Weldments 8-1 and 8-3), when comparing to the corresponding Nb free steels 5 and 7 (Weldments 5-1, 5-3, 7-1 and 7-3). The higher Mn steel 8 (Steel 8) had the greater HAZ attack of the two. Increasing the heat input of these two steels increased the depth of the groove in Steel 8 (compare Figure 22 to Figure 23), but lessened it in Steel 6 (compare Figure 20 to Figure 21).

The presence of Nb in higher C steels (Steels 2 and 4) had little effect on the corrosion behaviour when compared to their respective Nb free steels (Steels 1 and 3). Again, the higher manganese steel (Steel 4) showed greater HAZ attack. Heat input increase had little effect on HAZ attack of Steel 2 (see Figures 24 and 25), but lessened the attack on Steel 4 (Figures 26 and 27).

Table 11 summarizes measurements on the depth of the corrosion grooves of each sample after the constant potential tests. These numbers are the average maximum depth based on measurement in two different cross-sections. The groove depth is an indicator of the severity of the corrosion attack.

4.2.1.b Results of Gleeble Samples

The presence of a noble weld metal zone in HAZ specimens may have enhanced the corrosion process. Thus, Gleeble simulated specimens were corrosion tested to eliminate the complications of variable composition and residual stress. The four day dissolution test data for the Gleeble specimens are summarized in Table 12. In general, uniform corrosion was observed in all the specimens. In all the Steels preferential attack in the thermal-cycled zone was evident.

The Gleeble specimen with a $t_{8/5}$ of 20s roughly corresponded to 3kJ/mm in 25mm thick plate. The constant temperature zone corresponded to the coarse grained zone of the HAZ. When the cooling time was increased to 128s, no sign of localized corrosion was observed in most of the

steels used. Figures 28, 29 and 30, respectively show the surface profiles of Steels 3, 4 and 8.

Comparing the D_m data for $t_{8/5}$ of 20s obtained from the Gleeble specimens (refer to Table 12) to that of the actual welds does seem to suggest that the weld metal zone has a definite effect on localized HAZ corrosion since the weld metal was made more noble by Ni addition and residual stresses were present.

4.3 Microelectrode Experiments

A graph of position versus potential ϕ for Steel 1a welded with a heat input of 1 kJ/mm is shown in Figure 31 for three different over potentials (vSCE) of the weldment in 0.5 N NaCl. With increasing over-potential (vSCE) of the weldment there is a corresponding increase in the potential ϕ of the microelectrode, corresponding to the increase in current leaving the specimen surface. It has to be emphasized here that the potential ϕ which the microelectrode measures was not an electrode potential but a potential difference which results from localized dissolution rates. A higher potential ϕ corresponded to a higher current. As shown in Figure 31 there was an increase in dissolution rate of the weld metal portion of the weldment with respect to the parent plate with increased over-potential. It should be noted that no cleaning or conditioning was done before taking any measurements. Little excess HAZ dissolution was observed in the profiles under these conditions. After four days at an over-potential of -500 mV (vSCE) specimen 1a showed little HAZ corrosion, Figure 12.

The Position/Potential ϕ profile for steel 3a (having a higher Mn content than Steel 1) is shown in Figure 32 as a function of weldment over potential (vSCE). It can be inferred from Figure 32 that there is an increase in weld metal dissolution with increased over-potential. Of importance is the increase in Potential ϕ in the vicinity of the HAZ indicative of a higher degree of dissolution than either the parent or weld material at all over-potentials tested. Severe corrosion of the HAZ after four days at an over-potential of -500 mV was observed in Figure 15.

The Position/Potential ϕ profile of Steel 1a welded with a heat input of 3 kJ/mm as a function of weldment potential (vSCE) in 0.5 N NaCl is shown in Figure 33. The characteristics of this profile are similar to those of specimen 1a - 1 kJ/mm (Figure 31). There is an overall increase in Potential ϕ of the microelectrode with over-potential, an increase in weld metal dissolution with over-potential and a little excess HAZ corrosion (Figure 12).

Figure 34 shows the Position/Potential ϕ profile of Steel 3a welded with a heat input of 3 kJ/mm. The main features of this profile are, increased weld metal dissolution with increased over-potential, and excessive HAZ dissolution at all over-potentials.

The Position/Potential ϕ profile of weldment 3-1 kJ/mm as a function of time (2-8 hours) at an over-potential of -500 mV (vSCE) is shown in Figure 35. At an over-potential of -500 mV (vSCE) there is an increase in the overall current leaving the specimen, until about six hours when a steady state is reached. The profiles after six hours begin to overlap, indicative of a steady state. The high dissolution rate of the weld material as well as the HAZ are suggested by the profiles in Figure 35. HAZ corrosion was observed in this specimen after four days at an over-potential of -500 mV (vSCE), Figure 13.

Similar behaviour was observed in the Position/Potential profile of weldment 4 - 1kJ/mm as seen in Figure 36. Peaks were detected in the region of the HAZ. The curve obtained after 24 hours shows an overall reduction in Potential ϕ compared to the curves obtained between four to twelve hours.

Figure 37 shows a graph of total current versus time for weldment 2 - 1 kJ/mm. It can be seen from this Figure that it took approximately twelve hours for the current to reach a plateau of about 6 mA. These results are supported by the Position/Potential ϕ profile for this material, shown in Figure 38a. There is an overall increase in ϕ with time up to twelve hours at which point the profiles begin to overlap. Little enhanced HAZ dissolution is noted. Figure 38b shows these profiles after long term exposure. All these curves are within 1 mV of one another, indicative of the small change in current of the plateau region.

A graph of time versus current is shown in Figure 39 for sample 7-3 kJ/mm held at an over-potential of -600 mV (vSCE). After about twelve hours there is a decrease in the rate of change of current with time. Figure 40a shows a Position/Potential ϕ for this weldment. There is an upward shift of the profiles which corresponded to the increase in current with time up to twelve hours. Figure 40 b shows an expanded scale Position/Potential ϕ profile of weldment 7-3 kJ/mm for longer holding times. The less than 1 mV difference between the curves is suggestive of the small change after long holding times. Notable peaks in the profiles are observed in the HAZ region.

A schematic diagram of the surface colouration after 8 hours and 48 hours in 0.5 N NaCl is shown in Figure 41. After 8 hours there was an incomplete oxide covering on the weldment. After 48 hours there was a complete oxide coating. The inner portion of the HAZ had a bright orange-red colour, the rest of the weldment had a black-orange colour.

A graph of current versus time for weldment 5-1 kJ/mm is shown in Figure 42. The corresponding Position/Potential ϕ profiles for this material are shown in Figure 43a. This specimen took about 24 hours to reach a relatively stable value. A small peak in the HAZ is noted in Figure 43b.

The Position/Potential ϕ profiles of weldment 4-1 kJ/mm as a function of time are shown in Figure 44. The peaks in the HAZ region become more distinct with the passage of time. There is an overall increase in Potential ϕ with time, corresponding to the increase in current with time up to twelve hours where there is a decrease in the rate of change.

Figure 45 shows the Position/Potential ϕ profiles of weldment 6-1 kJ/mm as a function of time at an over-potential of -600 mV (vSCE). This Figure shows the same general trends as did weldment 4-1 of Figure 44. These trends are an overall increase in Potential o with time, and an emergence of prominent peaks in the HAZ. The position of these peaks is also of some importance; they are indicative of the fact that the HAZ corrosion in this weldment was narrowly confined to the most highly reheated region of the HAZ, as shown in Figure 22, after four days exposure at an over-potential of -500 mV (vSCE).

The Position/Potential ϕ profiles of Steel 7 welded with a heat input of 1 kJ/mm are shown in Figure 46 as a function of holding time at an over-potential of -600 mV (vSCE). Well pronounced peaks in the HAZ are observed in these profiles. The wide appearance of the peaks in the HAZ are indicative of the relatively uniform corrosion which occurred in this material, see for example Figure 18.

The Position/Potential ϕ profiles of Steel 8, welded with a heat input of 3 kJ/mm is shown as a function of time in Figure 47. It has the same characteristics as the other profiles discussed to this point. There is an increase in the overall Position/Potential ϕ profiles with time up to twelve hours where there is a decrease in the rate of change. The Potential peaks in the HAZ also appear to become more enhanced with time. The position of the peak Potentials near the fusion line in this material are indicative of the severe corrosion in the overheated region as seen in Figure 21.

4.3.1 Summary of Microelectrode Experimental Results

There was a qualitative agreement between the microelectrode experiments and the longer term tests performed at an over-potential of -500 mV. Tests performed as a function of over-potential showed that in the case where there was active dissolution of the HAZ, the HAZ corroded at all the overpotentials used. It was observed that the weld material became more active with increasing over-potential. Tests as a function of time showed that it generally took about twelve hours for the current and hence the Position/Potential ϕ profiles to stabilize and this generally corresponded to a complete oxide covering situation. It was also observed that the oxide had a different colour above the HAZ. Lastly, the shape of the profiles obtained with the micro-electrodes corresponded very closely to the morphology of the attack obtained from four day constant potential dissolution test.

5.0 Discussion

5.1 Metallography and Effects of Microstructure

The microstructures observed in the HAZ are varied and complex. Careful study and comparison of the different cooling rates and compositions revealed the transformation sequence. In the past, the side-plate ferrite and acicular ferrite like phases were often mistaken as a bainitic phase. However, these phases were usually associated with grain boundary ferrite, indicating that they are higher temperature transformation phases. With moderate increases in cooling rate, the side-plate and acicular ferrite like phase contents increase at the expense of the grain boundary ferrite phase (compare Table 6a with Table 4a, Steel 1). At higher cooling rates, these phases will be replaced by bainite or martensite (compare Table 6a with Table 7a, Steel 1).

The degenerated pearlite phase is not commonly observed in commercial steels. The amount of this phase decreases with higher hardenabilities and faster cooling rates, suggesting that this was a high temperature transformation product. At lower cooling rates and in the presence of a large amounts of grain boundary ferrite, this phase was located within the prior austenite grains. At higher cooling rates, and when bainitic phases were present, this phase is associated with prior austenite grain boundaries. This observation suggests that this phase forms in the temperature range between grain boundary ferrite phase and the bainite phase formation. The morphology also fits the description of the pearlite phase.

Due to the complexity of the microstructure, it was not possible to obtain reliable grain size in the HAZ. The anodic dissolution results showed that the coarse grained region was preferentially etched in most of the steels studied. This suggested that grain boundary effects and subsequently the grain size was not an important factor.

Table 11 summarized the microstructures observed in the coarse grained HAZ and the corrosion depth observed. There was no clear correlation between microstructures in the HAZ and the degree of corrosion suffered by the region. For example, when Steels 1 and 2 were welded using a heat input of 3 kJ/mm, the resulting microstructures were quite different. Weldment

1-3 had ferrite/pearlite as the major structure in the coarse grained region and Weldment 2-3 had acicular ferrite like as the main component. However, both weldments had similar corrosion groove.

On the other hand, Weldments 7-1 and 8-1 had very similar microstructural components in the coarse-grained region (acicular ferrite like being the major component), but the degree of corrosion as measured by the groove depths, was very different. Weldment 8-1 had the greater depth. Similarly, Weldments 4-3 and 8-3 had similar microstructures but different degree of corrosion attack.

In this study there is some clear trend on the effects of heat input. When the heat input was increased from 1 kJ/mm to 3 kJ/mm weldments 1 to 6 showed less corrosion attack, weldment 7 and 8 showed increased attack. However, the Gleeble specimens showed generally an increase in localized corrosion (D_m) when the cooling time t_{8-5} was increased.

5.2 Chemistry Effect

The composition of the parent plate significantly influenced the corrosion behaviour of the HAZ. For example it was observed that addition of Nb to low carbon steels, the dissolution of the HAZ became more severe in both the low Mn Steel (Steel 6) and in the high Mn Steel (Steel 8). The addition of Nb to the higher C steels (steels 2 and 4) had little effect on the corrosion behaviour. Clearly then, the composition within the microstructure as opposed to the physical characteristics was the important parameter. The effect of C was such that, as the C level decreased the localized HAZ corrosion increased in corresponding steel compositions (refer to Table 11). Thus, it seems possible that C is playing a role in tying up portions of HAZ Mn or/and Nb and allowing the excess of the latter elements to be dissolved in ferrite phase. These excess concentrations of Mn or/and Nb dissolved in the ferrite phase may be responsible for the HAZ corrosion through increased hardenability.

It has been suggested (7) that the HAZ corrosion was the result of quenched-in carbon in the ferrite lattice; the effect of Mn was therefore indirect since it increased the amount of quenched-

It has been suggested (7) that the HAZ corrosion was the result of quenched-in carbon in the ferrite lattice; the effect of Mn was therefore indirect since it increased the amount of quenched-in carbon(7). In order to test this hypothesis, Steel 8 welded with a heat input of 1 kJ/mm was subsequently annealed for 2 hours at a temperature of 200°C (473°K). This treatment was designed to precipitate most of the carbon in the form of Fe-carbides (21) but keep the Nb carbides stable (22). Figure 48 shows the corroded specimen of 8-1 a. Examination of the corrosion groove for the unannealed Steel 8 and the annealed Steel 8 (8-1, and 8-1a respectively of Table 11), both welded with a heat input of 1 kJ/mm showed no differences between the unannealed and annealed specimens. This seems to suggest that the rate of dissolution of the HAZ was not the result of "quenched-in" carbon in the present study. However, the possibility of stronger effects of Nb masking the effect of C on corrosion should not be ruled out.

Mn may have a direct chemical effect on the corrosion behaviour. There is strong evidence to suggest that during the transformation from austenite to ferrite Mn will segregate to the austenite phase (23-25) even for annealing times as short as 100 seconds in the intercritical temperature range (25). During the transformation from austenite to pearlite the Mn will tend to associate itself with the cementite phase and avoid the ferrite. This has been thermodynamically predicted (26) and has been experimentally verified in a number of studies (27, 28, 29), even for short annealing times of 5 seconds below the so-called no-partition temperature (29). It is therefore expected that in a ferrite/pearlite matrix steel that there would be a higher Mn content in and around the cementite. When a steel is welded it will take approximately 30 seconds for it to cool from 1000°C (1273°K) to 500°C (773°K) with a heat input of 3 kJ/mm, and less than 5 seconds with a heat input of 1 kJ/mm (50). These rapid cooling rates and high temperatures (especially in the coarse grain region) will cause the pearlite phase to dissolve, disassociating the cementite and Mn, thus effectively increasing the Mn concentration in the ferrite phase in the HAZ.

Mn is known to increase the thermodynamic activity of Fe (31). It is also approximately 800 mV lower on the Pourbaix diagram than is Fe (32), and has been observed to preferentially segregate and oxidize at grain boundaries in Fe (33). This information suggests that an increase in the effective Mn concentration would increase the dissolution of the HAZ.

Mn also has another detrimental effect on HAZ corrosion, by increasing the solubility of Nb(CN) in Fe (34, 35, 36). In the present study Nb additions were noted to cause increased corrosion in the lower carbon steels (Steels 6 and 8). Nb is added to HSLA steels in order to control the grain size (through Zener pinning of grain boundaries by Nb(CN)) and for precipitation hardening. The equilibrium dissolution temperature of Nb(CN) is approximately 1100°C (1373°K) for typical Nb and C levels in HSLA steels, (a temperature which is easily exceeded during the weld thermal cycle), but during the rapid thermal cycle some superheating is required (30). The tendency of the precipitates to dissolve depends not only on the composition of the base metal, but also on the particle size.

The work of Suzuki et al (37) has demonstrated that as the particle size increased so did the dissolution time; there was little effect of Nb addition on the dissolution kinetics, but increasing the C content significantly increased the dissolution time. Both solubility product calculations (35) and kinetic factors show that as the C content is increased, less Nb can go into solution. Hence the lower carbon steels were greatly affected by Nb because of faster dissolution of Nb (C,N) resulting in more soluble Nb in the matrix. On the other hand, the Nb (C,N) dissolution rate in a high C steel is lower, resulting in less free Nb in the matrix. As one example, large changes were observed between the lower carbon steels, (Steel 7) which only had 0.002 wt% Nb and Steel 8 which contained .04 wt% Nb, while little change was observed in the higher C steels, (Steel 1 which contained no Nb and Steel 3 which contained 0.04 wt% Nb (Table 11). Other examples may also be noted in Table 11. Nb occupies a similar position on the Pourbaix diagram to Mn, 700 mV lower than Fe (32), and is also noted for raising the activity of Fe (38).

Figure 49 shows an empirical fit of the corrosion groove depth for the steels welded with a heat input of 1 kJ/mm against an enrichment factor. Mn enrichment is defined as the difference between the soluble Mn in the HAZ and the expected soluble Mn content of the ferrite in the base material assuming that there was 4 times the Mn content in the cementite as there was in the ferrite (28, 29). The Nb enrichment is the difference between the soluble Nb content in the HAZ and that in the base metal. It is assumed that in the base metal, due to precipitation of Nb (C, N), the soluble Nb level is negligible. In the coarse grained region of the HAZ it is

Nb (C, N), the soluble Nb level is negligible. In the coarse grained region of the HAZ it is assumed that total dissolution occurred in the lower carbon steels while no dissolution of Nb occurs in the higher carbon steels. Total dissolution of Mn in all the steels was assumed. These assumptions are supported by the literature. The factor of four is empirically added to account for the much stronger apparent effect of Nb on corrosion as compared to Mn and to fit the data more closely to that of the Mn data. Appendix 2 outlines the calculation of Mn enrichment. In Figure 49 the corrosion depths for the steels welded with a heat input of 3 kJ/mm are also plotted against the enrichment factors.

5.3 The Gleeble Specimens

In an actual weldment, the presence of a weld metal zone and the possibility of the existence of residual stress may complicate the localized corrosion behaviour of the weldment. In this program, filler material with Ni was used to ensure that the weld metal was more noble. This Galvanic factor alone may cause HAZ corrosion. Residual stress, due to the rapid thermal cycle endured in welding, is unavoidable. Residual stress will make the weldment more active and thus more susceptible to localized corrosion. To complement the data obtained in actual weldments Gleeble specimens eliminated the complication of the weld metal chemistry and the residual stress.

All the Gleeble specimens showed signs of a preferential localized corrosion. At the longer cooling time (128 s) there was increased attack in most of the steels (refer to Table 12). As a consequence of the longer cooling time, more time for diffusion was available for Mn distribution in the HAZ. Hence, one would expect a lower localized corrosion of the HAZ. But, on the contrary, this was not the case in the present study. Low C low Mn Steel 5 and Nb containing low Mn steels 2 and 6 showed a predominant increase in the localized corrosion of the HAZ when the cooling time $t_{8/5}$ was increased from 20s to 128s. This behaviour cannot be explained using the aforesaid discussions of section 5.2.

Even though the effect of Mn and C on the HAZ localized corrosion cannot be readily explained from the results of Gleeble specimens, the effect of Nb is quite evident. Steels 2 and

4 containing Nb showed higher localized corrosion in Gleeble specimens with t_{8-5} of 128s. Steels 4 and 8 containing Nb showed higher localized corrosion in Gleeble specimens with t_{8-5} of 20s. Unlike weldment corrosion, Nb had the effect on both high and low C as well as Mn steels in significantly increasing the localized corrosion. The extent of corrosion depended on the t_{8-5} cooling time.

Some of the discrepancies observed, in the localized corrosion, between the weldment and Gleeble HAZs can be explained by the method of corrosion depth measurements. In the case of weldments the corrosion depth was measured from the fusion boundary as a reference. This method may have an effect on the depth measurement since the weld metal also corroded. In Gleeble specimens, the entire surface of the rod specimen was corroded: in some areas more than others (refer to the figure in Table 12). The maximum depth ($D_m/2$) was determined by measuring the minimum diameter in the Gleeble treated band and the average maximum diameter on either end of the band (as reference). Again, this shows that there may be an effect of choosing a reference point, in representing the magnitude of the localized corrosion.

Comparing the weldment specimens and the Gleeble samples, the latter generally showed less corrosion attack (for Gleeble specimens depth = $D_m/2$), and were on the contrary to the findings of the former. This suggested that the presence of the weld metal zone and the residual stress have a definite influence on localized corrosion. Thus to prevent localized HAZ corrosion, efforts must be made to make the weld metal composition compatible with the HAZ and the parent plate. Welding procedure to minimize residual stress and "quench in" elements such as Mn and Nb should be followed.

5.4 Analysis of Factorial Experiments

The analysis of the factorial experiments performed for the weldments in Appendix 3 showed that the main effects of C, Mn, Nb and the interaction of C combined with Nb were significant in the anodic dissolution of HAZ. However, such an analysis performed for the Gleeble specimens did not show significance of any elements on the anodic dissolution characteristics of the HAZ.

5.5 Micro-Electrode Experiments

The micro-electrode technique is a short time test. There is the possibility of quantitatively predicting the localized corrosion susceptibility of a weldment in a short time (a few minutes) using this technique. One of the original aims of the micro-electrode experiments was to look into this possibility. It was observed that immersion time had significant effect on the position/potential curve, and on average, twelve hours were required for stabilization. Even at this stage current fluctuations occurred. The overpotentials used also varied the position/potential curve. At more negative potential, the maximums observed at HAZ were more pronounced. To quantify the technique, the potential ϕ must be related to corrosion rate. Since ϕ is effected by factors mentioned above, plus the effects of the electrode type, diameter and the distance between the work pieces and the micro-electrode. The latter is of particular importance since it can produce very large ϕ variation. To accommodate the effect of distance between the electrode and the workpiece, very sensitive distance measurement facility and the relationship between ϕ and distance are required. This accuracy was beyond the scope of the project and therefore not pursued. As mentioned, a more negative potential gave a sharper peak over the HAZ. This was the reason why a great number of the tests were performed at -600 mv overpotential.

The composition of the oxide layer formed on the microelectrode will provide valuable clues to the exact corrosion mechanisms. For example, if the oxide layers at the HAZ contained higher Mn and Nb than oxides in other regions. This can be used as direct proof that active dissolution of the above two elements is an important mechanism.

It was observed in these experiments that there was an increase in potential of the micro-electrode with time corresponding to an increased amount of current leaving the sample surface, see for example Figures 38 and 40. The stabilization in the current was probably due to the formation of an oxide completely covering the surface. With subsequent time there was little change in the current response. Although the presence of the oxide may accentuate any HAZ corrosion, the main mechanism of HAZ corrosion is the active dissolution of the HAZ due to

increased soluble Nb and Mn. The experiments performed as a function of overpotential showed that the HAZ would corrode at all overpotentials used in this study, while the response of the weld material depended on the overpotential. The oxide over the HAZ had a different colour after prolonged exposure indicating that it was different over the HAZ than over any other part of the weldment. The nature of an oxide film will depend on the microstructure of the substrate as well as on the chemical composition of the substrate (39, 40). Even with the presence of a thick oxide, active HAZ dissolution was detected. A qualitative correlation between the long term tests and the micro-electrode experiments was shown. Lack of experimental control was the reason why a quantitative correlation could not be made at this time.

6.0 Summary and Conclusions

The following conclusions can be drawn from this study:

1. An examination of the microstructures of the coarse grain region of the HAZ has shown no direct relationship between HAZ optical microstructure and HAZ corrosion.

2. Increasing the Mn content increased the depth of the corrosion groove in the HAZ.

3. Decrease in C content increased the depth of corrosion groove in the HAZ.

4. A comparison of Gleeble simulated specimens with the actual weld specimen results showed that the weld metal zone and residual stress also contributed to HAZ corrosion i.e. the Gleeble specimen showed generally less corrosion attack than that of the actual weldment samples.

5. Nb additions to low carbon steels were detrimental to the localized corrosion behaviour of the weldment HAZ. However Nb additions to high carbon steels had little effect.

6. The effect of increased heat input was to generally decrease the HAZ corrosion in the weldments. An increase in heat input generally yielded a softer HAZ. However, the increase in cooling time in Gleeble specimens increased the HAZ corrosion.

7. Micro-electrode experiments in this system have shown a qualitative agreement for the 4 day dissolution tests. Although chemical differences between the weld metal and parent plate are a prerequisite for HAZ corrosion, the oxide formation may accentuate this attack in these steels.

7.0 Recommendations

1. To study hardenability and specifically the effects of C, Si and Mn on the HAZ corrosion of steel weldments in salt water. This would require constant microstructures and variable alloying.

2. The Gleeble specimens should be prepared for the steel compositions used in (1) using more realistic t_{8-5} cooling times (corresponding to the heat inputs used in (1)). The corrosion tests need to be carried out in a way comparable to the tests in (1). Also, excessive corrosion of the non-heat treated regions of the specimens should be prevented.

3. Microhardness measurements of the various regions in the HAZ and their correlations with the HAZ corrosion are required.

8.0 References

1. E. Rasanen and K. Relander, Scandinavian Journal of Metallurgy, 7 (1978), 11-17.

2. A.V.A. Saarinen, Proceedings ICSTIS, Suppl. ISIJ, Vol. 11, 1971 1101-1106.

3. A. Saarinen and K. Onnela, Corrosion Science, 10 (1970), 809-815.

4. K. Itoh, H. Mimura, T. Inoue, R. Todoroki, Y. Horii, and H. Kihira, Symposium on Corrosion and Applied Electrochemistry, Oct. 10, 1085, 1-40.

5. H. Adrian, P. Drodten, H.J. Engell, D. Grimme, G. Herbsled, D. Horstmann, S. Mennenoh and W. Schwenk, Corrosion Science, 17 (1977), 143-153.

6. S. Lundin and B. Utterberg, 5th Scandinavian Corrosion Congress (1968), 33-1 yo 33-20.

7. R. Raty, J. Hakala and H. M. Miekk-oja, Jernkont. Ann. 154 (1970), 398-411.

8. G. Blackmann, A. Leimalm and S. Lundin, Welding Research Abroad, Oct. 1972, 22-31.

9. Ing and H. D. Steffens, IIW (1975) Subdivision No. 2, 2-28 to 2-48.

10. R. Strommen, IIW (1975) Subdivision No. 2, 2-01 to 2-26.

11. B.B. Chernov and R.V. Chichkin, Protection of Metals, May 1984, 644-647.

12. P. Droten, O. Steensland, S.Mennenoh and U.Tenhaven, A Baumel, Arch. Eisenhuttenwes 44 (1973), #12, 953-957.

13. Private Conversation with R.Brigham, CANMET, 1985.

14. Abson, D. J. Dolby, R.E., Doc. IIW-IXJ - 29-80, 1980.

15. Kasugai, T., Inagaki, M., "Microstructures and Their Morphologies in Weld Zone", 4th Symposium of JES, Osaka, 1982.

16. Kikuta, J. et al,Doc. IIW-IX-1982-83, 1983.

17. Watson, R.A. et al, Weld Metal Fabrication, No. 3, 1981.

18. Farrar, R. A. et al, Weld Metal Fabrication, No. 5, 1981, p 223.

19. Levine, E., Hill, D. C., "Structure and Properties of HSLA Weld Metal Containing Nb or V", Proceedings "Welding of HSLA Steels", 1979, Rome.

20. Jan, B. and Lubos, P., IIW Doc. IX-B-112-85.

21. Hanawa, K. and T. Mimura, Met. Trans., Vol 15A, p 1147, 1984.

22. Hansen, S.S., Vander Sande, J. B. and Cohen, M., Met. Trans., Vol. 11A, p 387, (1980).

23. Gilmour, J.B., Purdy, G. R. and Kirkaldy, J.S., Met. Trans., Vol 3, P 1455, (1972).

24. Bangaru, N.R.V. and Sachdev, A.K., Met. Trans., Vol. 13A, p 1899, (1982).

25. Wycliffe, P., Scripta Metallurgica, Vol. 18, p 327, (1984).

26. Cahn, J.W. and Hagel, W.C., Decomposition of Austenite by Diffusional Processes, John Wiley, p. 131, (1962).

27. Razik, N.A., Lorimer, G.W. and Ridley, N., Acta Metallurgica, Vol. 22, p. 1249, (1974).

28. Miller, M. K. and Smith, G.D.W., Metal Science, July p 249, 1977.

29. Williams, P.R., Miller, M.K., Beaven, P. A. and Smith, G.D.W., Phase Transformations, Vol 2. Inst. of Metallurgists, p. 98, 1979.

30. Easterling, K., Introduction to the Physical Metallurgy of Welding, London, Butterworths & Co. Ltd. (1983).

31. Hultgren, R., Desai, P., Hawkins, D. T., Gleiswer, M. and Kelly, K.K., Selected Values of Thermodynamic Properties of Binary Alloys, ASM (1973).

32. Pourbaix, M., Atlas of Electrochemical Equilibria in Aqueous Solutions, NAC (1974).

33. Wei, W. and Graebke, H.J., Corrosion Science, Vol. 26, p. 223, (1986).

34. Sharma, R.C., Lakshmanan, V.K. and Kirkaldy, J.S., Met. Trans. Vol. 15A, p. 545, (1984).

35. Koyama, S., Ishii, T. and Narita, K., Japan Inst. of Metal J., Vol 35, P 698, (1971).

36. Koyama, S., Ishii, T. and Narita, K., Japan Inst. of Metal J., Vol. 35, P. 1089, (1971).

37. Suzuki, S., Weatherly, G.C., Houghton, D.C., Acta Metall., Vol 35, p 341, (1987)

38. Paul, E. and Swartzendruber,, L.J., Bulletin of Alloy Phase Diagrams, Vol 7, p. 248 (1986).

39. Townsend, H.E., Cleary, H.J. and Allegra, L., Corrosion 37 #7 (1981), 384-391.

40. Blekkenhorst, F., Ferrari, G.M., Van Der Wekken, C.J. and Ijsseling, F.P., Br. Corros, J. 21 #3 (1986), 163-176.

Table 1

Table of Steel Compositions

Steel	C	Mn	Si	Nb	S	Al	O	N	Cu	Ni	Cr	Mo	V
							ppm	ppm					
1	0.12	0.78	0.28	0.002	0.009	0.025	54	57	0.012	0.007	0.019	0.002	0.002
1a	0.14	0.70	0.25	-	0.005	0.030	-	-	-	-	-	-	-
2	0.12	0.80	0.29	0.038	0.009	0.025	48	59	0.012	0.007	0.019	0.002	0.003
3	0.13	1.39	0.35	0.002	0.009	0.032	70	64	0.012	0.007	0.019	0.002	0.003
3a	0.14	1.50	0.25	-	0.005	0.030	-	-	-	-	-	-	-
4	0.13	1.44	0.38	0.040	0.009	0.025	60	60	0.012	0.007	0.019	0.002	0.003
5	0.055	0.78	0.31	0.002	0.009	0.015	50	52	NA	NA	NA	NA	NA
6	0.052	0.77	0.31	0.035	0.009	0.015	55	50	NA	NA	NA	NA	NA
7	0.057	1.54	0.31	0.002	0.009	0.015	75	55	0.012	0.007	0.019	0.002	0.004
8	0.056	1.53	0.32	0.039	0.009	0.015	65	49	0.012	0.007	0.019	0.002	0.004

NA = not analyzed

Table 2

Table of Welding Parameters

Welding Parameters
Filler Wire = SD1-3Ni
Flux = OP121TT

Weld	Current (A)	Voltage (V)	Speed (cm/min)	Nominal Heat Input kJ/mm
A	500	28	70	1.2
B	500	28	27.5	3.05

Table 3a

Quantitative Microstructural Analysis at the Fusion Line

H.I. = 1 kJ/mm

Steel	GF%	AF%	SF%	GP%	TM%	SM%
1	15	47	20	18	-	-
2	12	66	16	6	-	-
3	5	-	13	-	53	29
4	4	-	28	-	52	16
5	51	33	16	-	-	-
6	48	39	12	-	-	-
7	20	68	12	-	-	-
8	22	61	17	-	-	-

Table 3b

Quantitative Microstructural Analysis at the Mid-Point of HAZ

H.I. = 1.0 kJ/mm

Weld made from Steel	GF%	AF%	SF%	GP%	TM%	SM%	Distance from Center Line
1	29	35	11	25	-	-	0.4
2	13	64	16	7	-	-	0.5
3	7	-	14	-	58	21	0.6
4	4	36	22	-	26	12	0.6
5	62	26	12	-	-	-	0.6
6	59	38	3	-	-	-	0.5
7	22	69	9	-	-	-	0.7
8	27	62	11	-	-	-	0.7

Table 3c

Quantitative Microstructural Analysis at the A_{c1} region of HAZ

H.I. = 1.0 kJ/mm

Steel	GF%	AF%	SF%	GP%	Ferrite%	Carbide%
1	61	18	9	12	-	-
2	-	-	-	3	83	14
3	74	-	15	11	-	-
4	-	-	-	-	-	-
5	-	-	-	-	-	-
6	-	-	-	-	95	5
7	83	13	4	-	-	-
8	-	-	-	-	-	-

Table 4a

Quantitative Microstructural Analysis at the Fusion Line

H.I. = 3.0 kJ/mm

Steel	GF%	AF%	SF%	GP%
1	47	29	21	3
2	19	69	12	-
3	14	69	15	2
4	16	54	30	-
5	78	16	6	-
6	45	32	23	-
7	53	42	5	-
8	35	53	12	-

Table 4b

Summary of Quantitative Microstructural Analysis at the Mid HAZ

H.I. = 3.0 kJ/mm

Steel	GF%	AF%	ST%	DP%	Distance from Center Line (mm)
1	44	37	11	8	1.1
2	34	55	11	-	1.0
3	12	70	14	5	1.1
4	17	55	28	-	0.6
5	90	6	4	-	1.1
6	82	12	6	-	0.8
7	70	24	6	-	1.0
8	72	26	2	-	0.8

Table 4c

Summary of Quantitative Microstructural Analysis

at the A_{c1} Region of HAZ H.I. = 3.0 kJ/mm

Steel	Ferrite	Carbide	Distance from Center Line
1	90	10	2.2
2	88	12	2.1
3	91	9	2.5
4	-	-	-
5	94	6	2.2
6	96	4	1.7
7	96	4	2.0
8	97	3	1.7

Table 5

Summary of Available Grain Size Numbers at the Fusion Line of the HAZ (grains/mm^3)

Steel	Heat Input 1 kJ/mm	Heat Input 3 kJ/mm
1	NA	1.0×10^2
2	8.0×10^2	1.3×10^2
3	2.5×10^2	12
4	NA	3.2×10^2
5	NA	NA
6	NA	NA
7	NA	NA
8	NA	NA

Table 6a

Quantitative Microstructural Analysis of

Central Region of Gleeble Samples

Steel	GF %	SM %	TM %	B%	AF %	SF %	DP %
1	1	11	73	7	–	–	8
2	1	12	67	19	–	–	2
3	1	9	90	1	–	–	–
4	–	17	83	–	–	–	–
5	34	–	–	–	47	19	–
6	8	–	–	–	61	31	–
7	1	11	83	5	–	–	–
8	1	10	83	7	–	–	–

Table 6b

Quantitative Microstructural Analysis of Gleeble Samples:

Mid-point region of transformed zone

($t_{8\text{-}5}$ = 5 s)

Steel	GF%	SM%	TM%	B%	GP%	AF%	SF%	Distance from Center Line (mm)
1	2	20	64	7	7	–	–	3.0
2	1	23	61	13	3	–	–	2.2
3	–	15	84	1	–	–	–	3.0
4	–	25	75	1	–	–	–	3.1
5	48	–	–	–	–	33	19	2.8
6	17	–	–	–	–	54	29	3.2
7	1	18	74	7	–	–	–	2.2
8	1	16	78	6	–	–	–	2.6

Table 6c

Quantitative Microstructural Analysis: Gleeble, Edge of

Transformed Zone

($t_{8\text{-}5}$ = 5 s)

Steel	PEF	Bainite	GP	SM	TM	AF	SF	Distance from Center Line
1	72	15	13	–	–	–	–	6.1
2	40	43	17	–	–	–	–	4.5
3	NA	NA	NA	–	–	–	–	6.0
4	–	7	–	41	52	–	–	6.2
5	–	–	–	–	–	93	7	5.7
6	–	–	–	–	–	87	13	6.5
7	1	15	–	13	71	–	–	4.5
8	12	19	–	18	51	–	–	5.2

Table 7a

Quantitative Microstructural Analysis

of Gleeble Samples Central Region

(t_{8-5} = 20 s)

Steel	GF%	SF%	AF%	B%	GP%
1	9	20	36	-	35
2	1	36	59	-	3
3	1	25	9	65	<1
4	-	24	4	72	-
5	38	11	51	-	-
6	5	28	67	-	-
7	2	15	83	-	-
8	2	29	69	-	-

Table 7b

Quantitative Microstructural Analysis

of Gleeble Samples: Mid point region

(t_{8-5} = 20 s)

Steel	GF%	SF%	AF%	DP%	B%	Distance from Centre Line(mm)
1	9	21	43	28	-	3.7
2	1	41	49	9	-	2.6
3	<1	20	5	1	74	2.6
4	-	24	4	-	72	2.2
5	62	5	33	-	-	2.7
6	<1	15	85	-	-	4.1
7	<1	12	87	-	-	3.7
8	3	24	73	-	-	3.2

Table 7c

Quantitative Microstructural Analysis

of Gleeble Samples: Edge of Transformed Zone

(t_{8-5} = 20 s)

Steel	GF%	SF%	GP%	AF%	B%	Ferrite%	Carbide	Distance from Centre Line(mm)
1	74	15	11	-	-	-	-	7.4
2	66	26	8	-	-	-	-	5.2
3	2	28	2	9	59	-	-	5.2
4	-	39	-	11	50	-	-	4.5
5	-	-	-	-	-	97	3	-
6	-	-	-	-	-	95	5	-
7	86	11	3	-	-	-	-	-
8	2	24	1	73	-	-	-	-

Table 8a

Quantitative Microstructural Analysis

(Centre of Gleeble: $t_{8/5}$ = 128s)

Steel	GF %	SF %	AF %
S1	20	14	66
S2	13	16	71
S3	7	15	77
S4	3	19	78
S5	55	3	42
S6	34	10	56
S7	37	14	49
S8	6	42	52

Table 8b

Quantitative Microstructural Analysis

Gleeble Sample: Mid Point

($t_{8/5}$ = 128 s)

Steel	GF%	SF%	AF%	GP%	Distance from Centre Line (mm)
1	31	15	54	-	5
2	14	23	63	-	6.9
3	11	23	66	<1%	6.9
4	2	32	66	-	6.3
5	77	-	23	-	4.8
6	29	27	44	-	4.4
7	28	25	47	-	5.1
8	8	51	41	-	4.2

Table 8c

Quantitative Microstructural Analysis

Edge of Gleeble ($t_{8/5}$ = 128 s)

Steel	Ferrite	Carbide	Distance from Centre Line (mm)
1	92	8	10
2	88	12	13.8
3	87	13	13.8
4	88	12	12.7
5	94	6	9.6
6	95	5	8.8
7	95	5	10.2
8	95	5	8.4

Table 9

Summary of Grain Size Measurements

(Gleeble, $t_{8/5}$ = 20s)

	Volumetric Grain Size (g/mm^3)		
Designation	Centre	Middle	Edge
1	19	59	2.6×10^5
2	78	1.4×10^3	3.2×10^5
3	9.8×10^2	1.1×10^3	1.9×10^4
4	4.0×10^2	2.5×10^3	1.8×10^4
5	N.A.*	N.A.*	5.5×10^5
6	3.0×10^2	5.1×10^2	1.1×10^6
7	3.0×10^2	6.3×10^2	2.4×10^4
8	6.9×10^2	1.3×10^3	1.2×10^4

* Complex interlinked ferritic laths.
Reliable grain size cannot be determined.

Table 10

Summary of Grain Size Measurements

(Gleeble, $t_{8/5}$ = 128s)

	Volumetric Grain Size (g/mm^3)		
Designation	Centre	Middle	Edge
1	18	62	6.7×10^5
2	15	74	3.9×10^6
3	12	51	1.9×10^6
4	30	740	6.4×10^6
5	15	1.9×10^4	5.4×10^5
6	32	6.5×10^3	1.3×10^6
7	18	7.9×10^2	8.9×10^5
8	22	3.5×10^2	6.2×10^4

Table 11

Microstructure and Corrosion Groove Depth of HAZ

Sample	GF%	AF%	SF%	GP%	TM%	SM%	Depth (mm)
1-1kJ/mm	15	47	20	18	0	0	.16
1-3kJ/mm	47	29	21	3	0	0	.14
1a-1kJ/mm			NA				.18
1a-3kJ/mm			NA				.16
2-1kJ/mm	12	66	16	6	0	0	.16
2-3kJ/mm	19	69	12	0	0	0	.15
3a-1kJ/mm			NA				.35
3a-3kJ/mm			NA				.22
3-1kJ/mm	5	0	13	0	53	29	.24
3-3kJ/mm	14	69	15	2	0	0	.24
4-1kJ/mm	4	0	28	0	52	16	.25
4-3kJ/mm	16	54	30	0	0	0	.20
5-1kJ/mm	51	33	16	0	0	0	.21
5-3kJ/mm	78	16	6	0	0	0	.18
6-1kJ/mm	48	39	12	0	0	0	.41
6-3kJ/mm	45	32	23	0	0	0	.36
7-1kJ/mm	20	68	12	0	0	0	.23
7-3kJ/mm	53	42	5	0	0	0	.36
8-1kJ/mm	22	61	17	0	0	0	.49
8-1akJ/mm	22	61	17	0	0	0	.49
8-3kJ/mm	35	53	12	0	0	0	.55

where GF= grain boundary ferrite
AF= acicular ferrite
SF= sideplate ferrite
GP= degenerated pearlite

Table 12

Summary of Corrosion Results of the Gleeble Simulated Samples

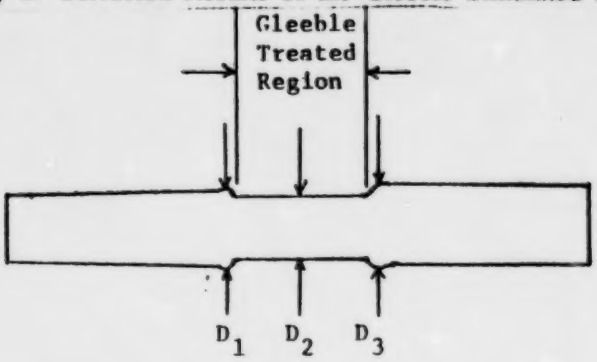

Corrosion Tested Gleeble Specimen

Steel	$t_{8.5}$ s	Diameter of Gleeble Treated Specimens at Locations Shown, mm			
		D_1	D_2	D_3	D_m*
1	20	8.839	8.585	8.839	0.25
1	128	9.119	9.119	9.233	0.06
2	20	9.017	8.763	9.017	0.25
2	128	8.331	7.874	8.407	0.50
3	20	9.042	8.839	9.017	0.19
3	128	8.763	8.661	9.017	0.23
4	20	8.153	7.823	8.204	0.36
4	128	8.484	8.280	8.890	0.41
5	20	9.093	8.915	9.144	0.20
5	128	8.179	7.671	8.331	0.58
6	20	9.017	8.839	9.042	0.19
6	128	8.611	8.433	8.992	0.37
7	20	8.687	8.636	8.839	0.13
7	128	8.890	8.788	9.017	0.17
8	20	9.119	8.763	9.195	0.39
8	128	-	-	-	-

* $D_m = \frac{D_3 + D_1}{2} - D_2$

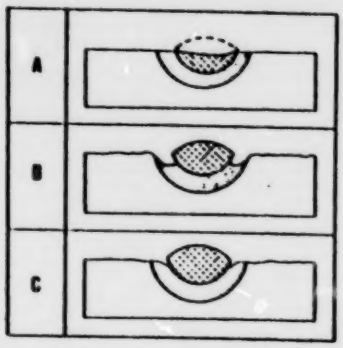

Figure 1. Showing three types of Weldment corrosion a) Weld metal corrosion, b) HAZ corrosion, c) fusion line attack.

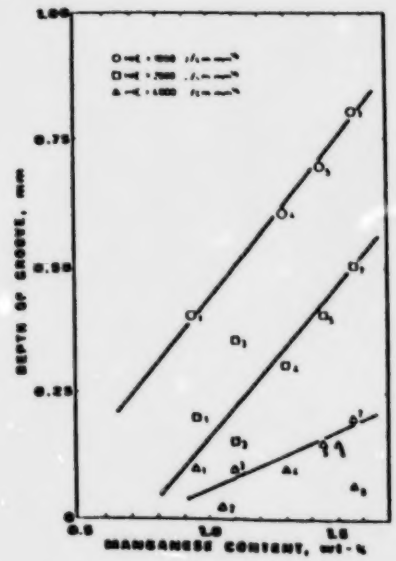

Figure 2. Showing the effect of Mn and heat input on HAZ corrosion on various C-Mn steels (after Saarinen (2)).

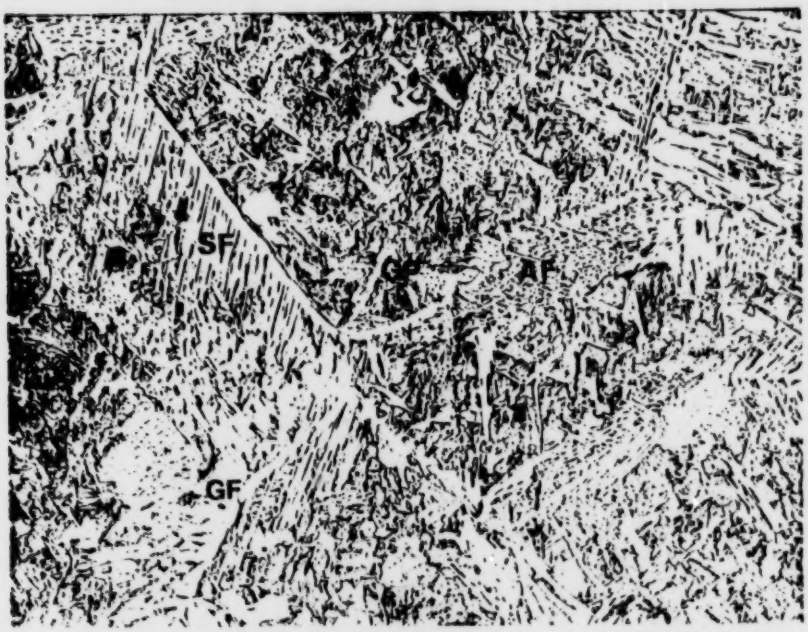

Figure 3. Typical microstructures in Gleeble sample of steel 1 (t_{8-5} = 20 s), Mag. 200 X.

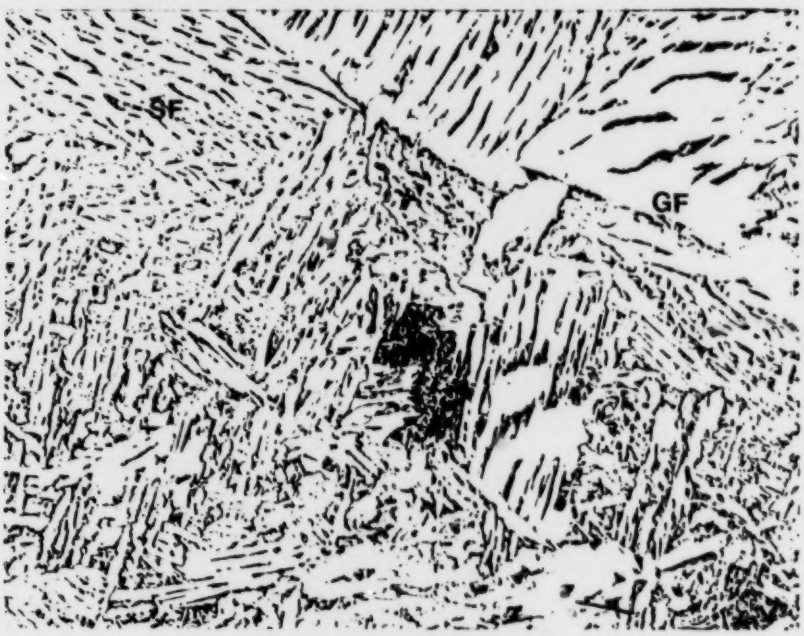

Figure 4. Typical microstructures observed in HAZ of steel 3 at 3 kJ/mm heat input, Mag. 500 X.

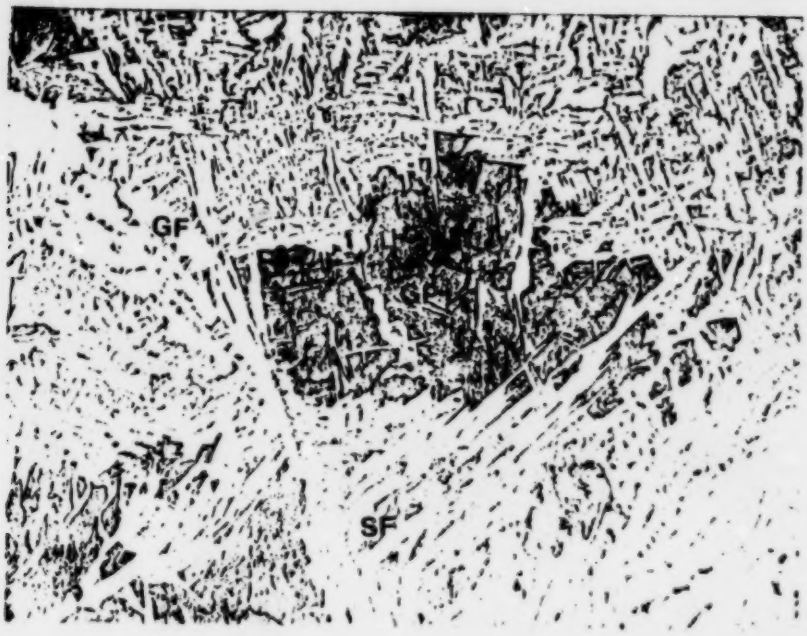

Figure 5. Typical microstructures observed in steel 1 Gleeble sample ($t_{8\text{-}5}$ = 20 s) Mag. 750 X.

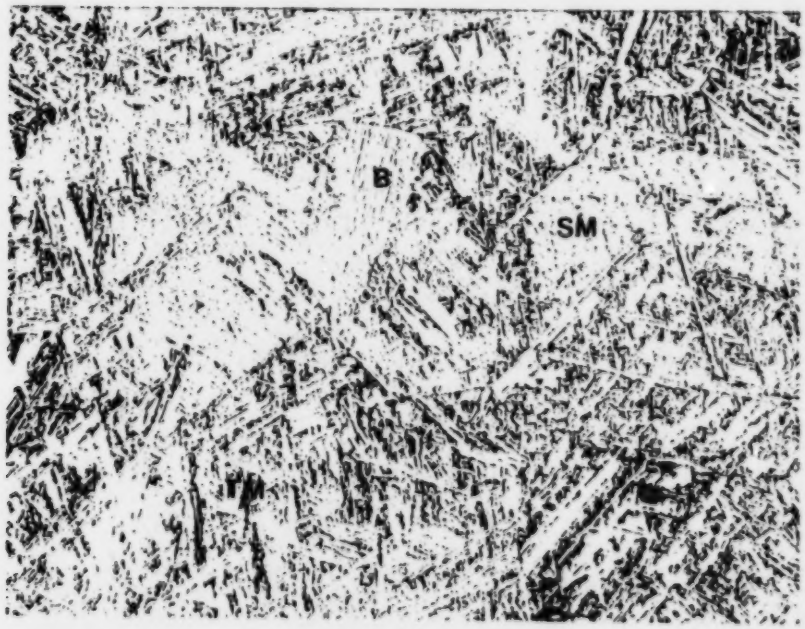

Figure 6. Typical microstructures observed in steel 8 Gleeble samples ($t_{8\text{-}5}$ = 5 s) Mag. 250 X.

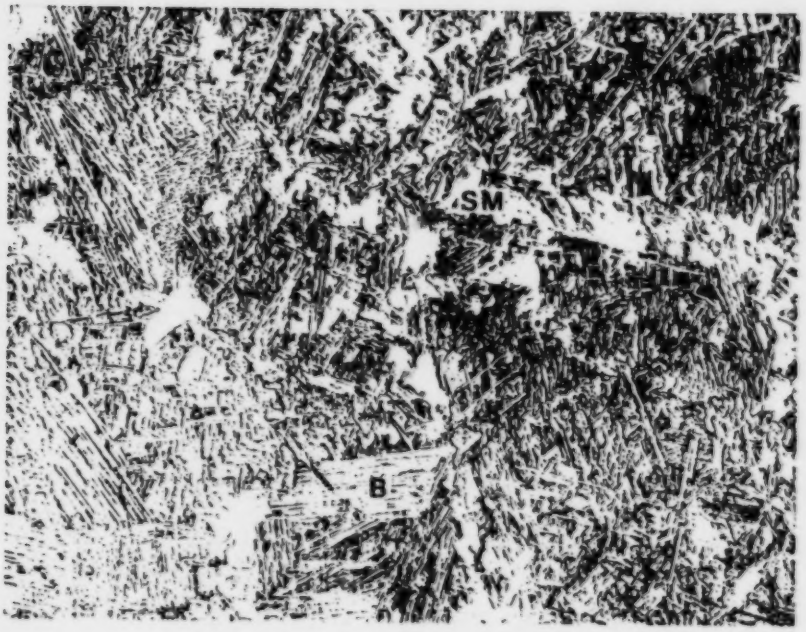

Figure 7. Typical microstructures observed in steel 1, Gleeble sample ($t_{8/5}$ = 5 s). Mag. 250 X.

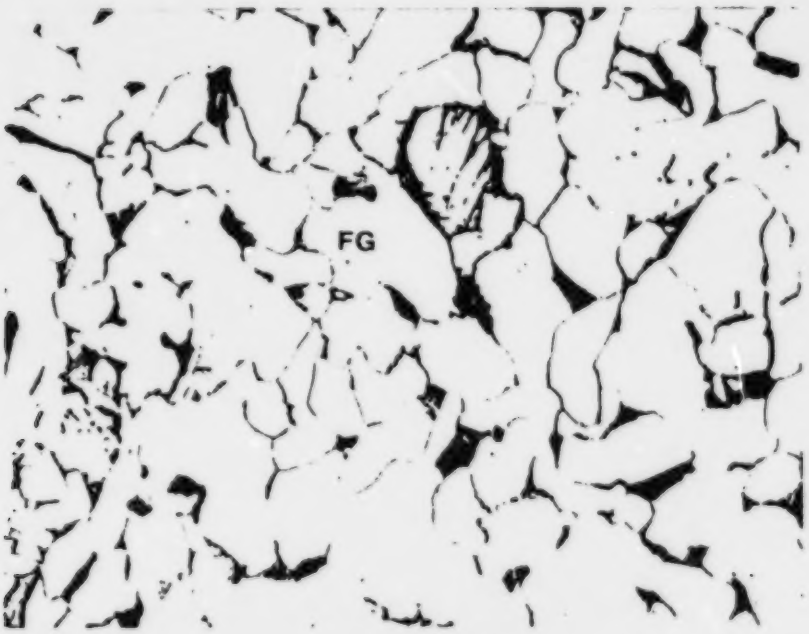

Figure 8. Typical microstructures observed at edge of HAZ, steel 1, heat input = 3 kJ/mm. Mag 1000 X.

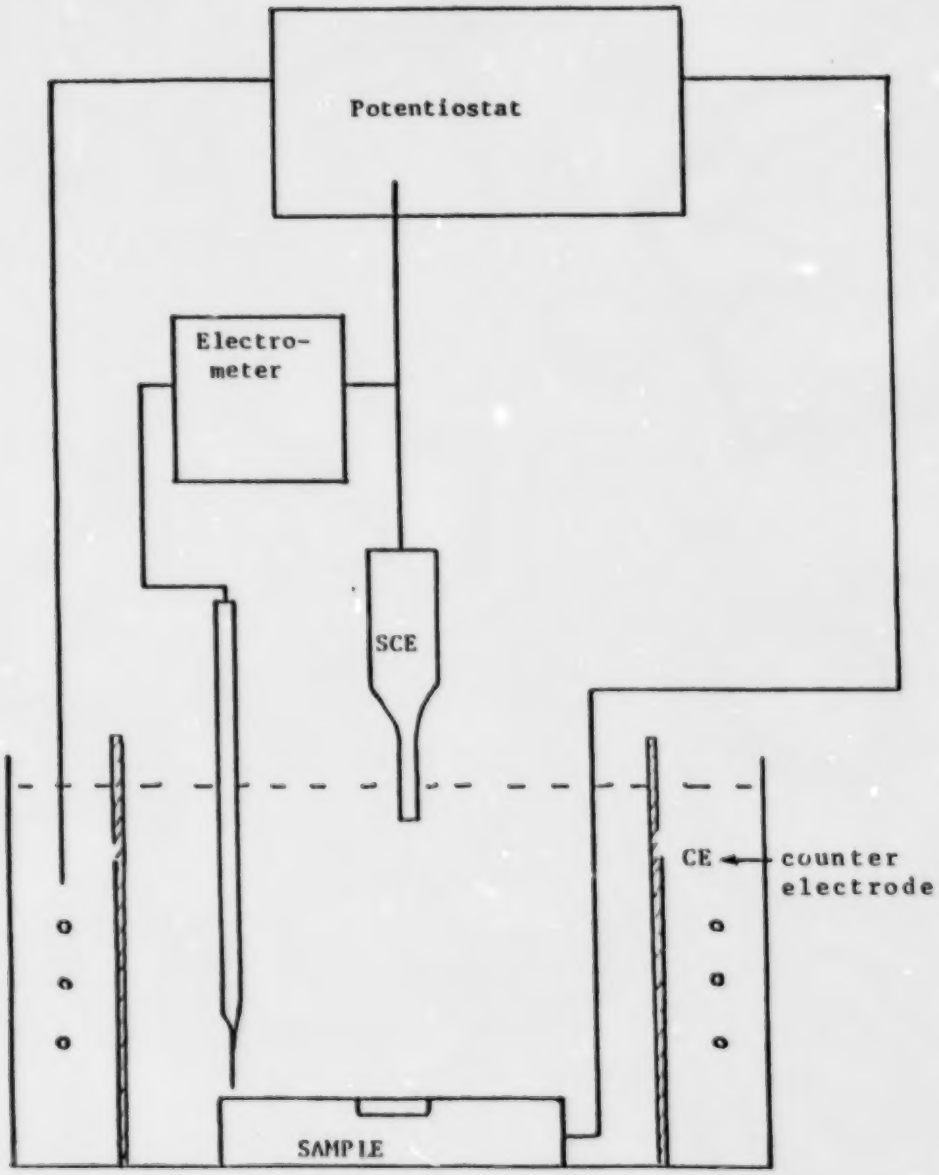

Figure 9. Experimental apparatus used in Micro-electrode testing.

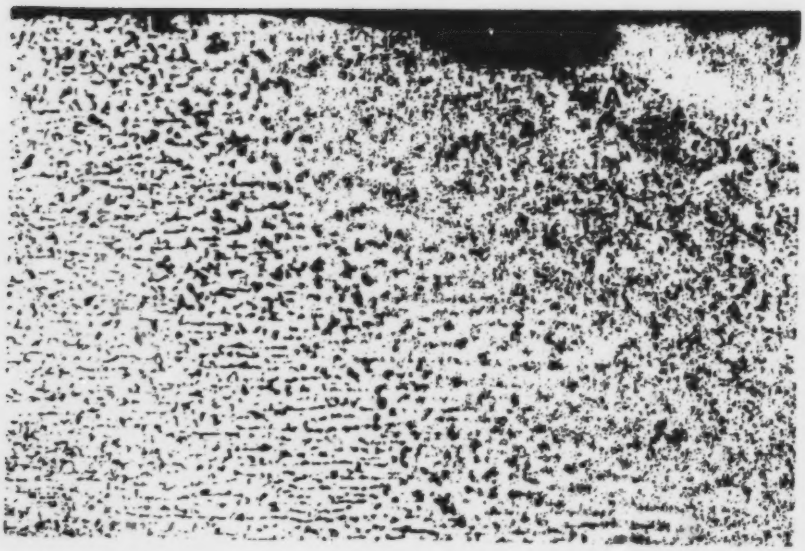

Figure 10a. As-corroded 1 - 1 kJ/mm (40x).

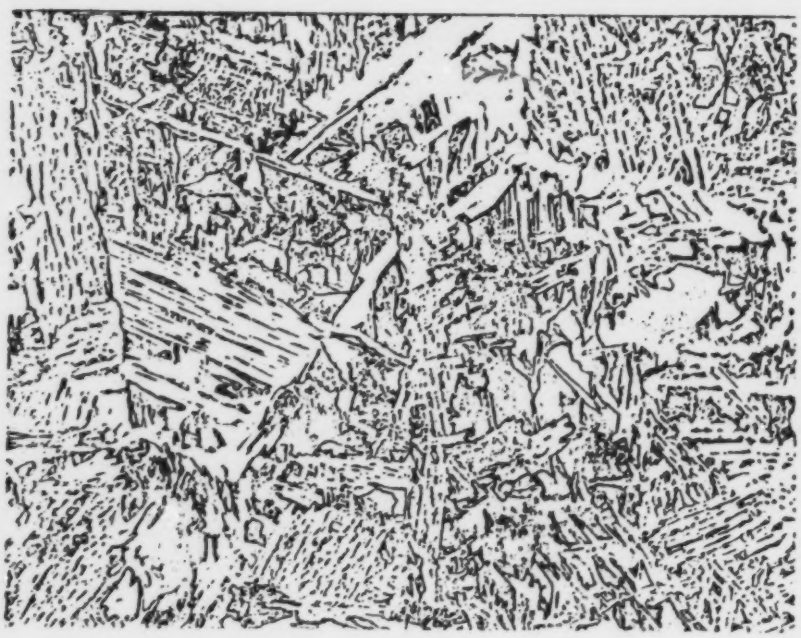

Figure 10b. Microstructure of Region A of Figure 10a for 1-1kJ/mm (500 X).

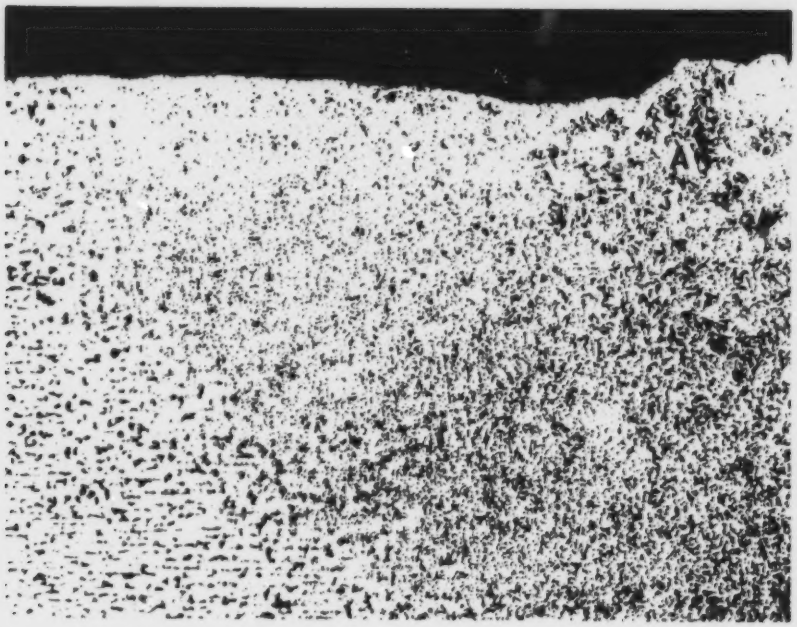

Figure 11a. As-corroded 1-3 kJ/mm (40X).

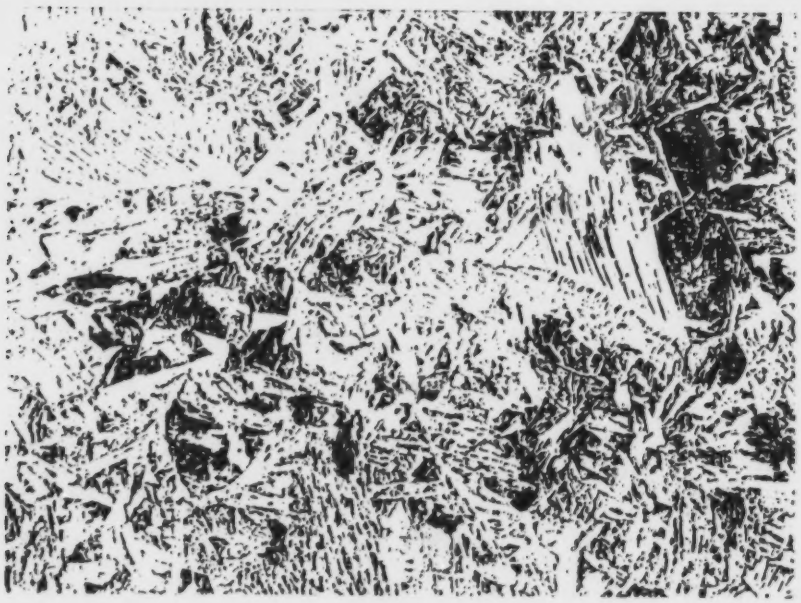

Figure 11b. Microstructure of the grain growth region A for 1-3 kJ/mm (200 X).

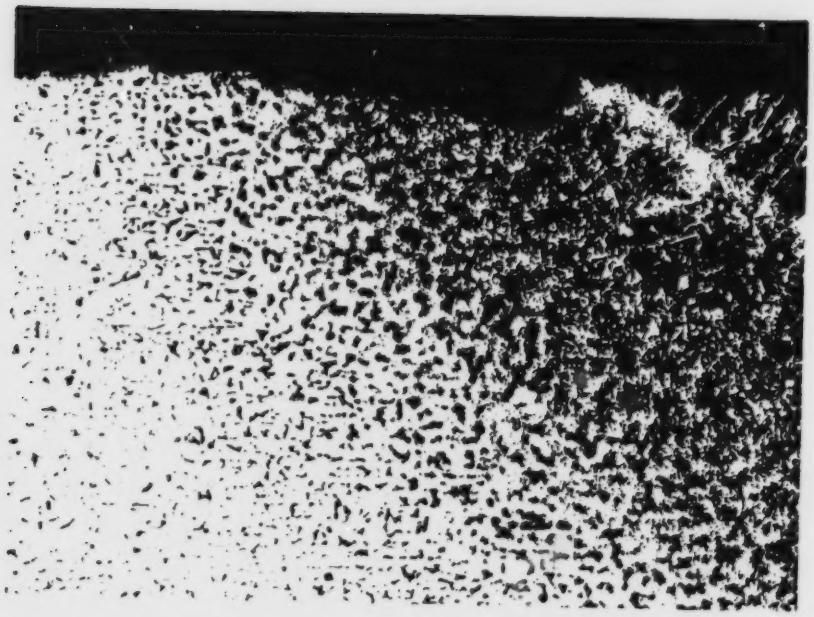

Figure 12a. As-corroded 1a-1 kJ/mm (40 X).

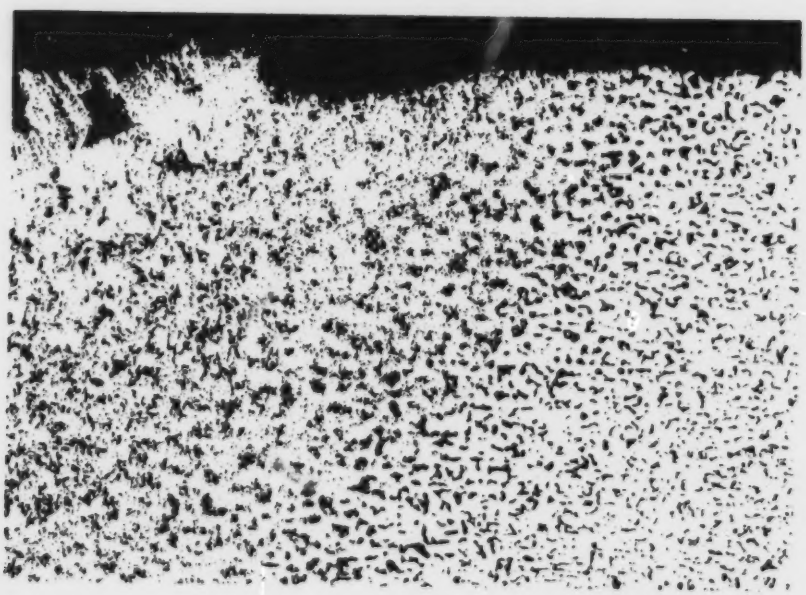

Figure 12b. As-corroded 1a - 3 kJ/mm (40 X).

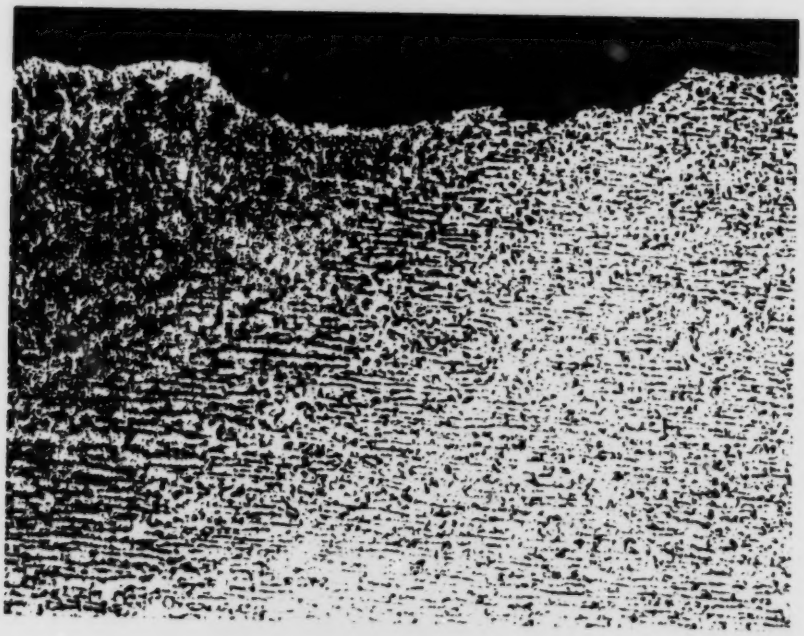

Figure 13a. As-corroded 3-1 kJ/mm (40 X).

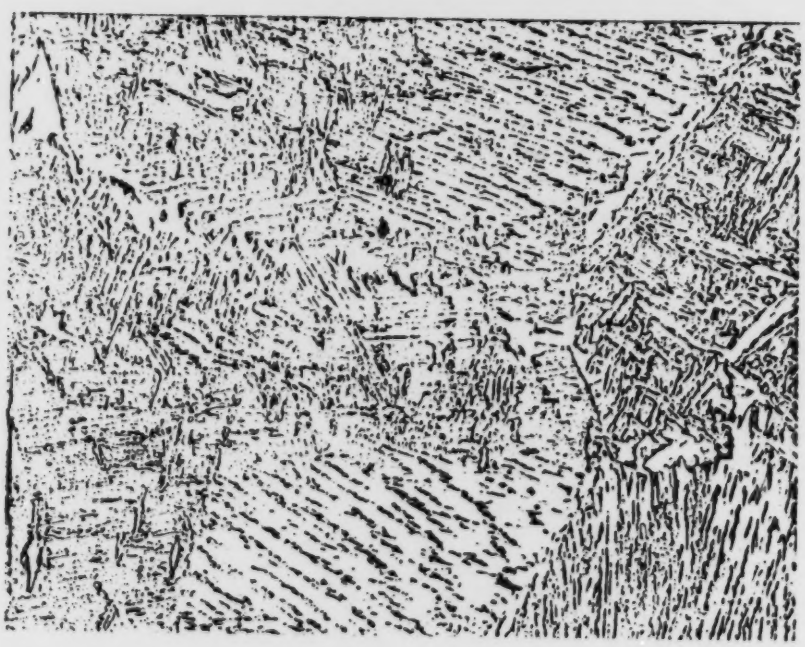

Figure 13b. Microstructure of Region A of Figure 13a (500 X).

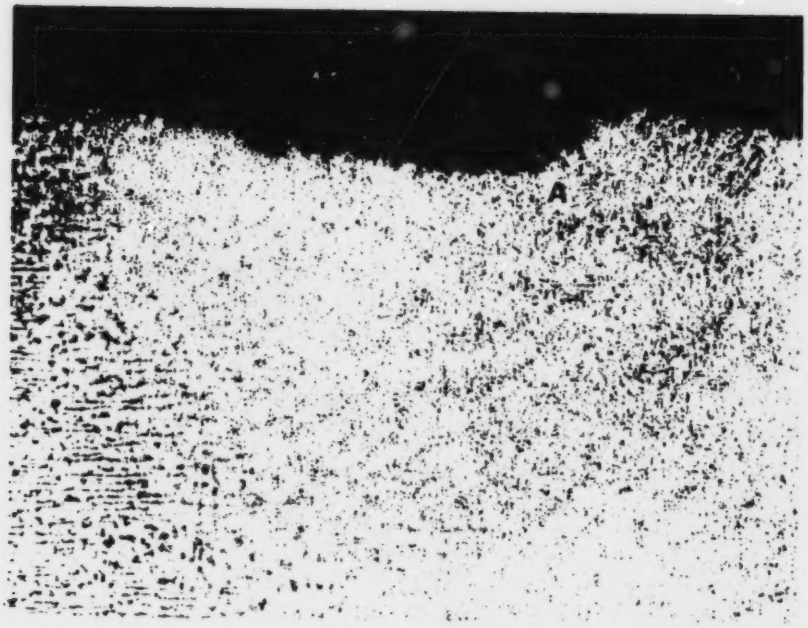

Figure 14a. As-corroded 3-3kJ/mm (40 X)

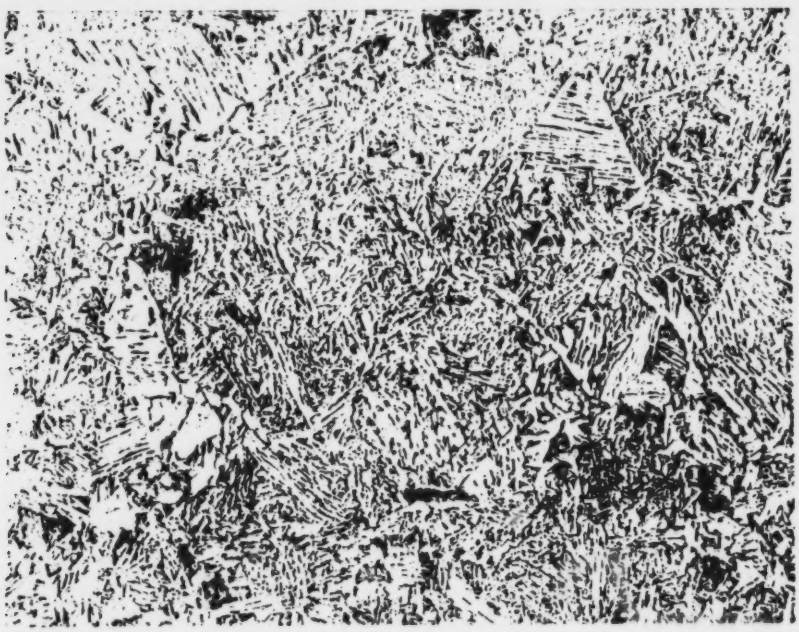

Figure 14b. Microstructure of Region A of Figure 14a for 3-3 kJ/mm (200 X).

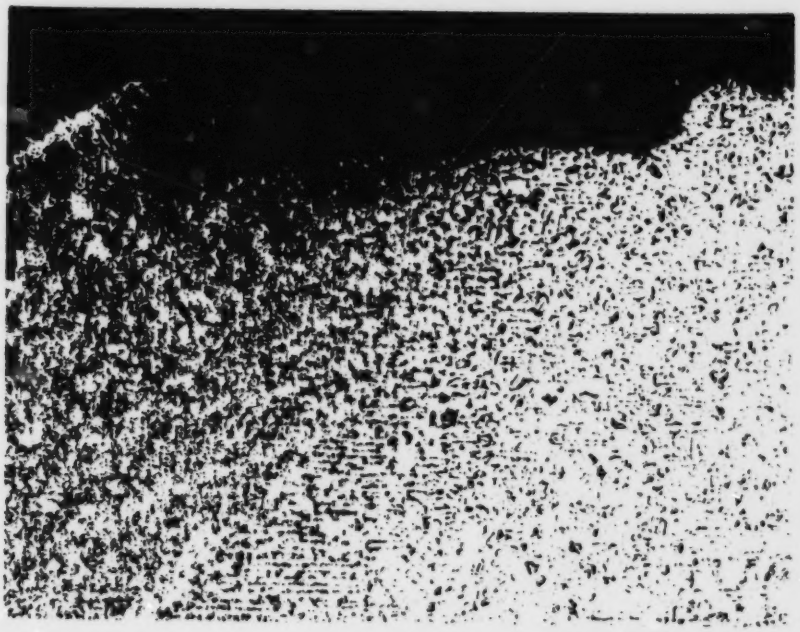

Figure 15a. As-corroded 3a-1 kJ/mm (40 X).

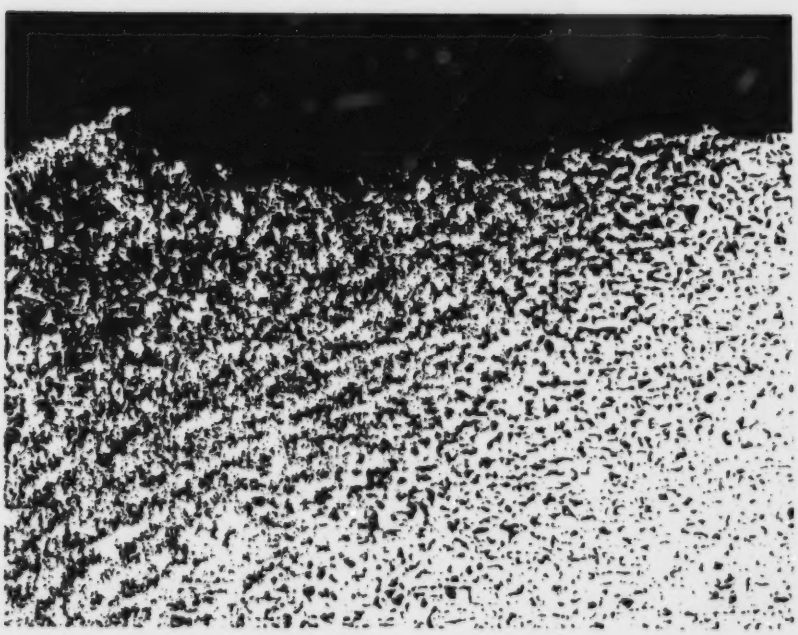

Figure 15b. As-corroded 3a-3kJ/mm (40 X).

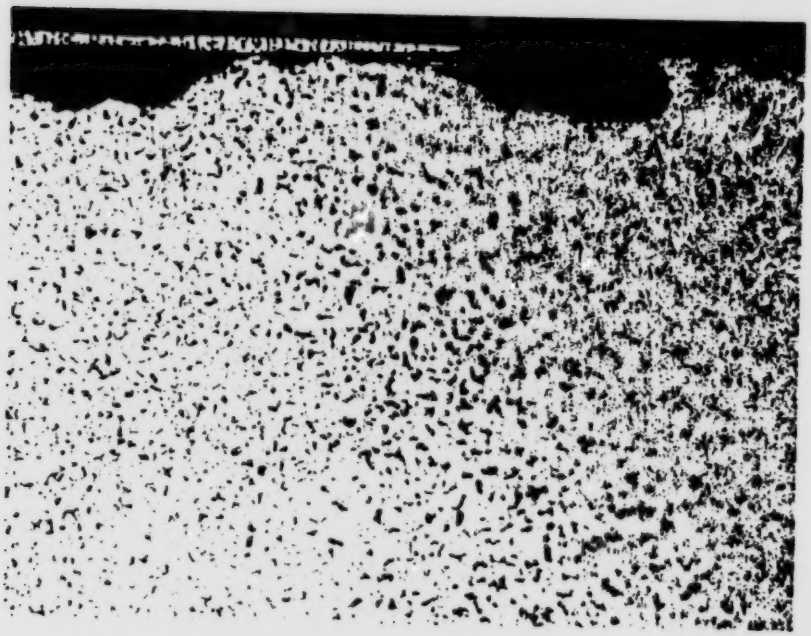

Figure 16a. As-corroded 5-1 kJ/mm (40 X).

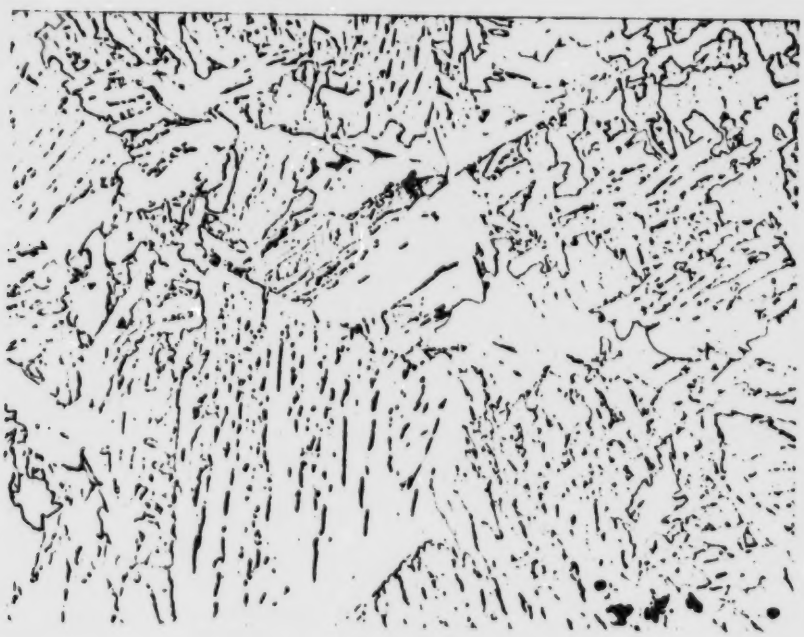

Figure 16b. Microstructure of Region A of Figure 16a for 5-1 kJ/mm (500 X).

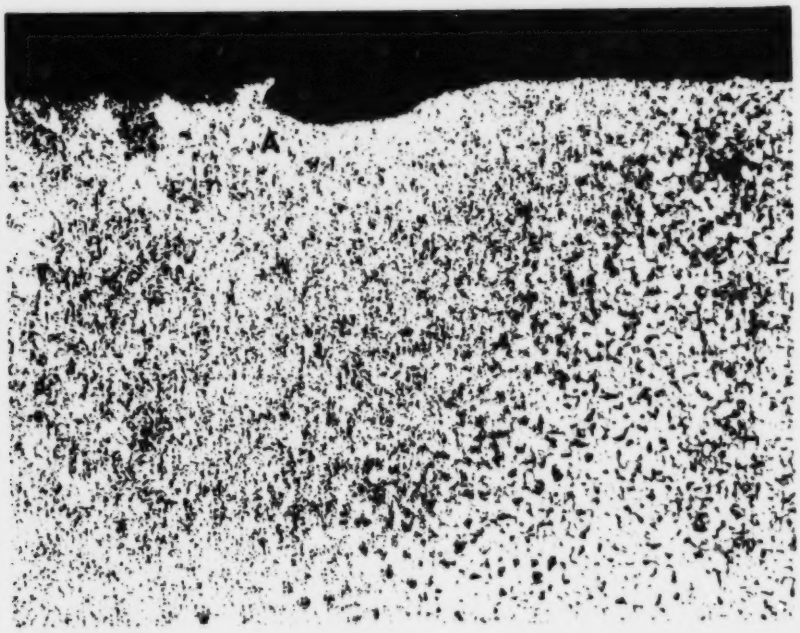

Figure 17a. As-corroded 5-3 kJ/mm (40 X).

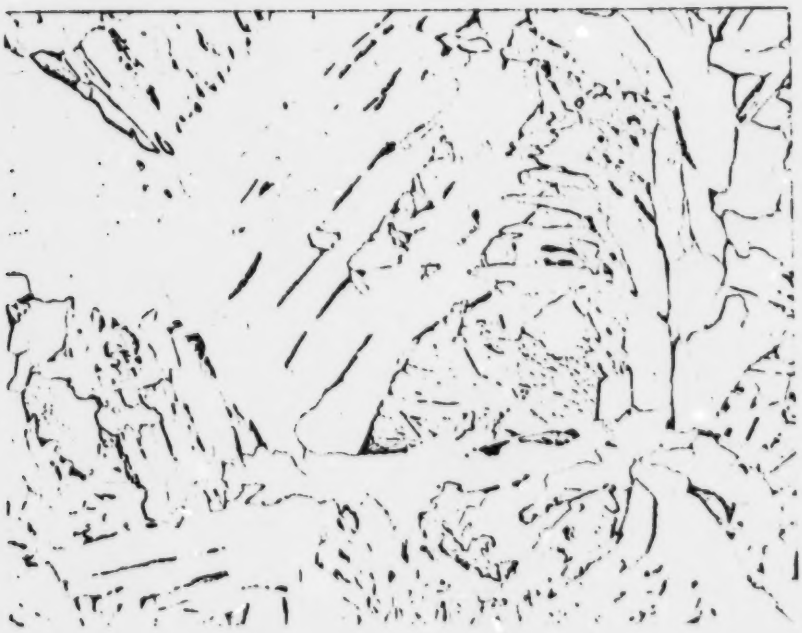

Figure 17b. Microstructure of Region A of Figure 17a for 5-3 kJ/mm (500 X).

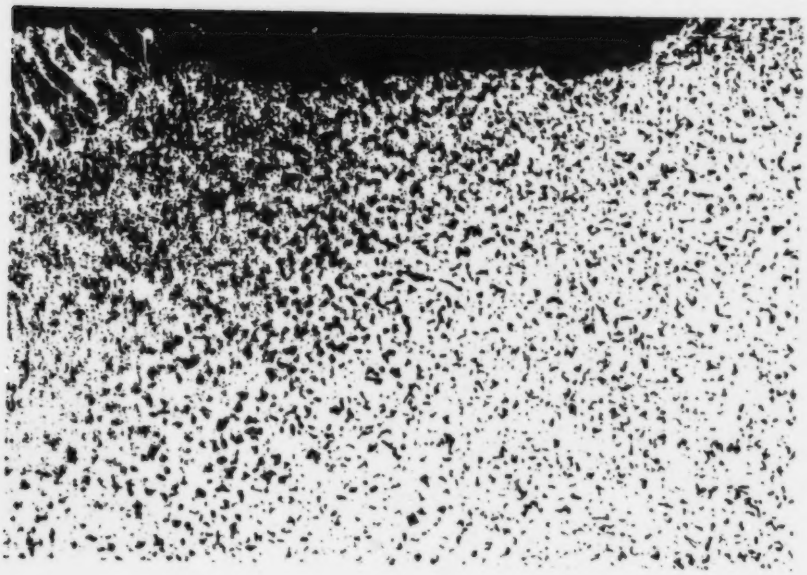

Figure 18a. As-corroded 7-1 kJ/mm (40 X).

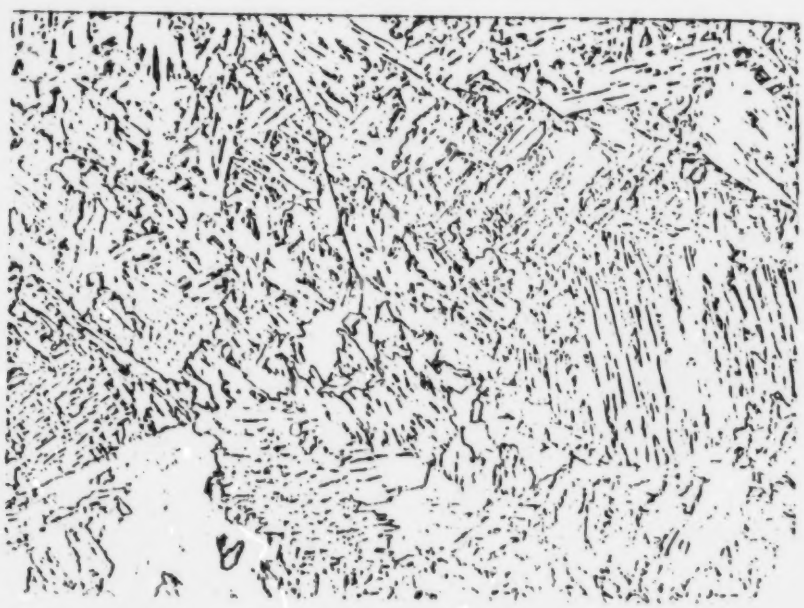

Figure 18b. Microstructure of Region A of Figure 18a for 7-1 kJ/mm (500 X).

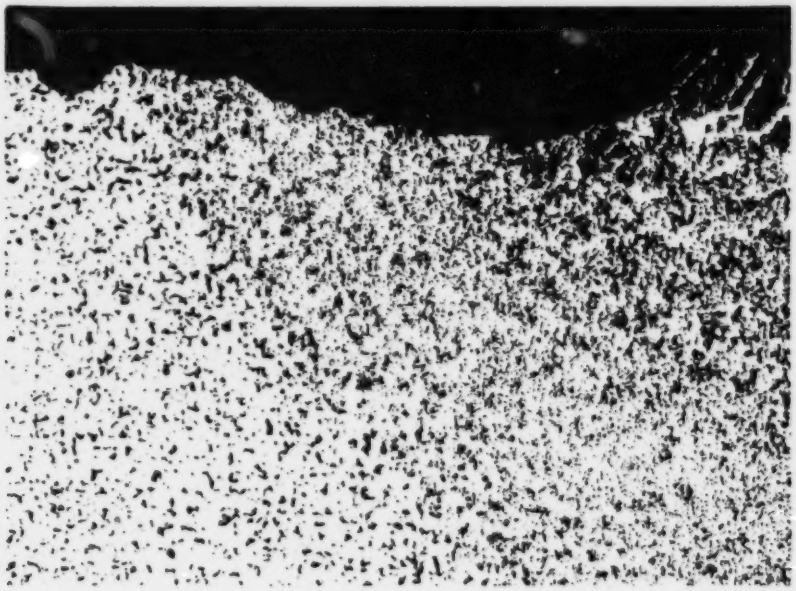

Figure 19a. As-corroded 7-3 kJ/mm (40 X).

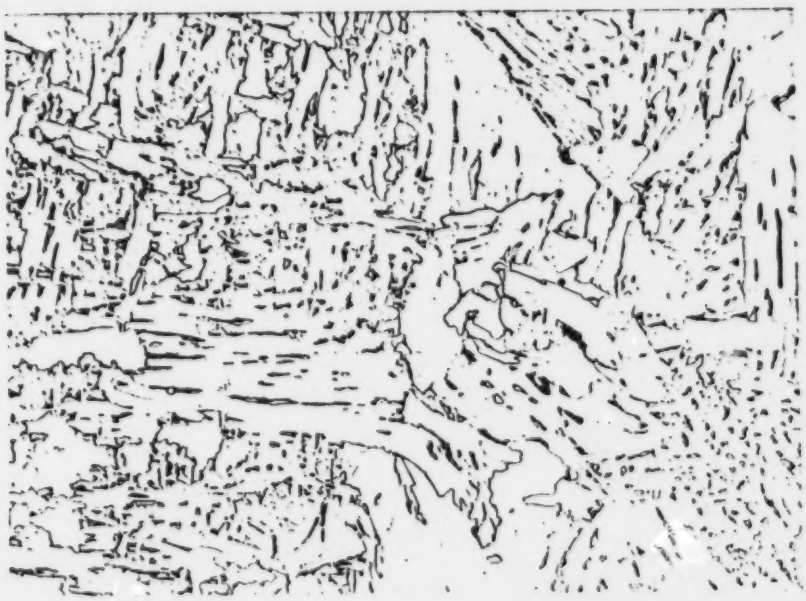

Figure 19b. Microstructure of Region A of Figure 19a for 7-3 kJ/mm (500 X)

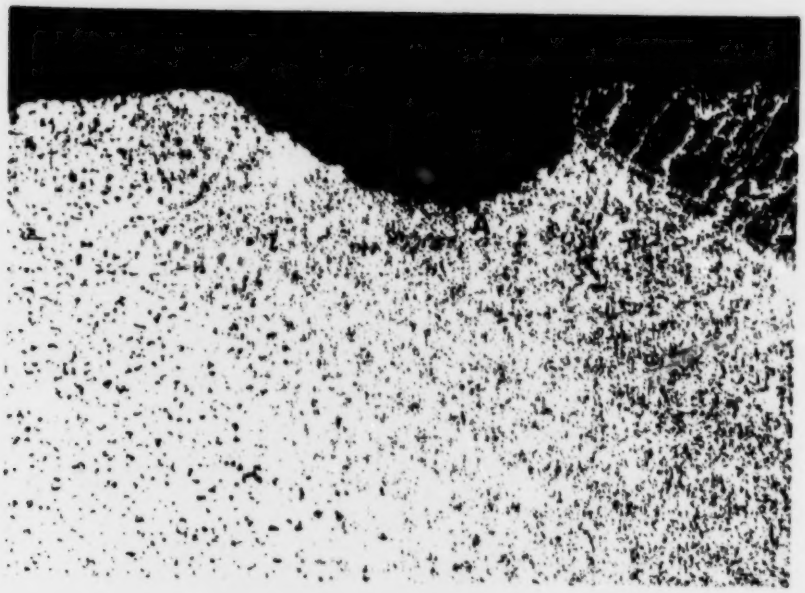

Figure 20a. As-corroded 6-1 kJ/mm (40 X).

Figure 20b. Microstructure of Region A of Figure 20a for 6-1 kJ/mm (500 X).

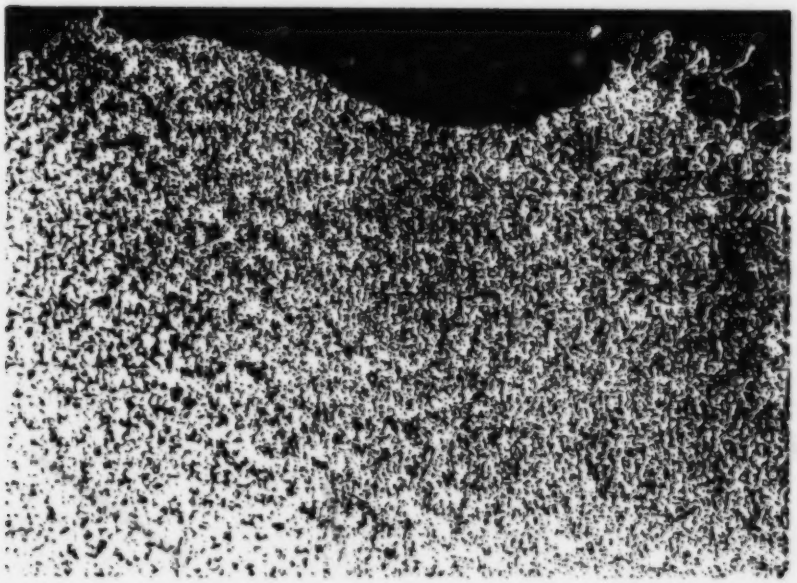

Figure 21a. As-corroded 6-3 kJ/mm (40 X).

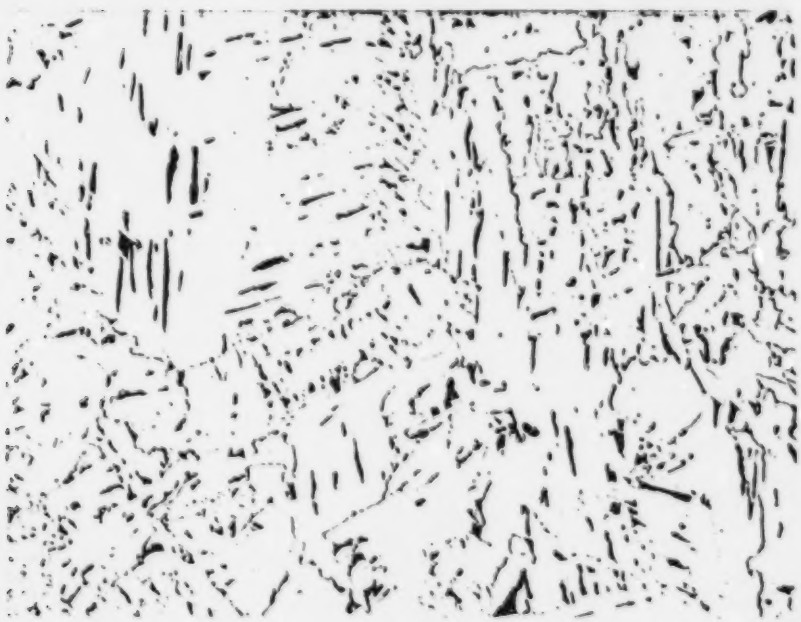

Figure 21b. Microstructure of Region B of Figure 21a for 6-3 kJ/mm (500 X).

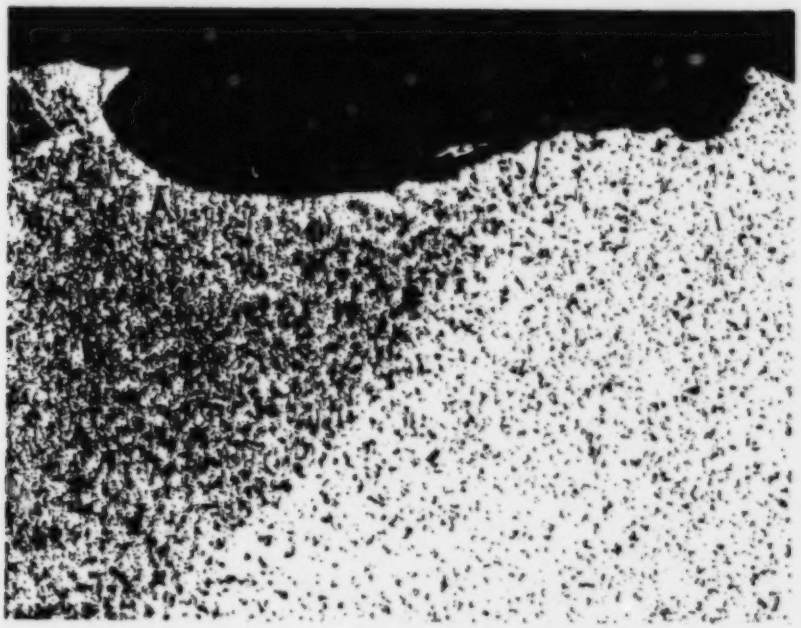

Figure 22a. As-corroded 8-1 kJ/mm (40 X).

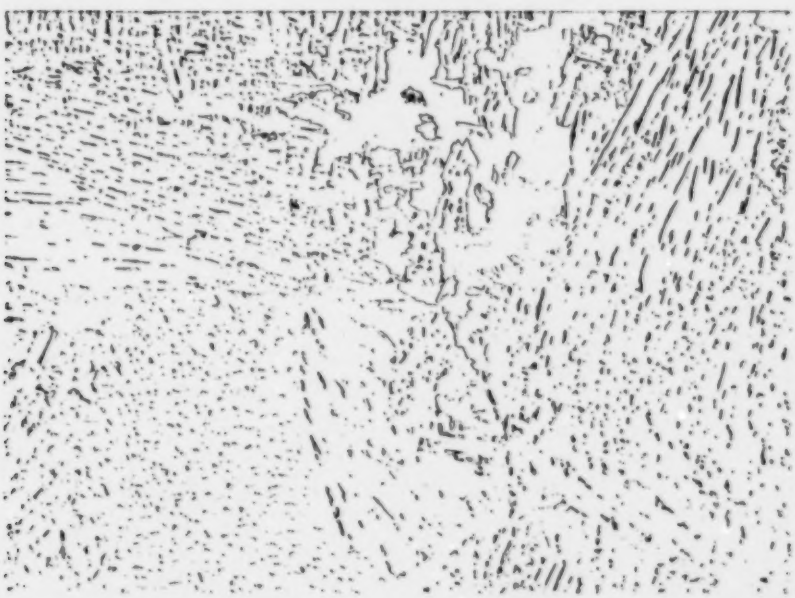

Figure 22b. Microstructure of Region A of Figure 22a for 8-1 kJ/mm (500 X).

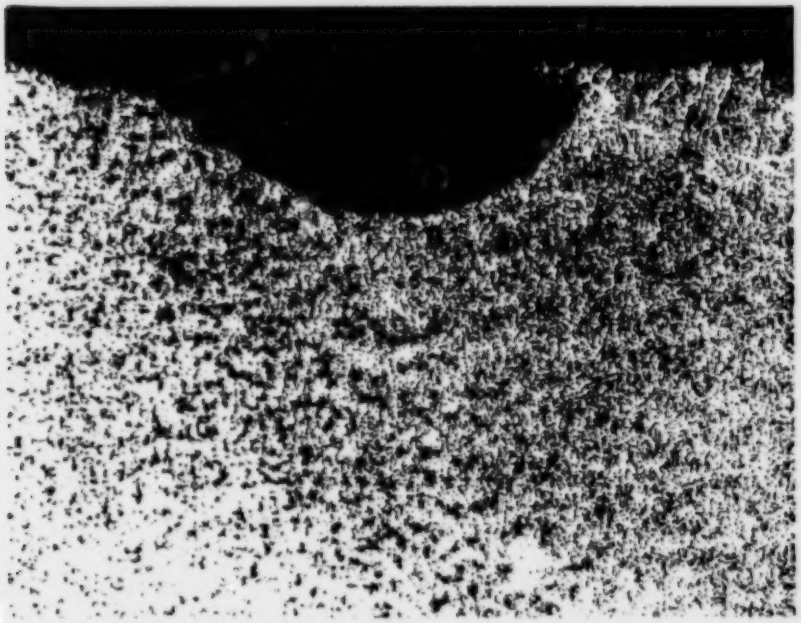

Figure 23a. As-corroded 8-3 kJ/mm (40 X).

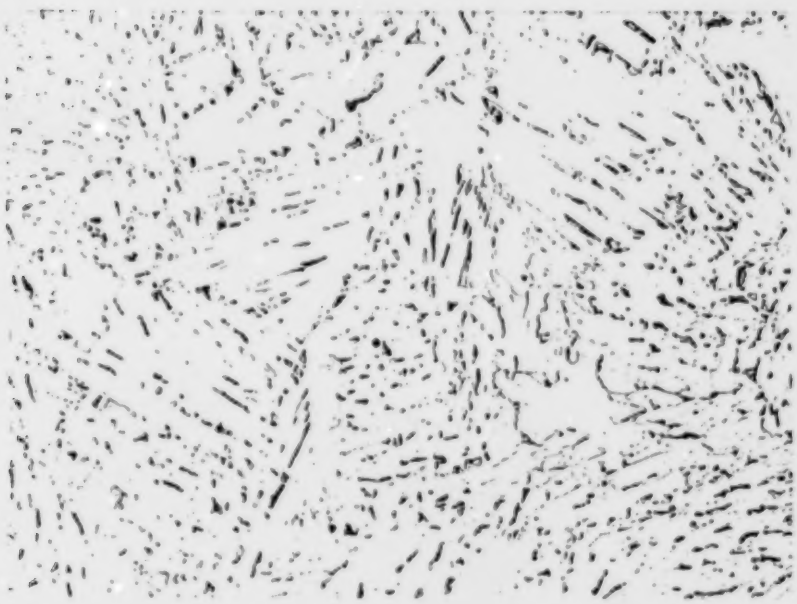

Figure 23b. Microstructure of Region B of Figure 23a for 8-3 kJ/mm (500 X).

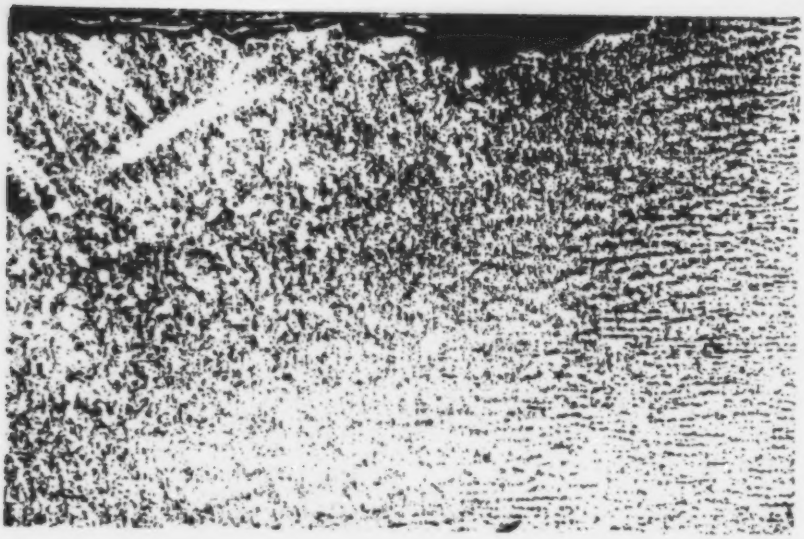

Figure 24a. As-corroded 2-1 kJ/mm (40 X).

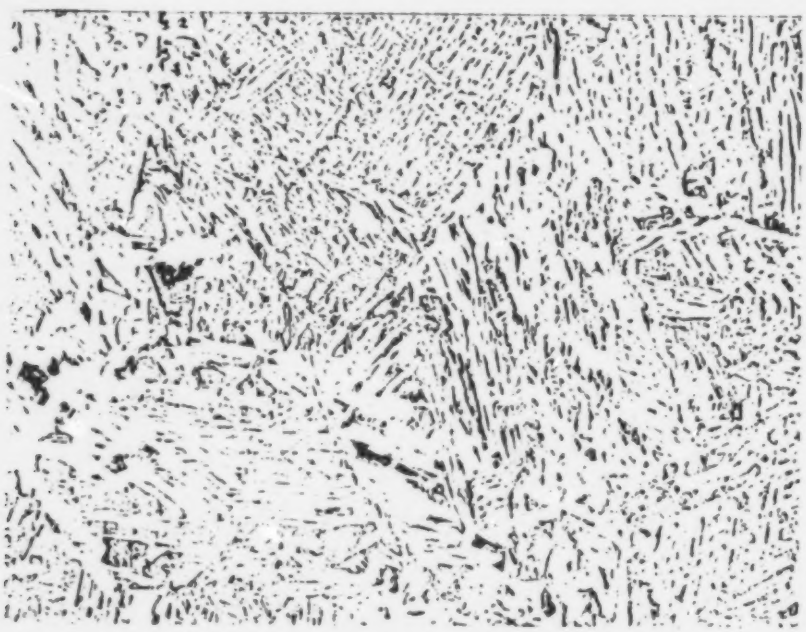

Figure 24b. Microstructure of Region A of Figure 24a for 2-1 kJ/mm (500 X).

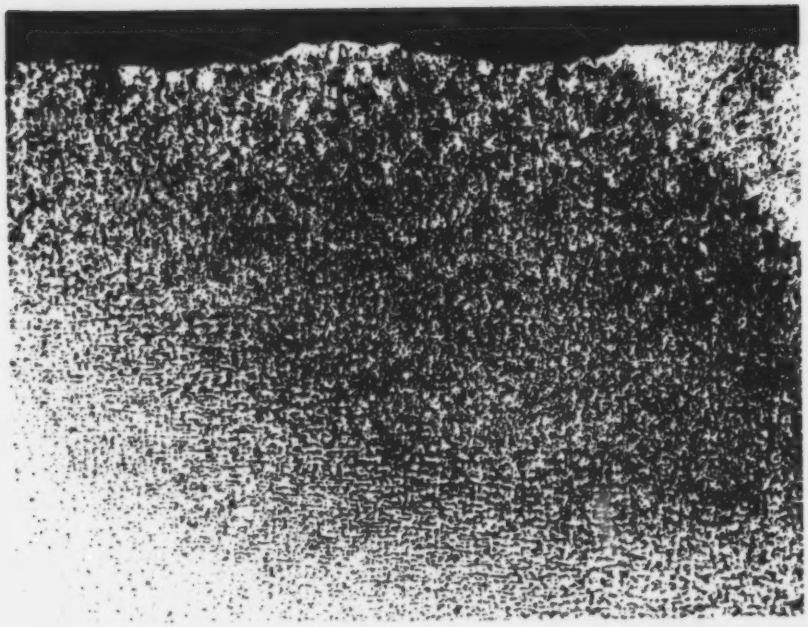

Figure 25a. As-corroded 2-3 kJ/mm (16 X).

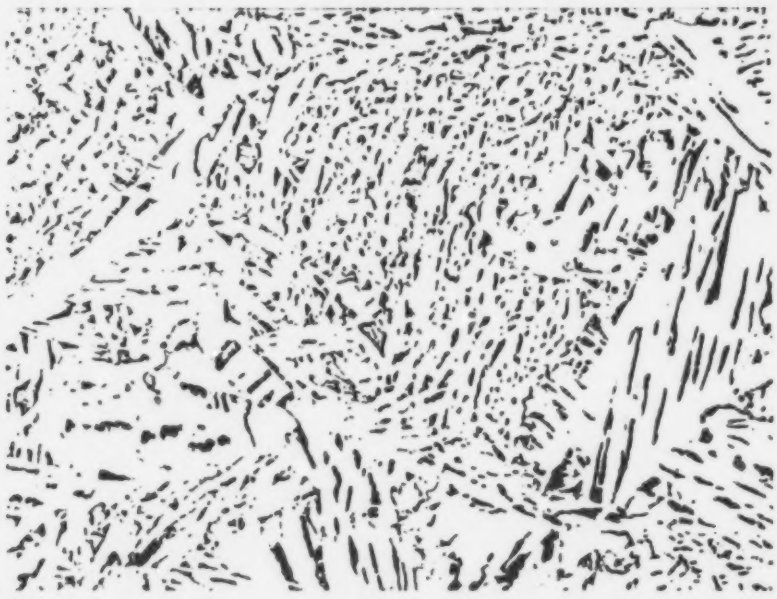

Figure 25b. Microstructure of Region A of Figure 25a for 2-3 kJ/mm (500 X).

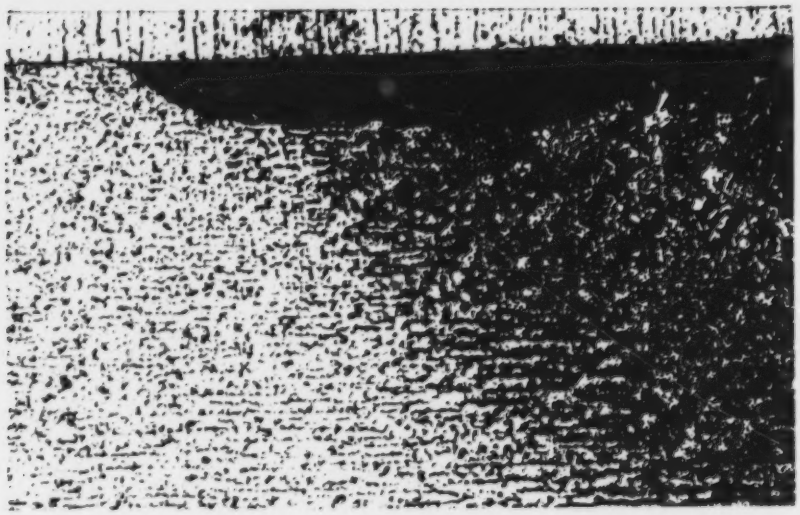

Figure 26a. As-corroded 4-1 kJ/mm (40 X).

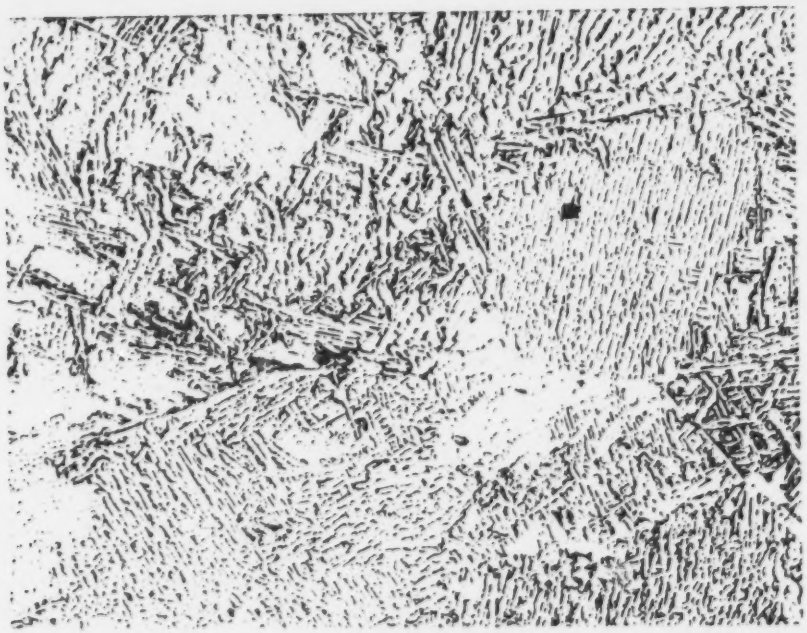

Figure 26b. Microstructure of Region A of Figure 26a for 4-1 kJ/mm (500 X).

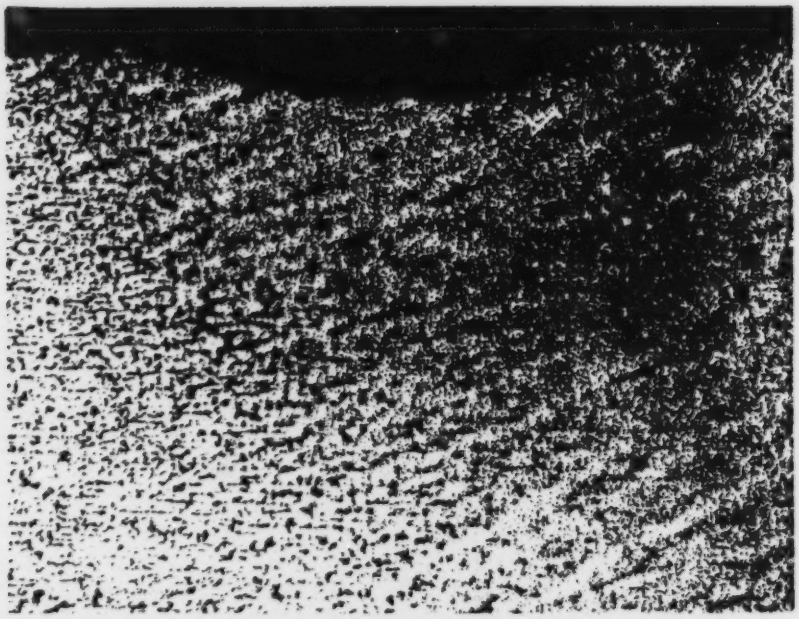

Figure 27a. As-corroded 4-3 kJ/mm (40 X).

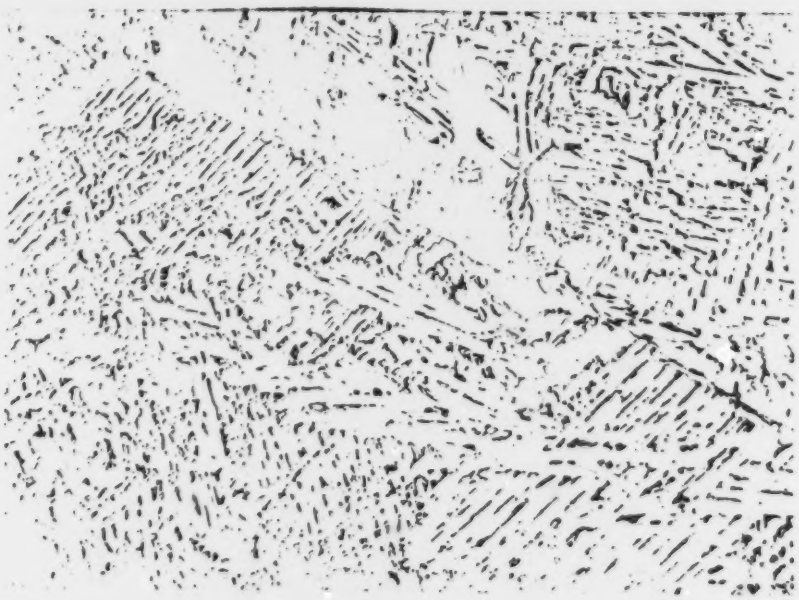

Figure 27b. Microstructure of region A of Figure 27a for 4-3 kJ/mm (500 X).

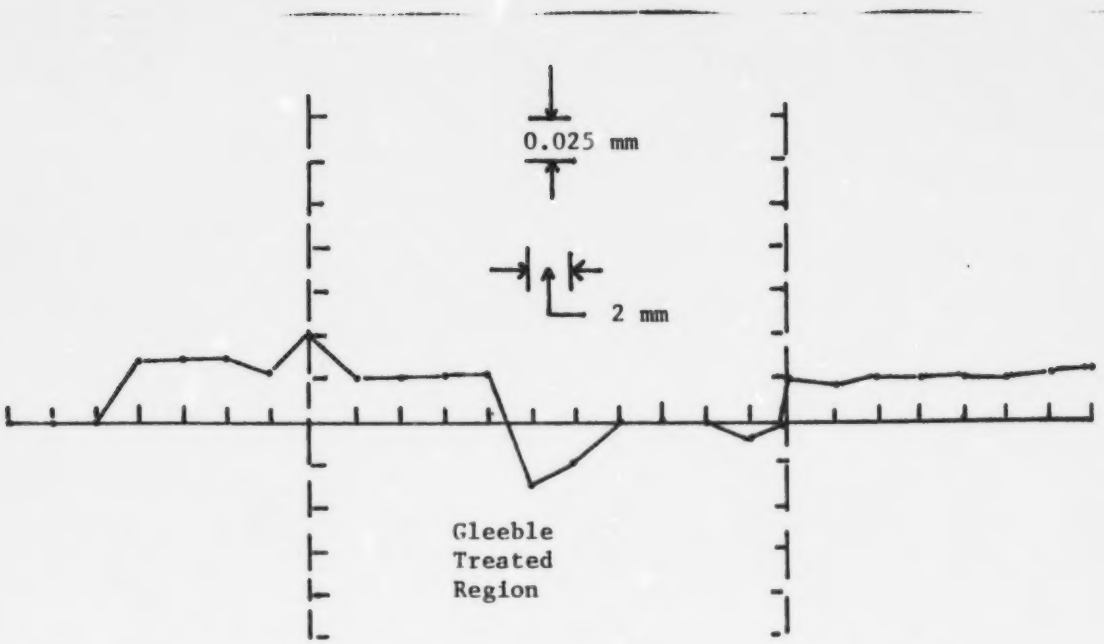

Figure 28. Gleeble specimen profile after corrosion. Sample 3-20s. Specimen checked longitudinally (for 50 mm), at a randomly selected circumference (50 X).

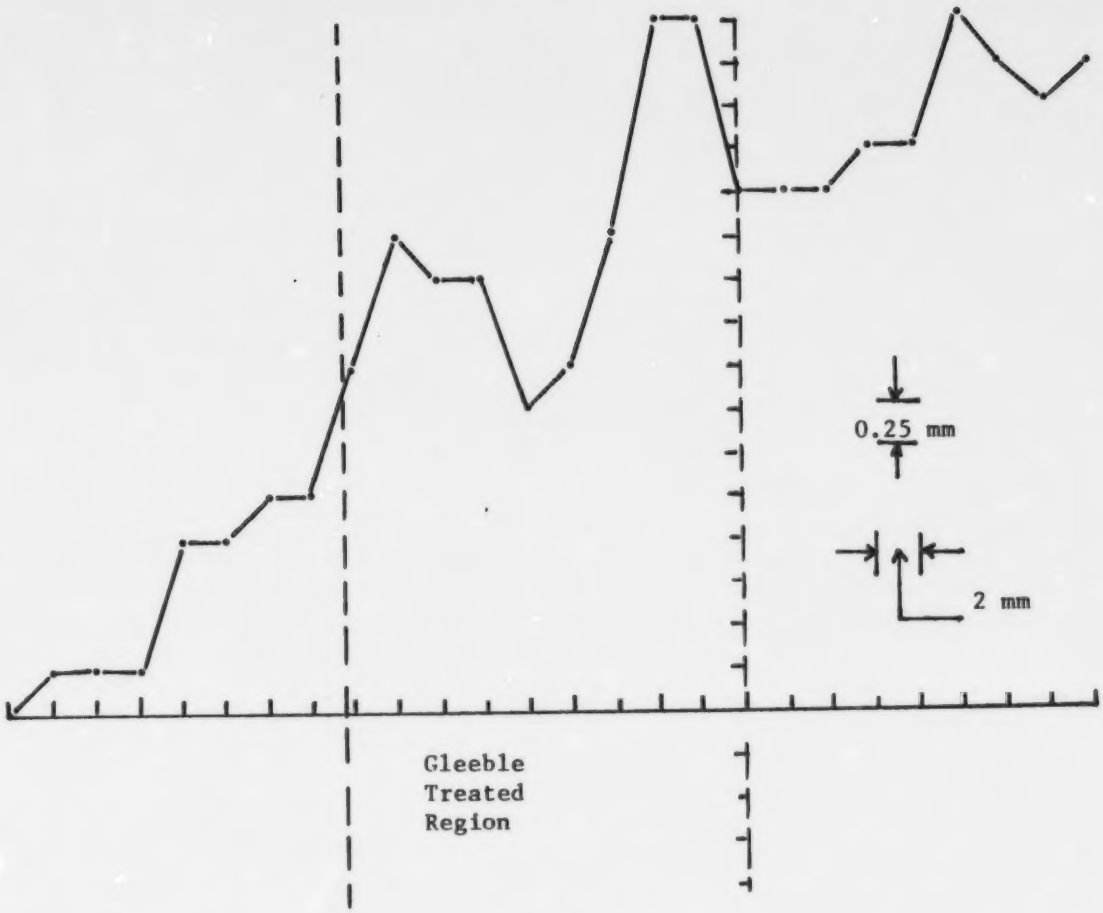

Figure 29. Gleeble specimen profile after corrosion - Sample 4 - 20s. Specimen checked longitudinally (for 50 mm) at a randomly selected circumference (50 X).

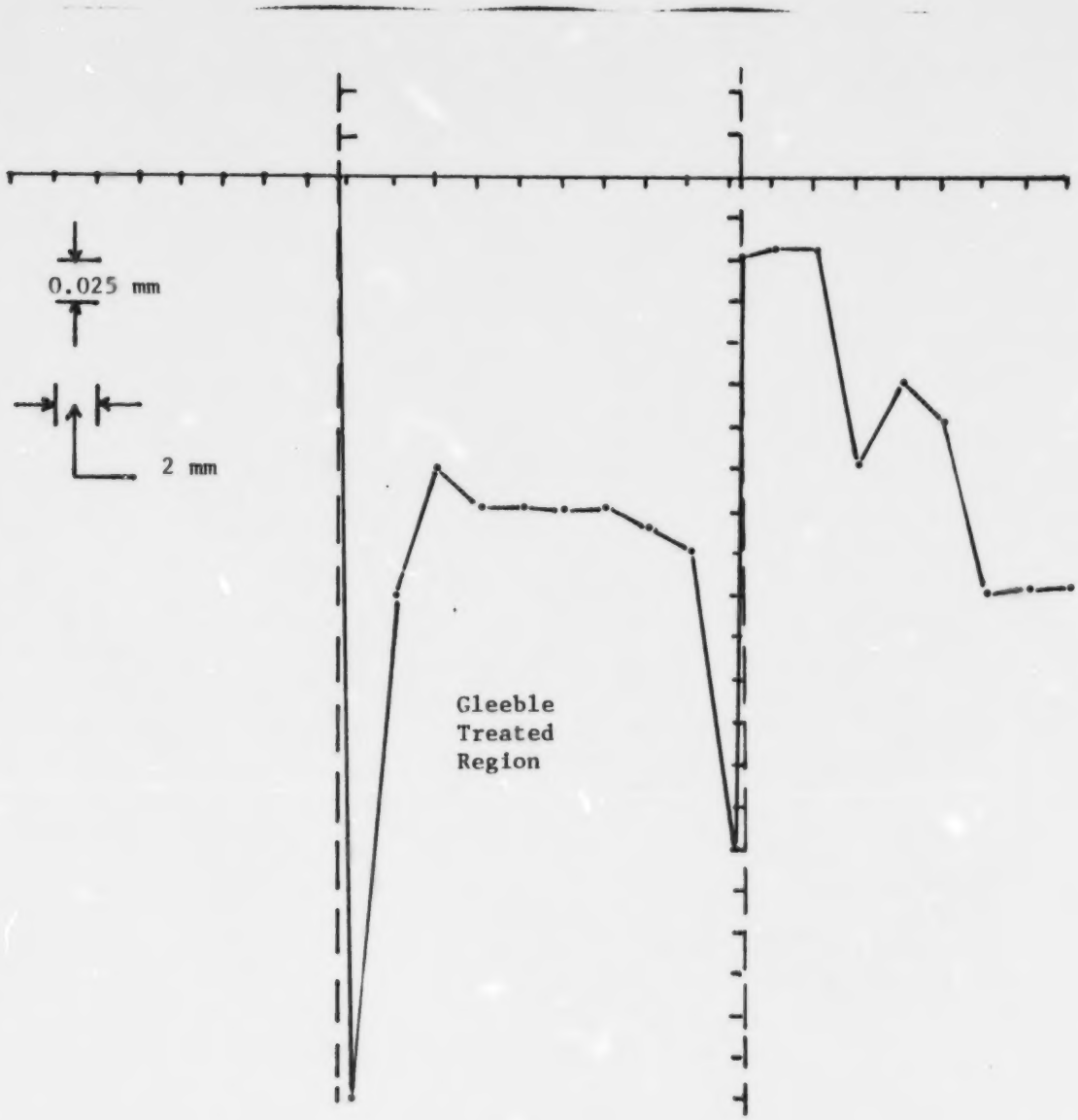

Figure 30. Profile of Gleeble specimen after corrosion - Sample 8-20s. Specimen checked longitudinally (for 50 mm) at a randomly selected circumference (50 X).

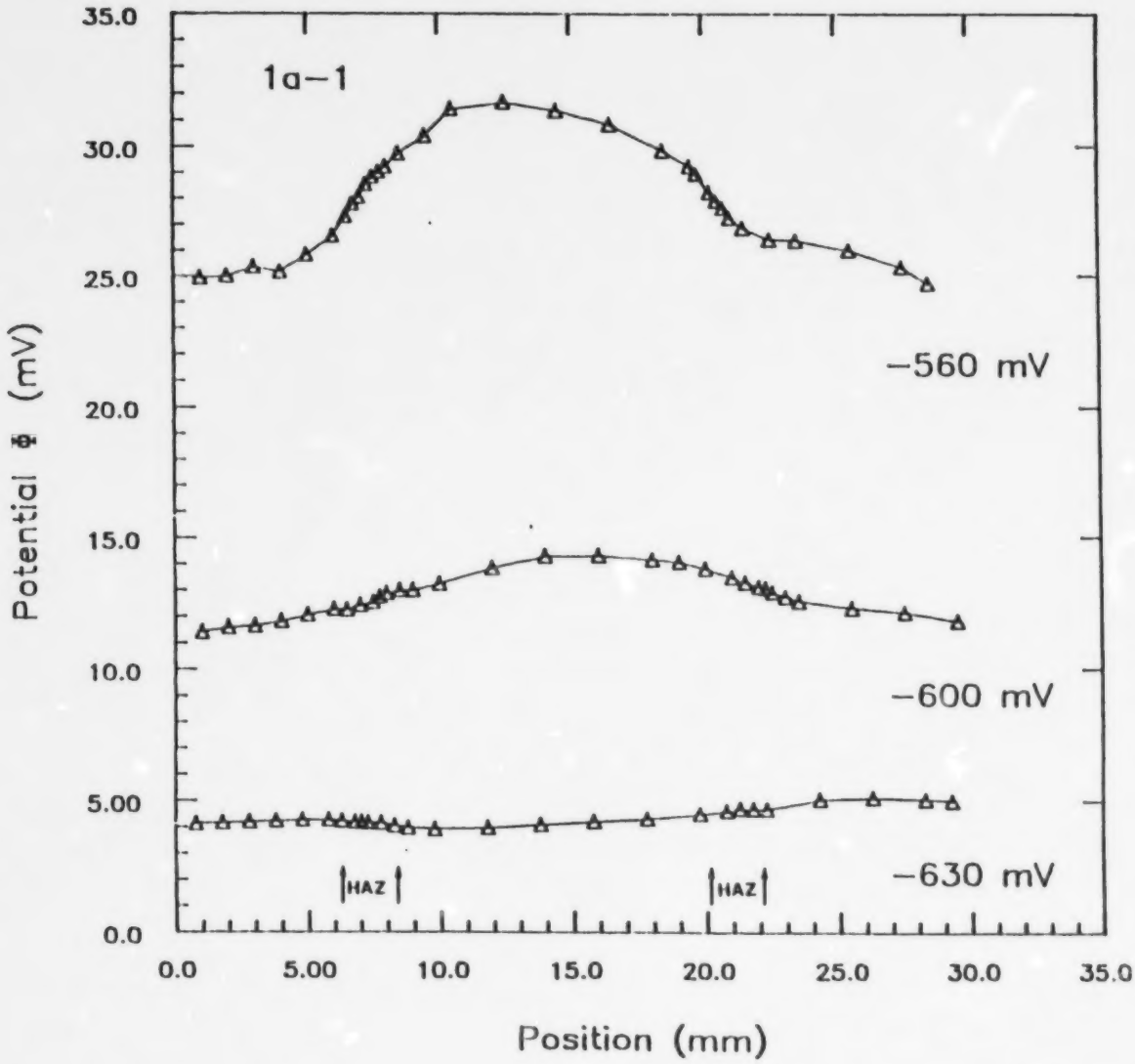

Figure 31. Position/Potential profile of weldment 1a-1 kJ/mm, as a function of weldment potential (vSCE) in 0.5 N NaCl.

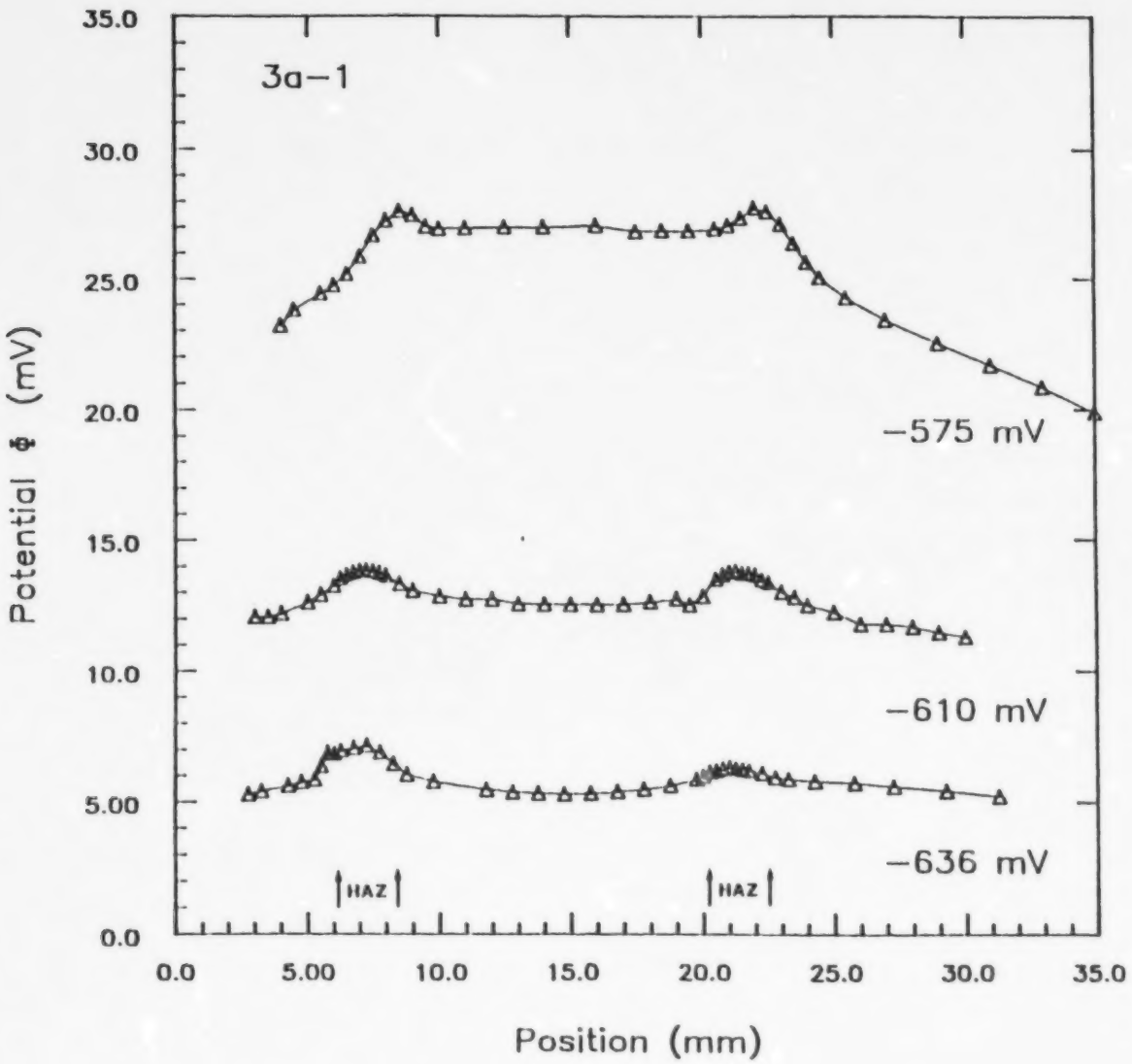

Figure 32. Position/Potential profile of weldment 3a-1 kJ/mm, as a function of Weldment potential (vSCE) in 0.5 N NaCl.

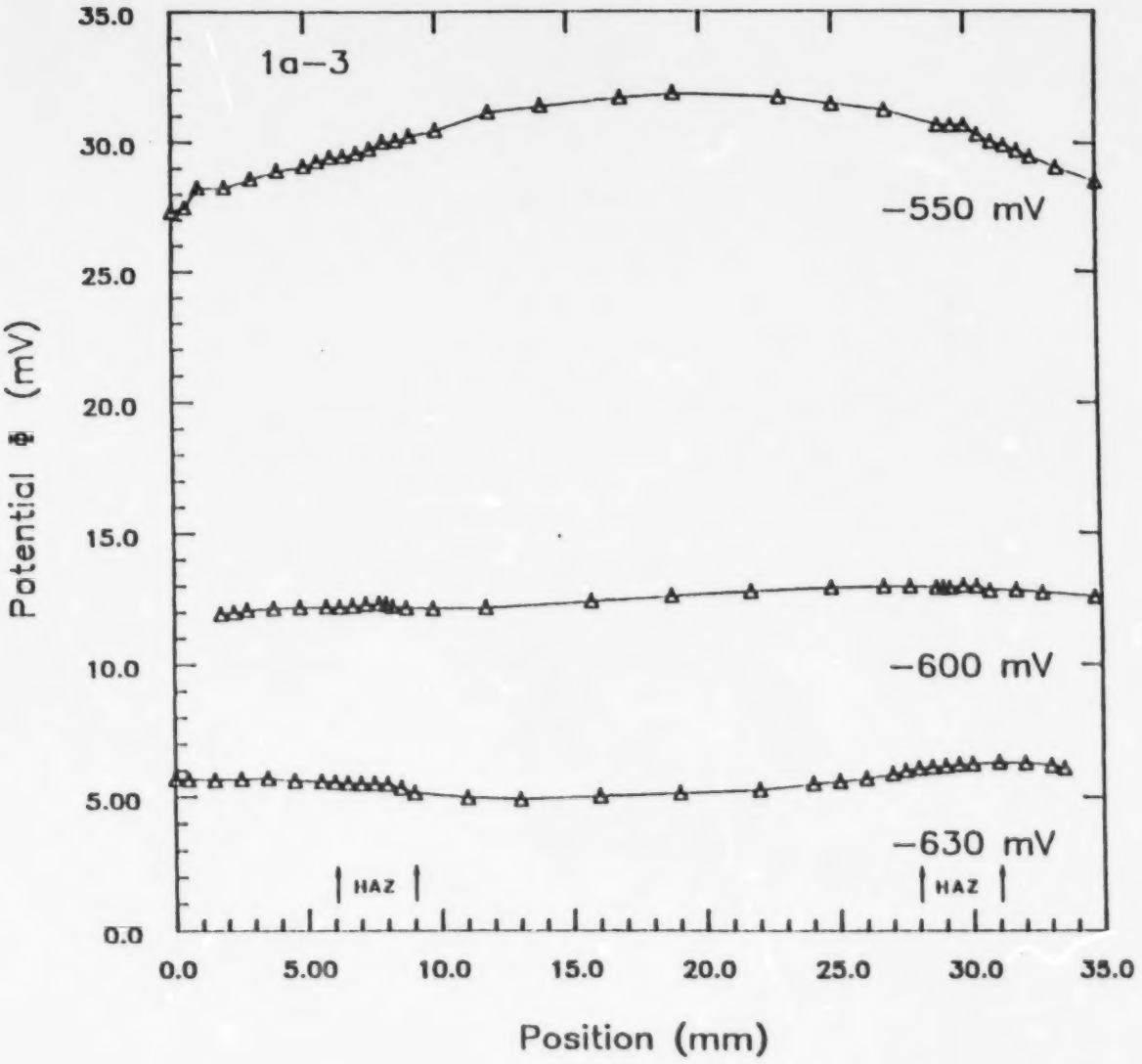

Figure 33. Position/Potential profile of weldment 1a-3 kJ/mm, as a function of Weldment potential (vSCE) in 0.5 N NaCl.

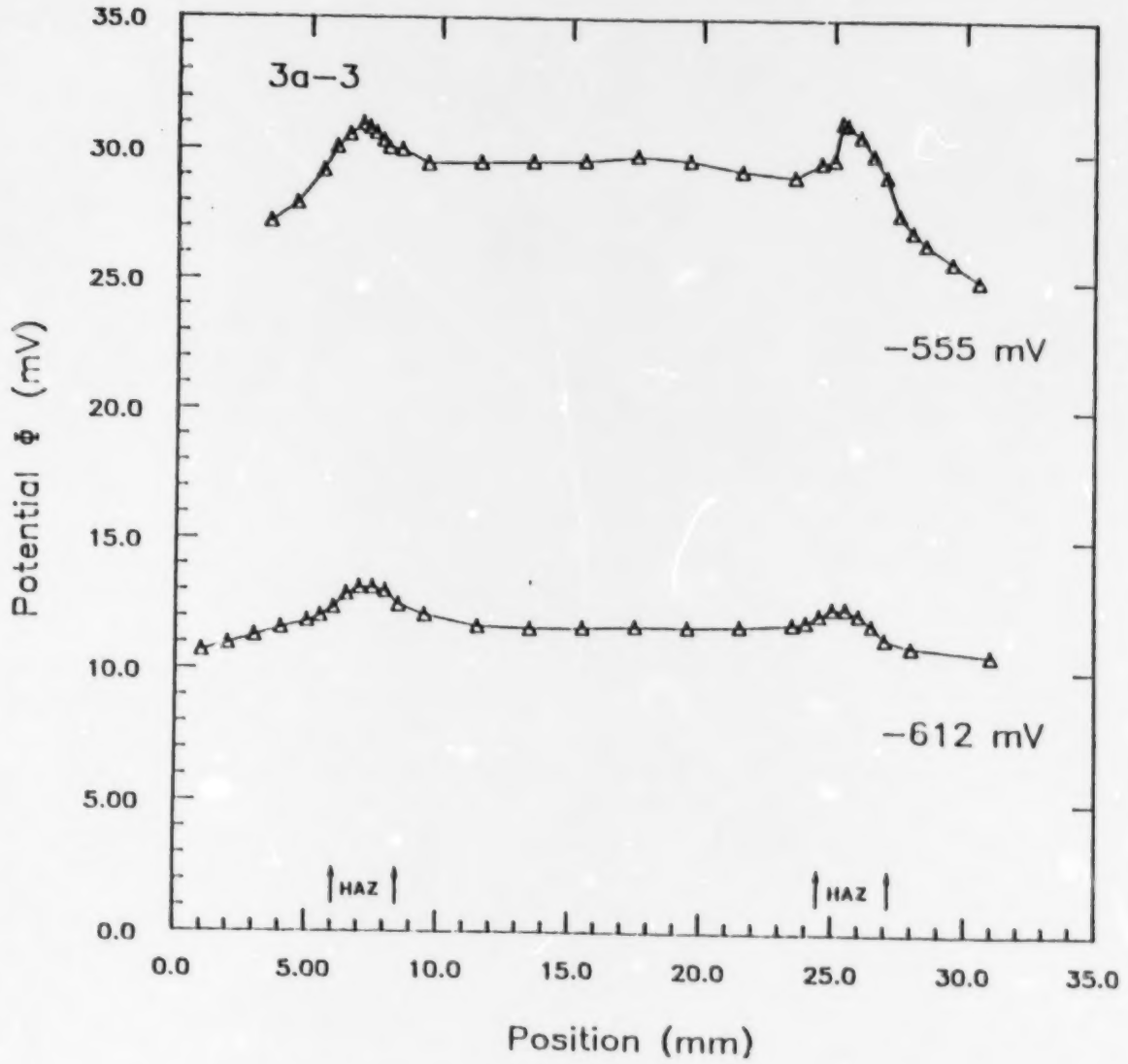

Figure 34. Position/Potential profile of Weldment 3a-3 kJ/mm, as a function of weldment potential (vSCE) in 0.5 N NaCl.

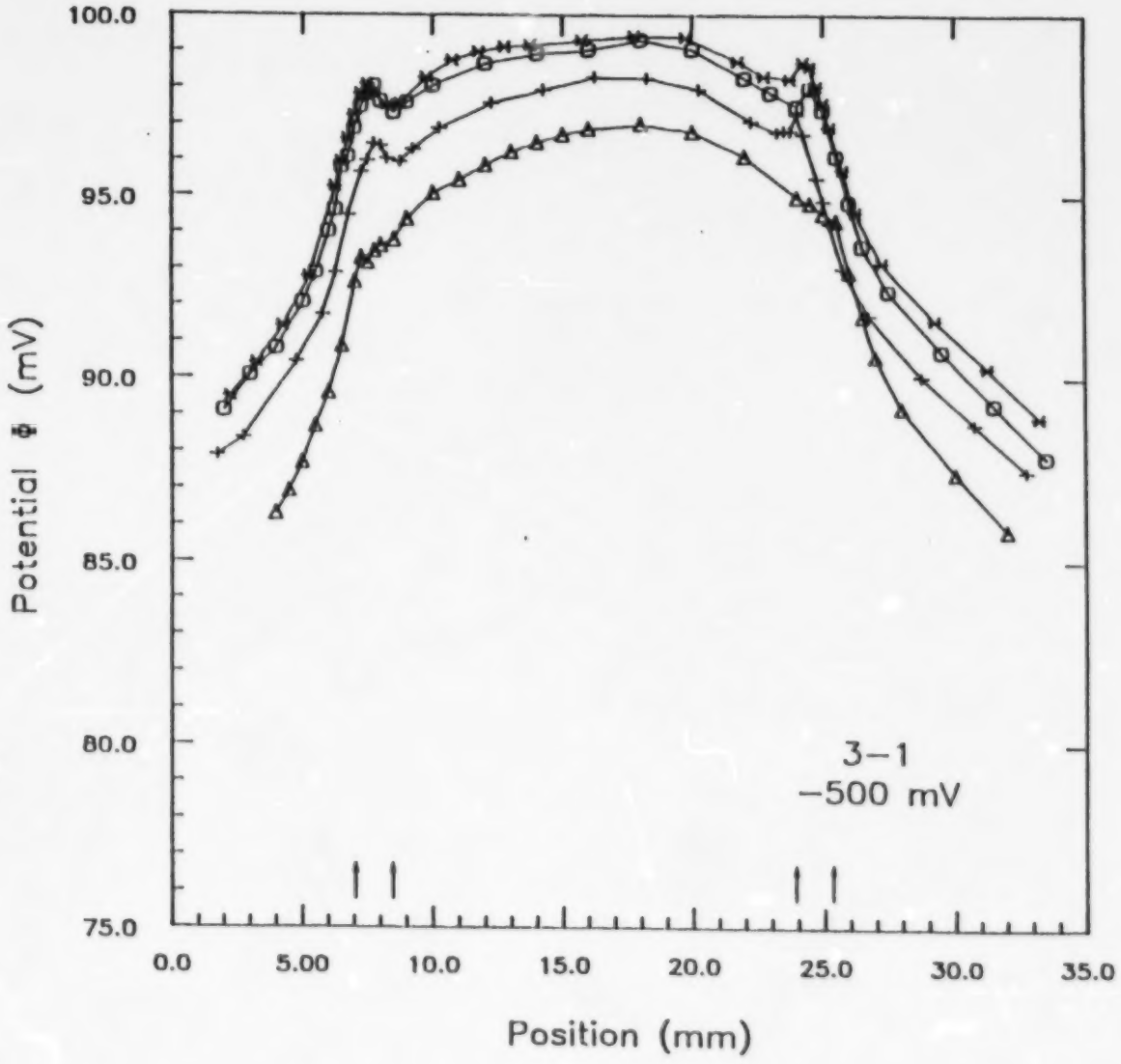

Figure 35. Position/Potential profile of weldment 3-1 kJ/mm as a function of time at a Weldment potential of -500 (vSCE) in 0.5 N NaCl. △ -2 hours, + -4 hours, * -6 hours, □ - 8 hours.

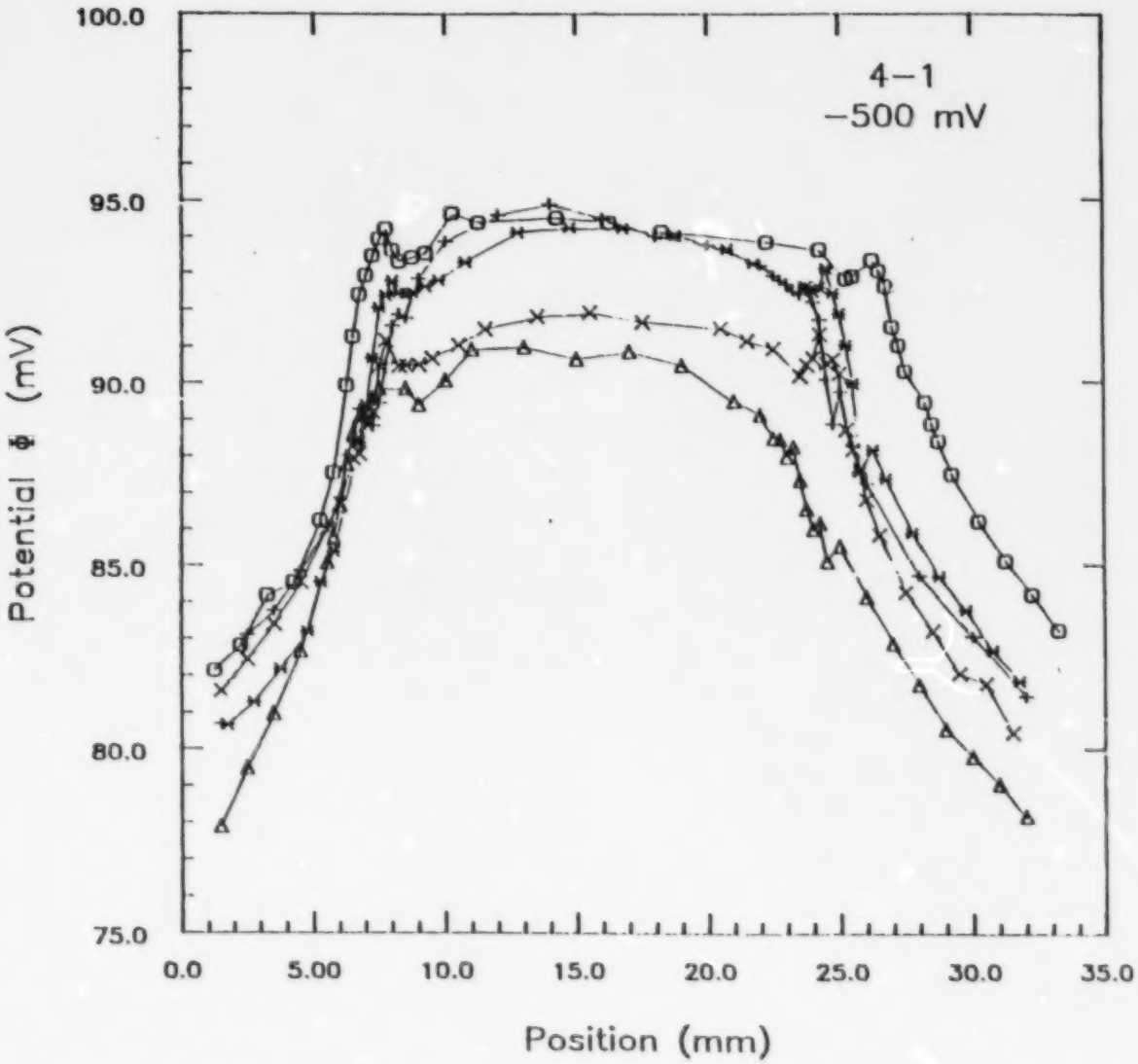

Figure 36. Position/Potential profile of weldment 4-1 kJ/mm as a function of time at a Weldment potential of -500 mV (vSCE) in 0.5 N NaCl. ∆ -2 hours, + -4 hours, * -8 hours, □ -12 hours, x -24 hours.

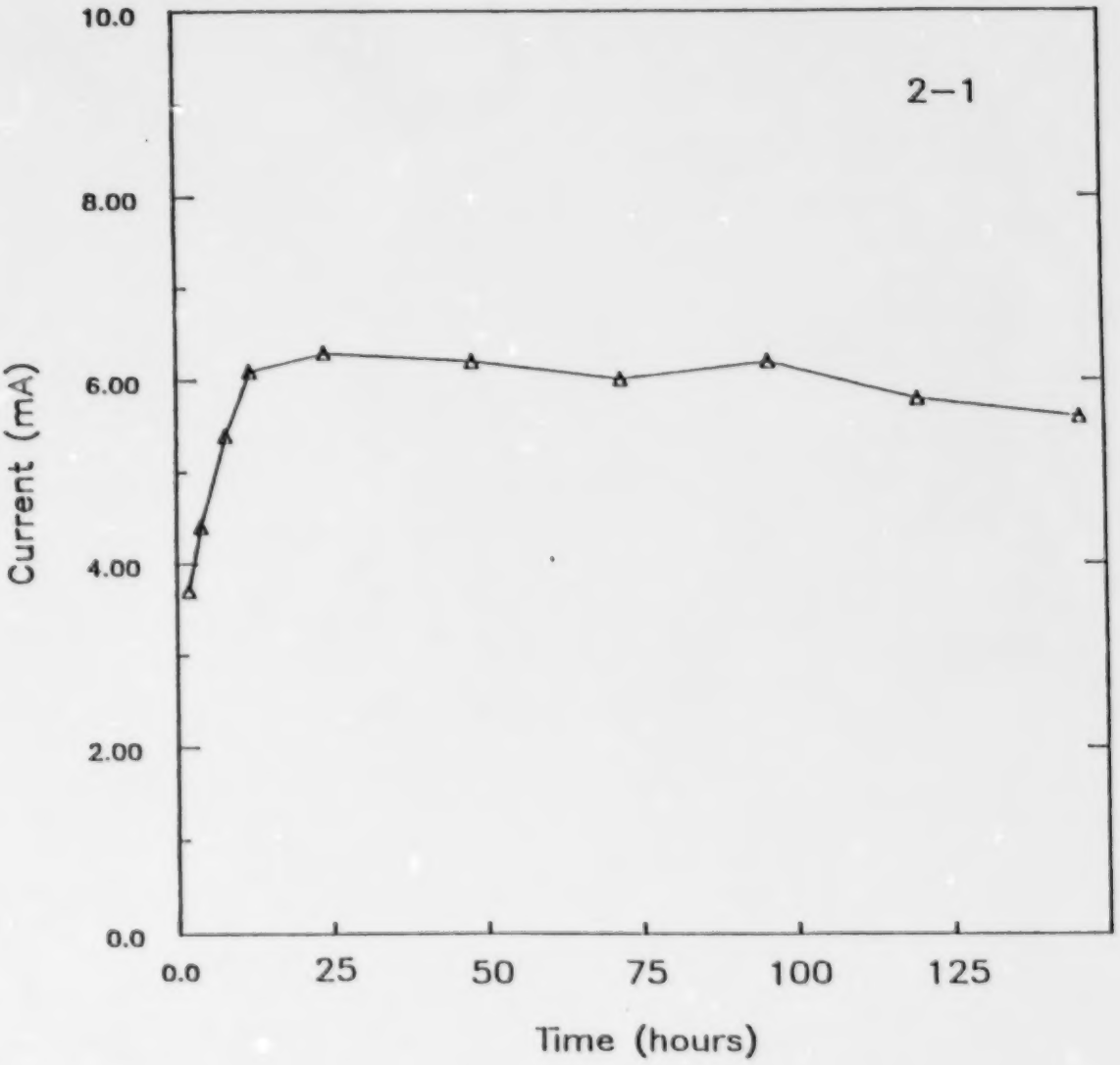

Figure 37. Graph of total current leaving the specimen versus time for weldment 2-1 kJ/mm at a potential of -600 mV (vSCE).

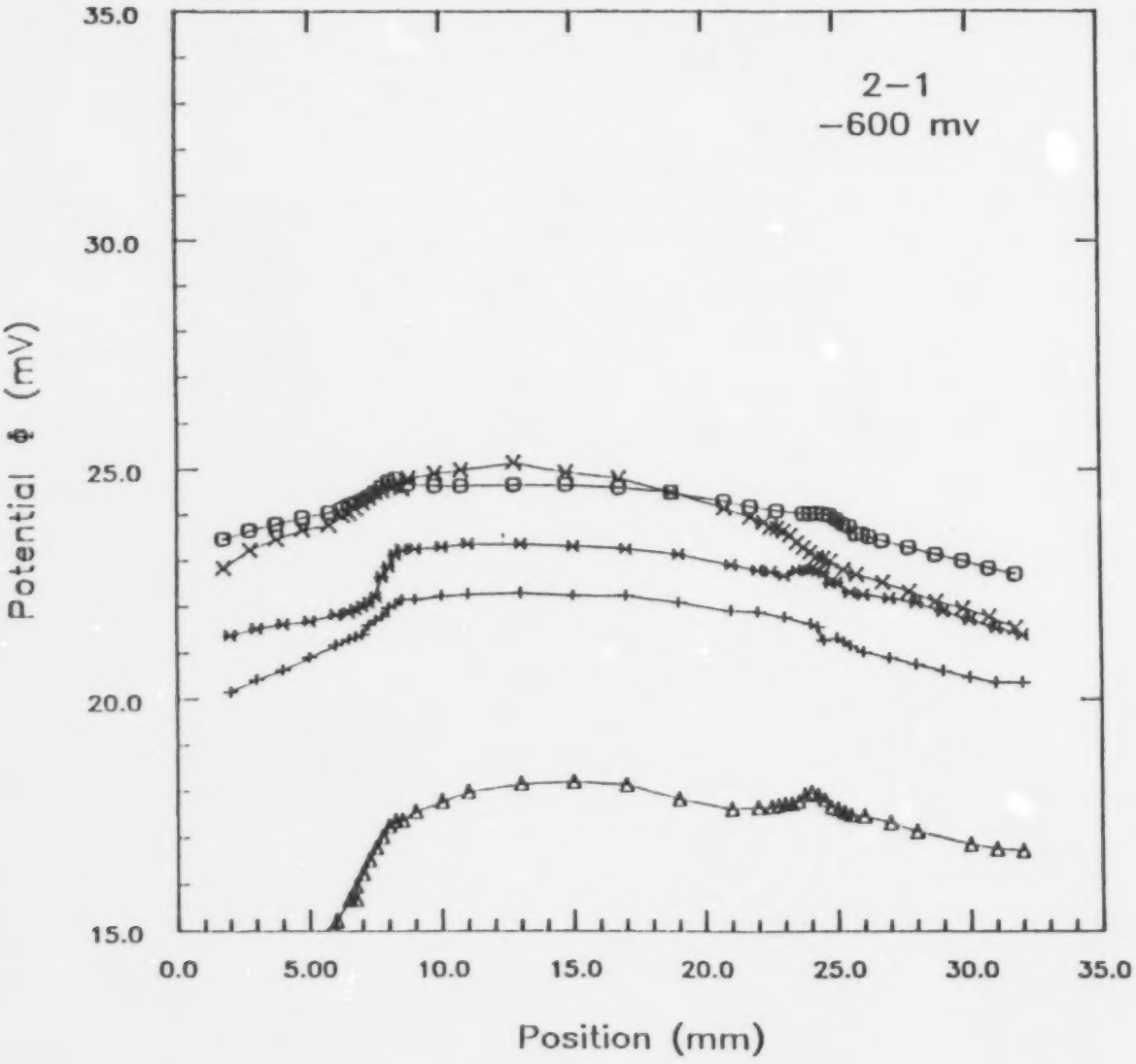

Figure 38a. Position/Potential profile of weldment 2-1 kJ/mm as a function of time at a potential of -600 mV (vSCE) in 0.5 N NaCl. Δ- 2 hours, + -4 hours, * -8 hours, ◘ -12 hours, x -24 hours.

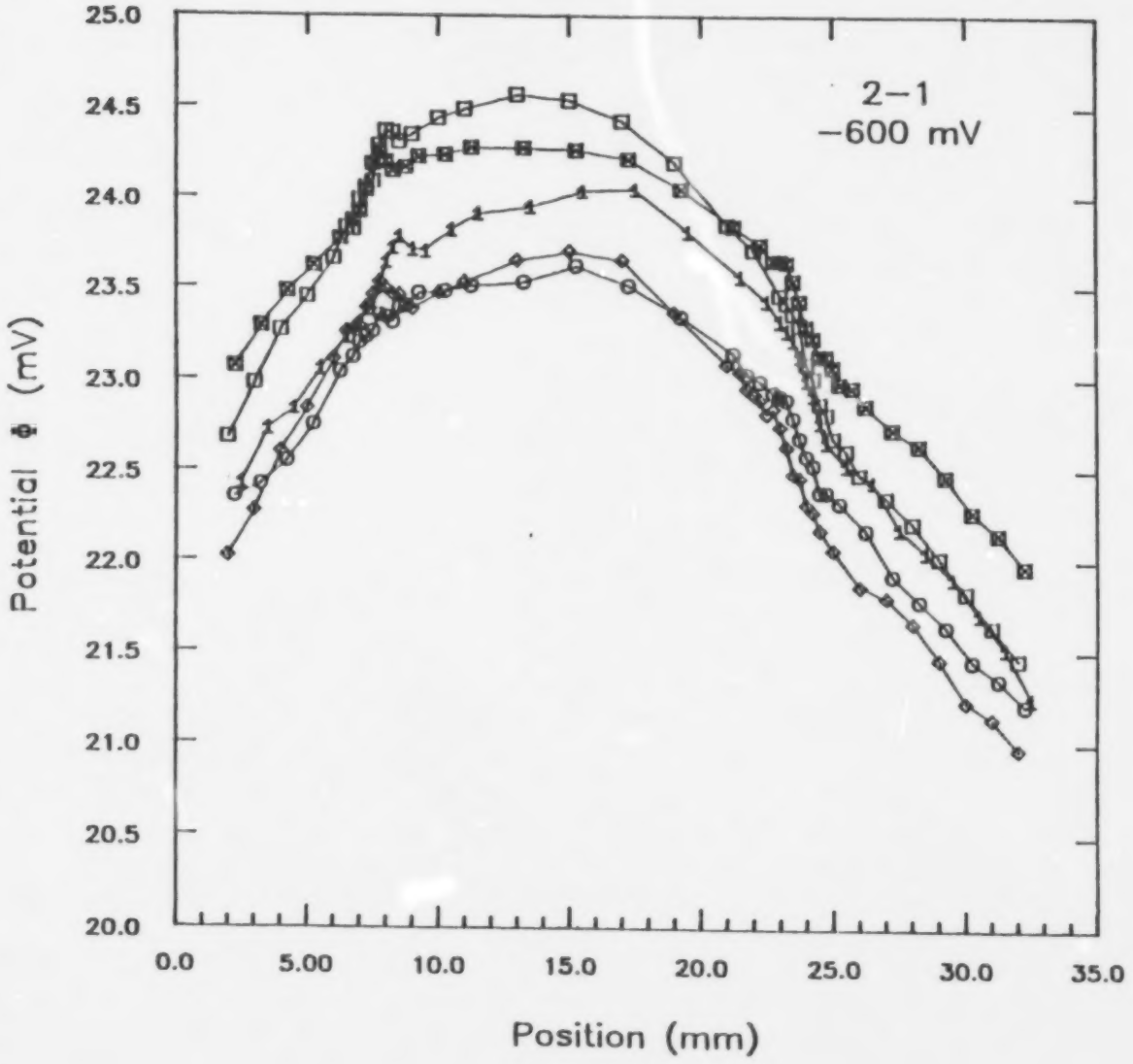

Figure 38b. Position/Potential profile of weldment 2-1 kJ/mm as a function of time at a potential of -600 mV (vSCE) in 0.5 N NaCl. □- 48 hours, ◊ -72 hours, ■- 96 hours, ◘ - 120 hours, 1 - 146 hours.

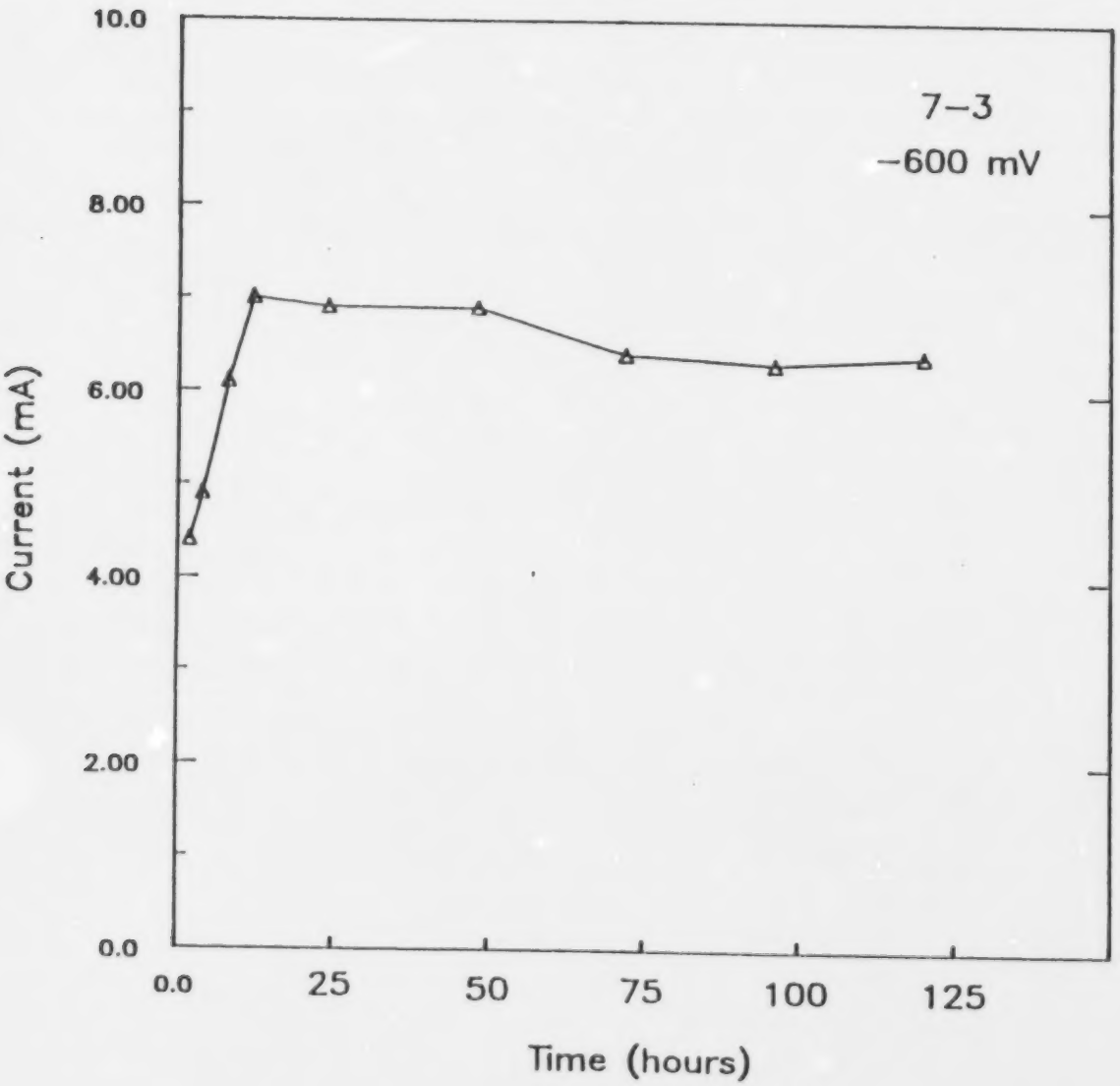

Figure 39. Graph of total current leaving the specimen versus time for weldment 7-3 kJ/mm at a potential of 600 mV.

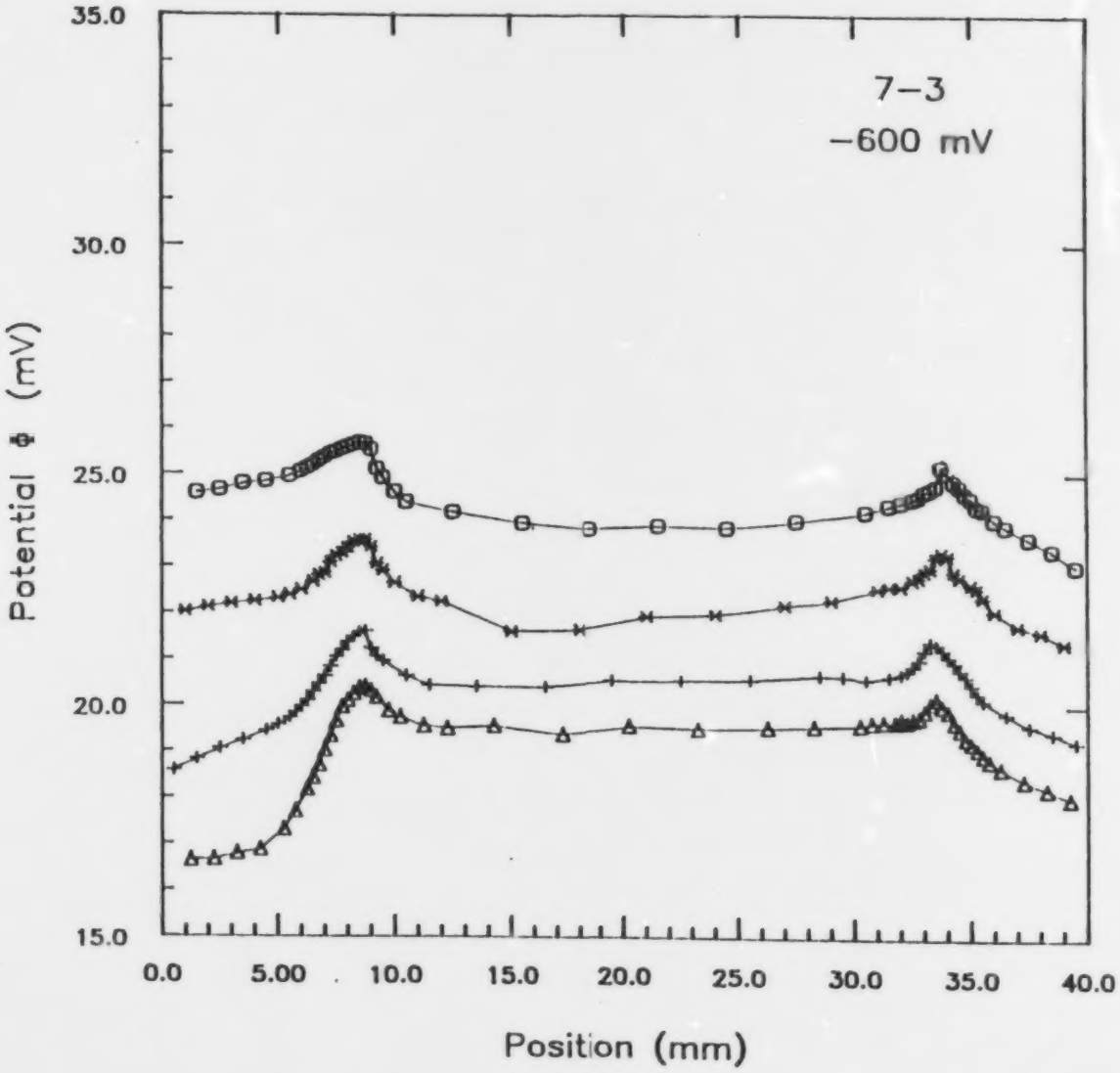

Figure 40a. Position/Potential profile of weldment 7-3 a function of time at a potential of -600 mV (vSCE) in 0.5 N NaCl. Δ - 2 hours, + - 4 hours, * -8 hours, ◘ - 12 hours.

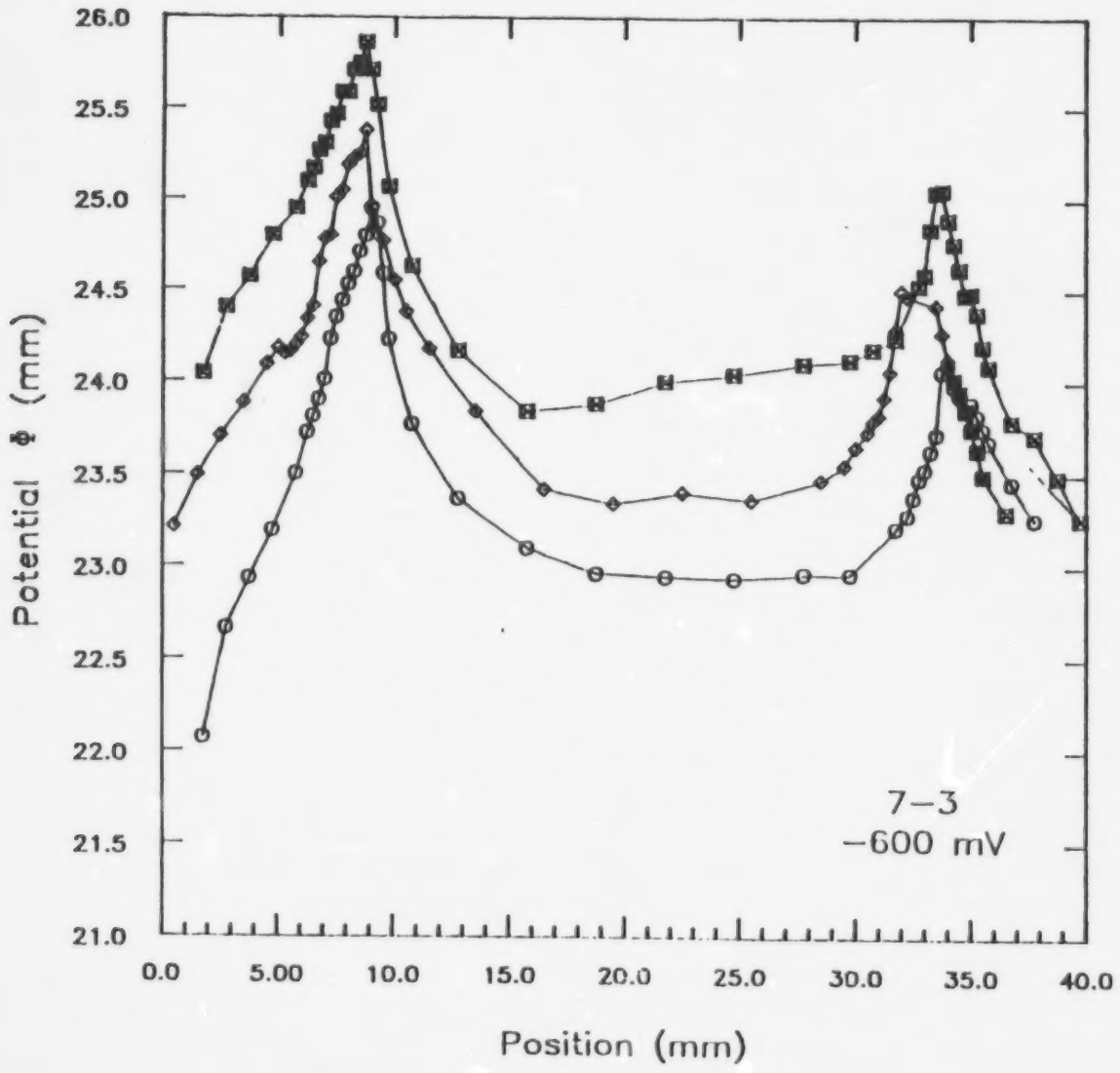

Figure 40b. Position/Potential profile of weldment 7-3 kJ/mm as a function of time at a potential of -600 mV (vSCE) in 0.5 N NaCl. ◇- 72 hours, ▣- 96 hours, o - 120 hours.

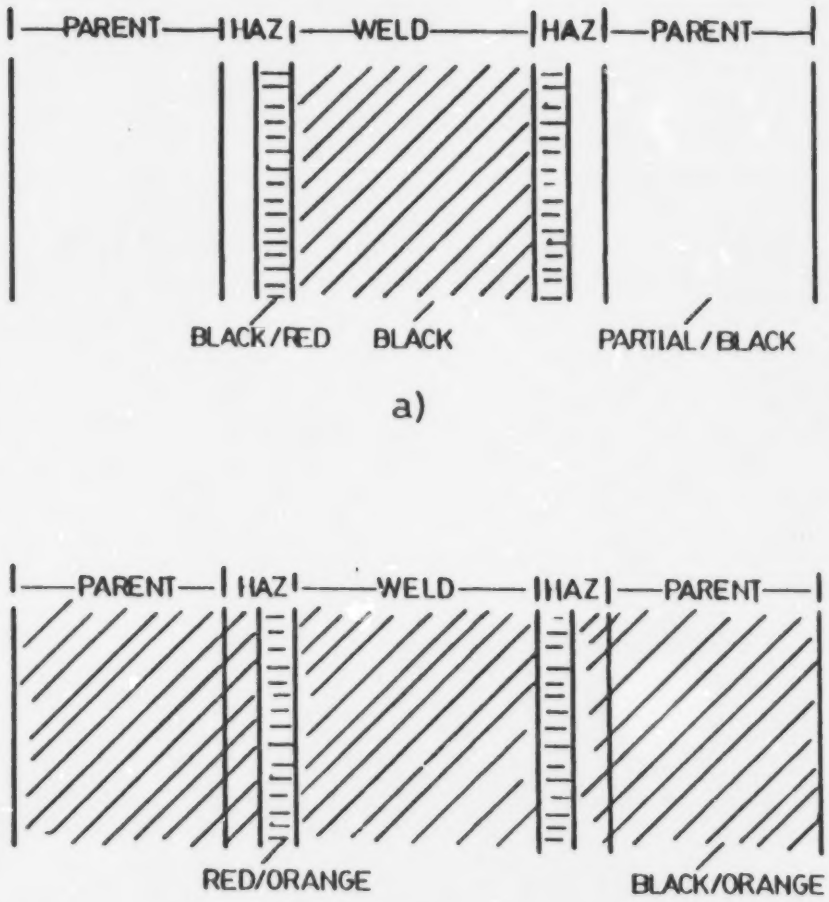

Figure 41. Schematic diagram of the surface of specimen 7-3 kJ/mm a) after 8 hours, b) 48 hours at a potential of -600 mV (vSCE) in 0.5 N NaCl.

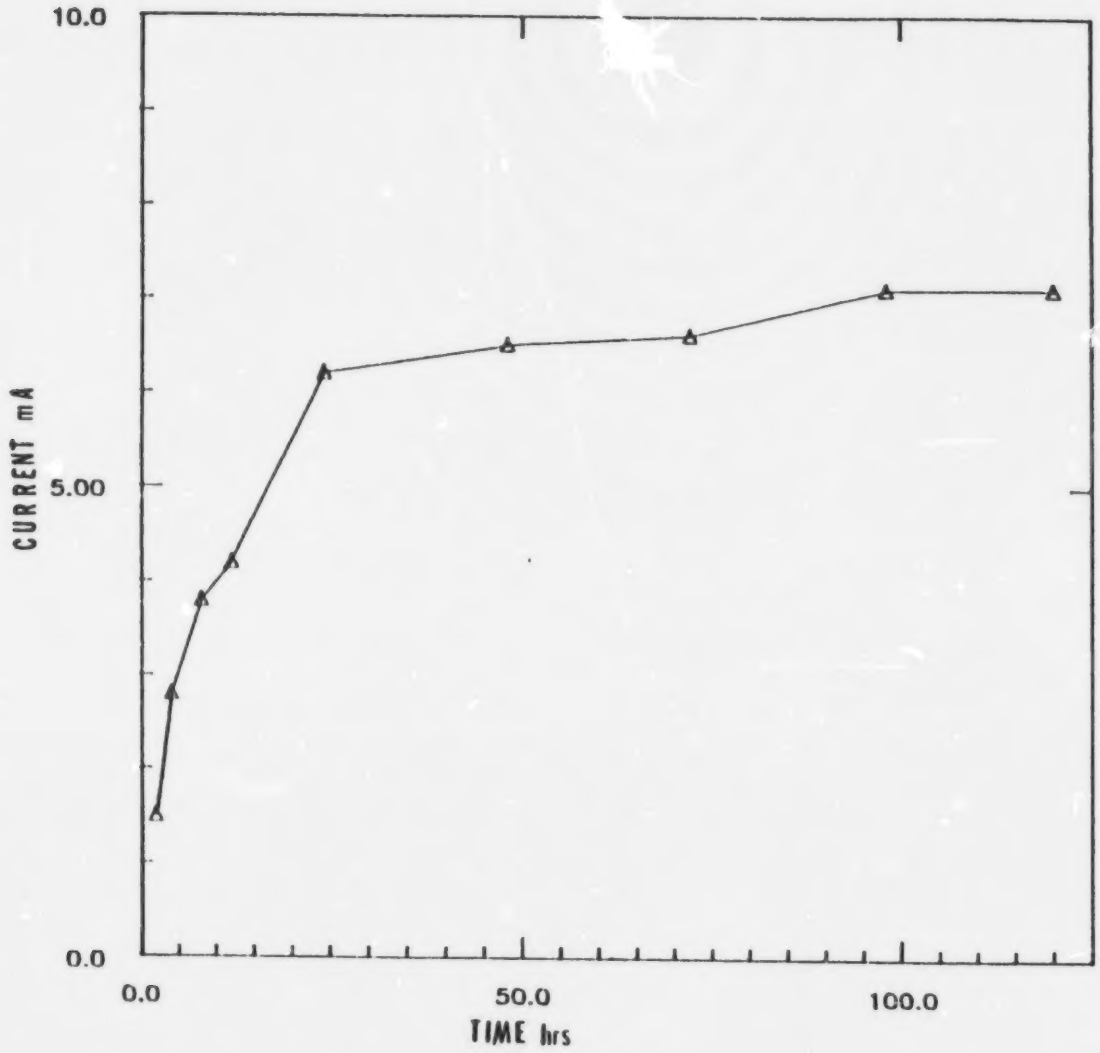

Figure 42. Graph of total current versus time for weldment 5-1 kJ/mm at a potential of -600 mV (vSCE) in 0.5 N NaCl.

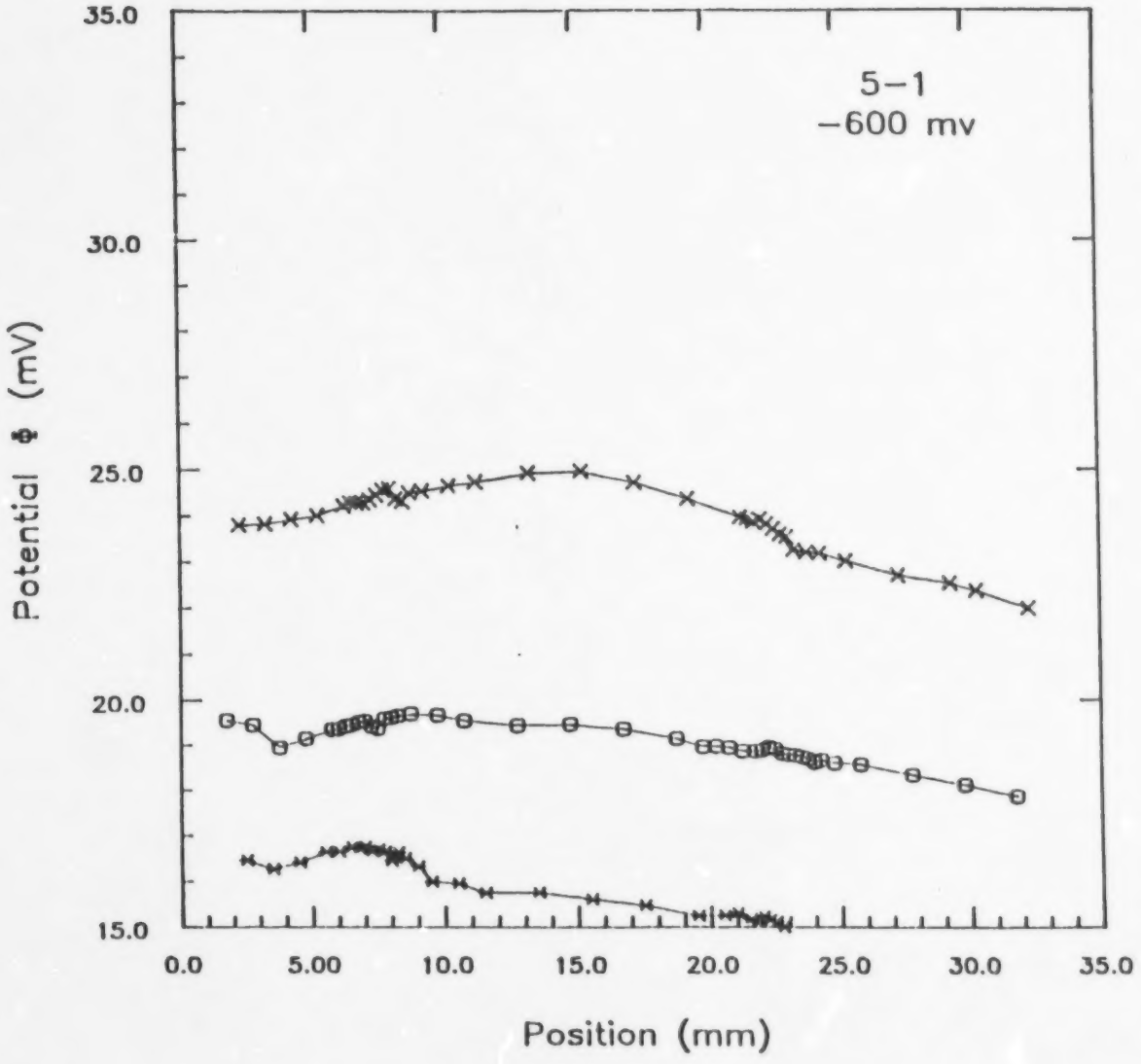

Figure 43a. Position/Potential profile as a function of time for weldment 5-1 kJ/mm at a potential of -600 mV (vSCE) in 0.5 N NaCl * - 8 hours, o - 12 hours, x - 24 hours.

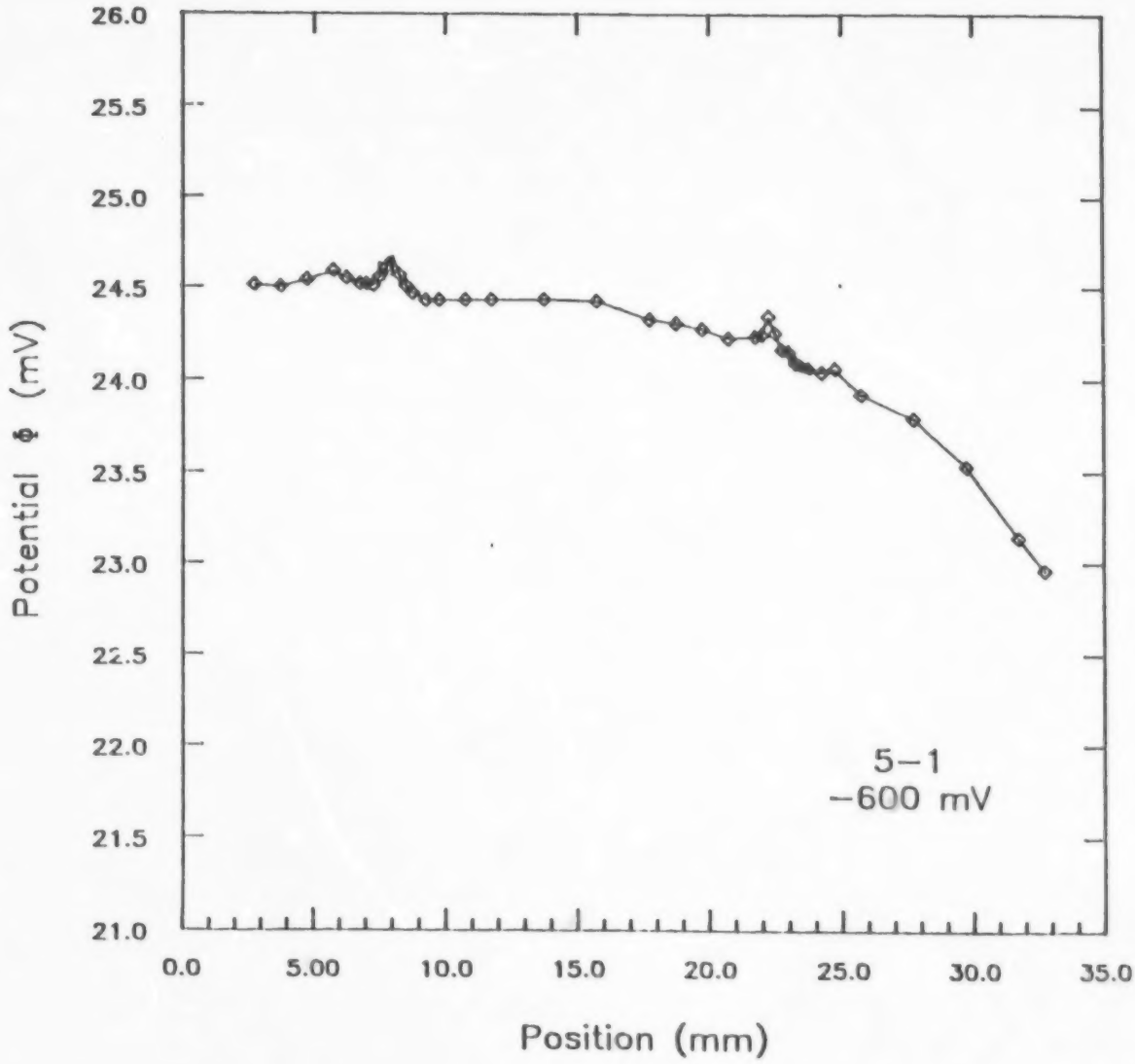

Figure 43b. Position/Potential profile for weldment 5-1 kJ/mm after 72 hours exposure at a potential of -600 mV in 0.5 N NaCl.

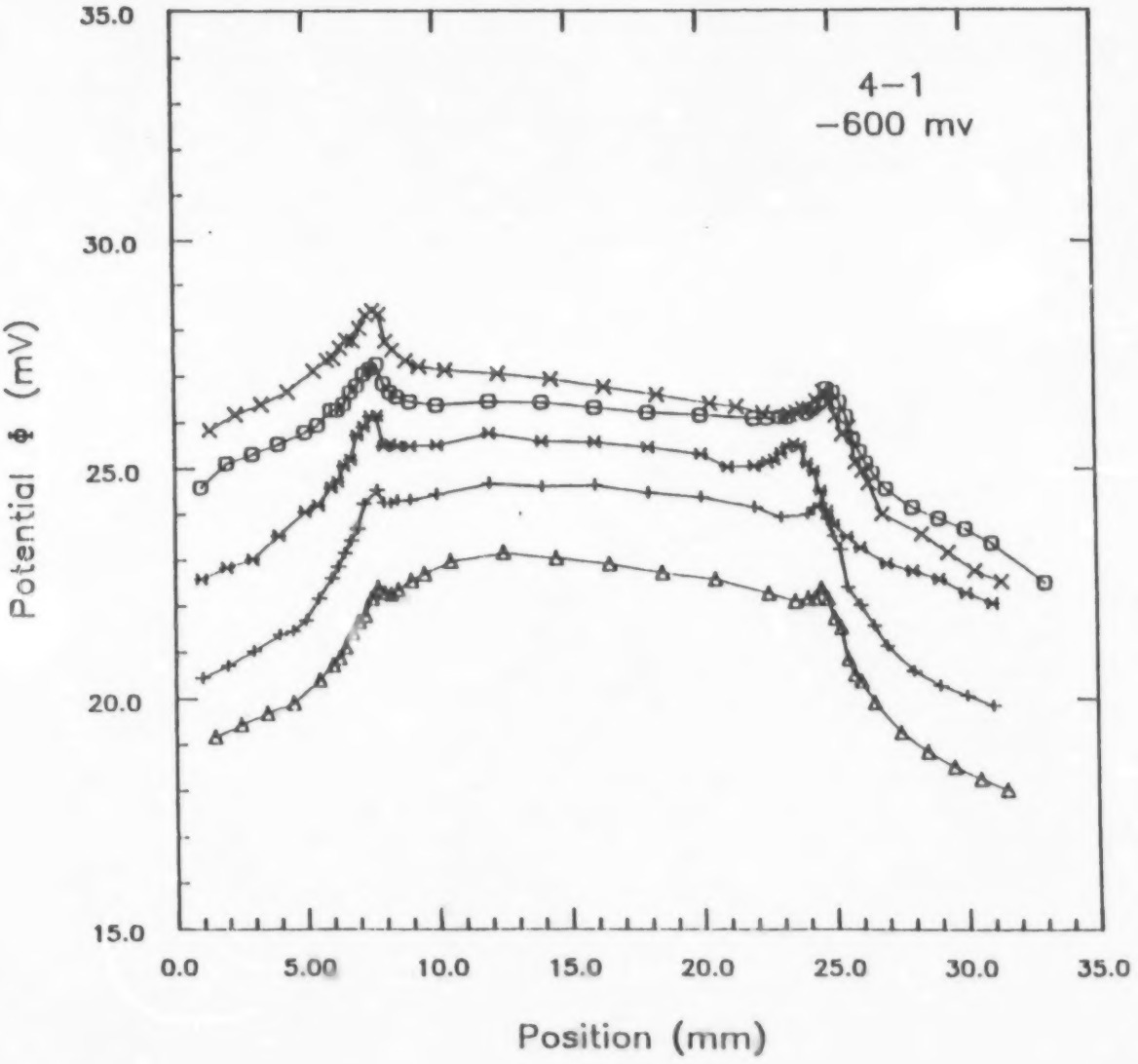

Figure 44. Position/Potential profile as a function of time for weldment 4-1 kJ/mm at a potential of -600 mV (vSCE) in 0.5 N NaCl. Δ - 2 hours,, + - 4 hours, * - 8 hours, ◘ - 12 hours, x - 24 hours.

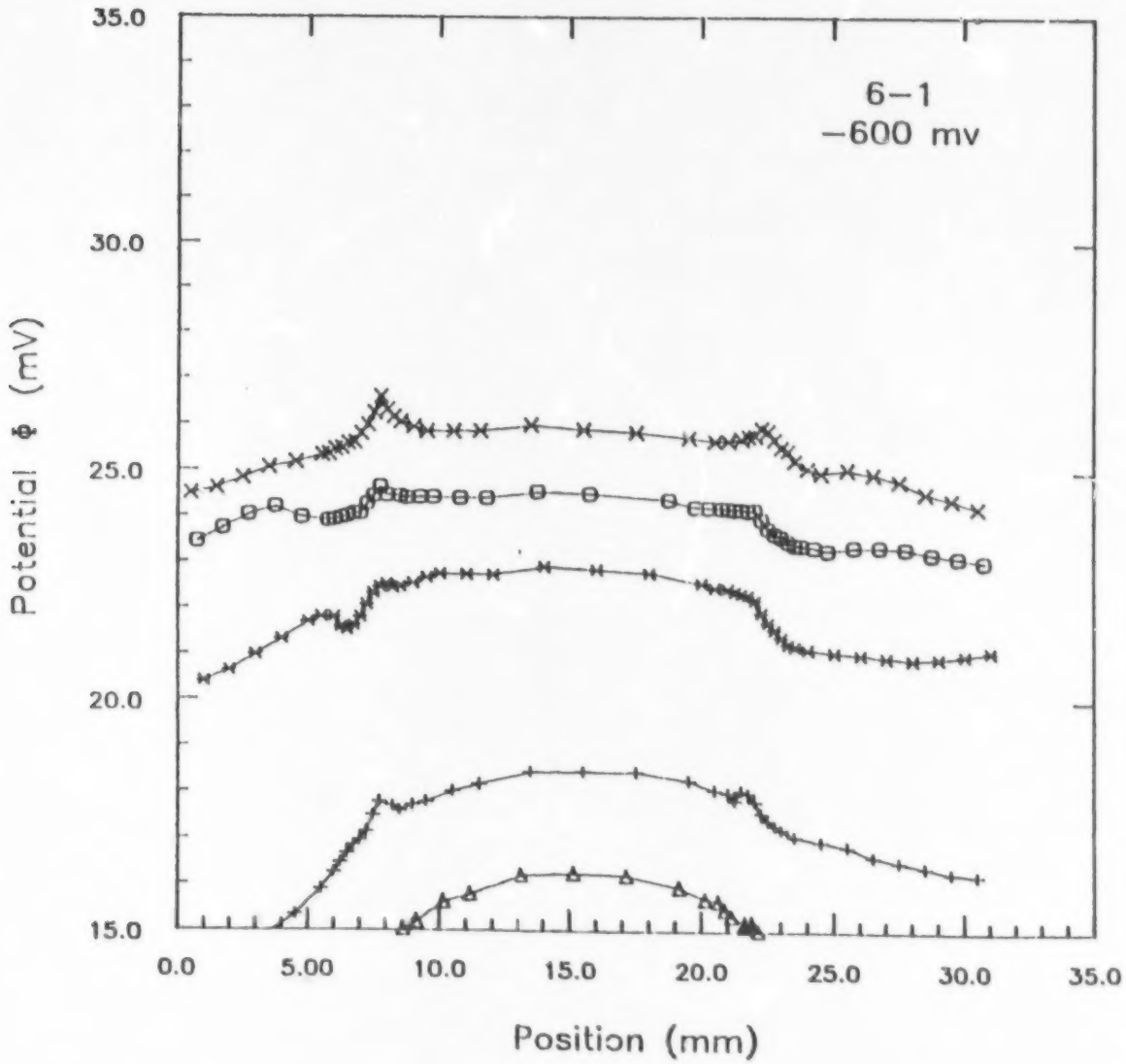

Figure 45. Position/Potential profile as a function of time for weldment 6-1 kJ/mm at a potential of -600 mV (vSCE) in 0.5 N NaCl. Δ- 2 hours, + - 4 hours, * - 8 hours, ◘ - 12 hours, x - 24 hours.

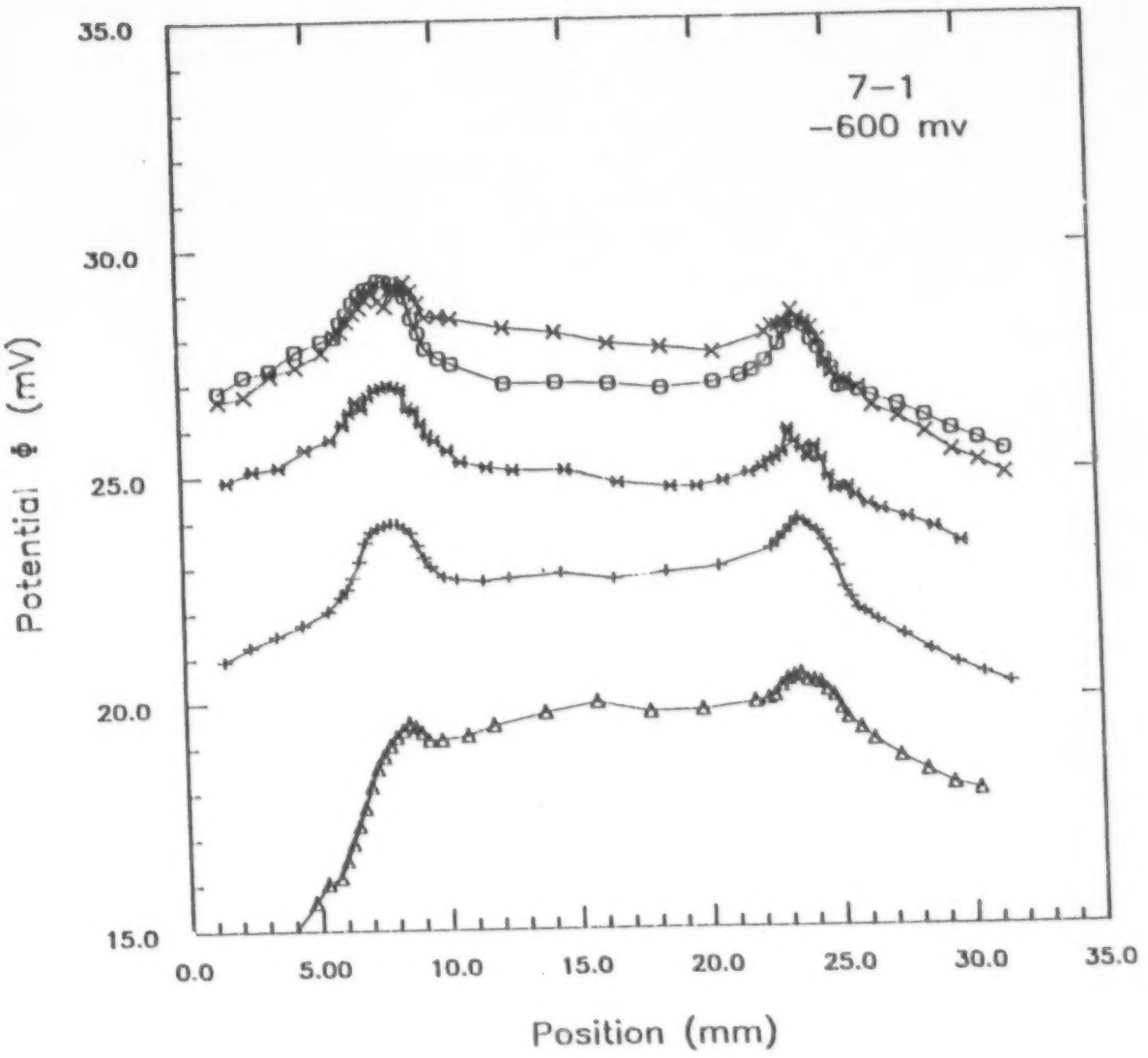

Figure 46. Position/Potential profile as a function of time for weldment 7-1 kJ/mm at a potential of -600 mV (vSCE) in 0.5 N NaCl. Δ- 2 hours, + - 4 hours, * - 8 hours, ◘ - 12 hours, x - 24 hours.

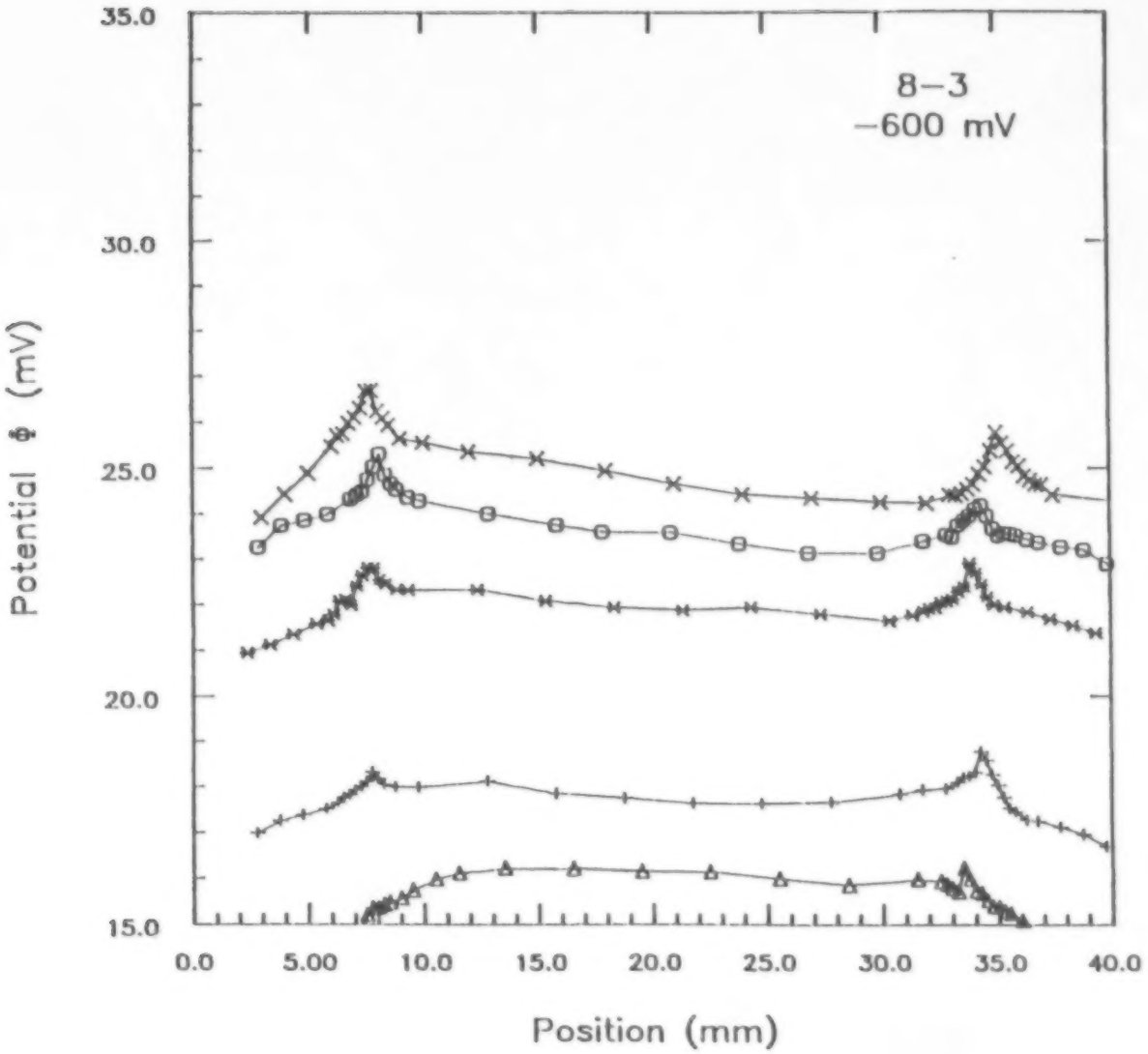

Figure 47. Position/Potential profile as a function of time for weldment 8-3 kJ/mm at a potential of -600 mV (vSCE) in 0.5 N NaCl. Δ- 2 hours, + - 4 hours, * - 8 hours, ◘ - 12 hours, x - 24 hours.

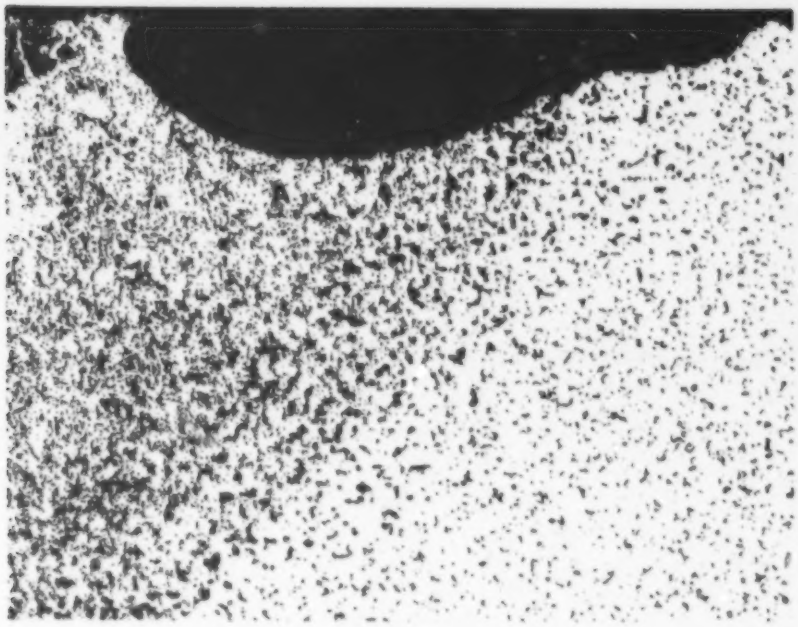

Figure 48a. As-corroded annealed 8-1 kJ/mm (40 X).

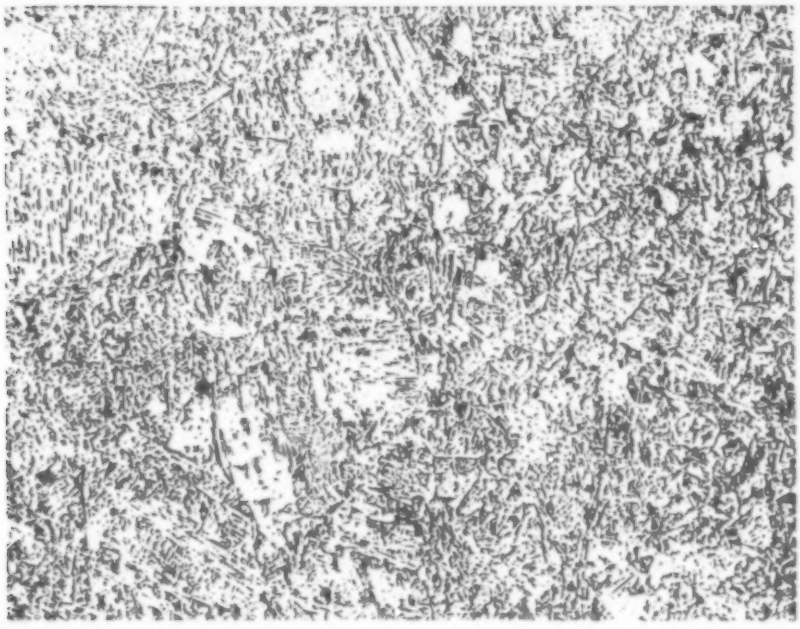

Figure 48b. Microstructure of Region A of Figure 48a for annealed 8-1 kJ/mm (200 X).

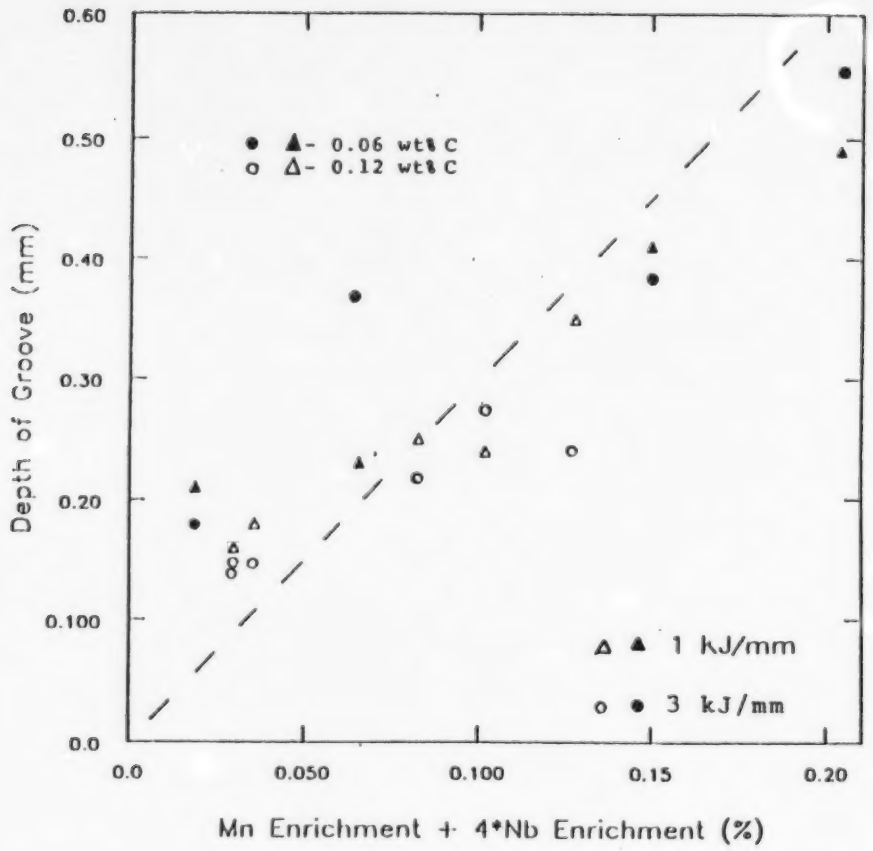

Figure 49. Graph of Mn Enrichment + 4*Nb Enrichment, assuming total dissolution of Nb(CN) in the lower carbon steels.

APPENDIX 1

Summary of Base Material Characterization

Table A1-1

Summary of Tensile Tests (Parallel Direction)

Parent Plate Steel Designation	Yield Stress (ksi) Upper	Yield Stress (ksi) 0.2% Offset	U.T.S. (ksi)	% Elongation
1	46.7	40.7	62.3	39.5
2	50.6	50.6	68.0	35
3	52.6	47.1	71.5	37
4	72.2	61.4	78.6	33.5
5	47.3	41.3	58.1	39.5
6	60.2	52.0	63.9	36.5
7	44.5	42.9	62.1	41.5
8	63.8	58.0	72.0	34.0

Table A 1-2

Summary of Tensile Tests (Transverse Direction)

Parent Plate Steel Designation	Yield Stress (ksi) Upper	Yield Stress (ksi) 0.2% Offset	U.T.S. (ksi)	% Elongation
1	40.9	39.7	62.9	38.5
2	49.7	48.7	67.4	33.5
3	49.4	46.0	71.3	35
4	60.6	58.5	79.2	27
5	46.0	38.2	57.1	40.5
6	56.8	49.7	64.4	32.5
7	45.7	42.9	62.3	41
8	57.9	57.2	72.6	34

Table A1-3

Charpy Impact Tests on Base Materials

(Energy Absorbed, J)

Steel	Test Temperature (°C)		
	-10	-50	-80
1	75, 76, 75	18, 8, 9	4, 4, 5
2	45, 38, 45	10, 7, 9	4, 3, 4
3	69, 59, 53	11, 16, 14	10, 8, 8
4	35, 40, 37	19, 12, 20	3, 5, 8
5	318, 318, 319	12, 11, 119	6, 4, 4
6	131, 105, 217	5, 4, 10	7, 5, 4
7	205, 222, 320	68, 85, 13	9, 5, 7
8	100, 115, 91	103, 36, 64	9, 6, 20

Table A1-4

Quantitative Microstructural Analysis of Base Materials

Steel	Quantitative Microstructure		Volumetric Grain Size	ASTM No.
	Ferrite %	Carbide %	(grain/mm^3)	
1	89	11	1.51×10^5	8.7
2	90	10	2.13×10^5	9.1
3	78	22	2.63×10^5	9.3
4	83	17	4.75×10^5	9.7
5	96	4	7.68×10^4	8.2
6	96	4	2.65×10^5	9.3
7	89	11	8.84×10^4	8.2
8	92	8	3.36×10^5	9.5

APPENDIX 2

Calculation of Mn Enrichment in the Ferrite Phase of the HAZ

Under slow cooling conditions, pearlite and ferrite are formed in C-Mn steels. The Mn content in the carbide phase is 4 times as much as in the ferrite phase (1,2). During the heating half of a welding thermal cycle, the phase transformation to γ-phase homogenized the Mn distribution. During the cooling half of a welding thermal cycle there is not sufficient time for proper Mn partition. Thus, the ferrite phase in the HAZ contain more Mn than in an equilibrium condition. This enrichment of soluble Mn, it is postulated, cause localized HAZ corrosion.

The following definitions and equations were used in the calculation:

n = Mn enrichment = $Mn_{HAZ} - Mn_{ferrite}$

$Mn_{HAZ} = Mn_{bulk}$

$Mn_{bulk} = X_{carbide} * Mn_{carbide} + X_{ferrite} * Mn_{ferrite}$

$Mn_{carbide} = 4 * Mn_{ferrite}$

where

Mn_{bulk} = wt% Mn in the alloy

Mn_{HAZ} = wt% Mn in the ferrite phase of HAZ

$Mn_{carbide}$ = wt% Mn in Fe_3C

$X_{carbide}$ = wt fraction Fe_3C

$X_{ferrite}$ = wt fraction ferrite

Hence for Steel 1, which contained 89% ferrite and 11% pearlite, and had 0.78% Mn, the following calculation can be performed:

$Mn_{bulk} = (X_{carbide})(Mn_{carbide}) + (X_{ferrite})(Mn_{ferrite})$

$0.78 = (0.11 \times 0.12^*)(4\ Mn_{ferrite}) + (0.89 + 0.11 \times 0.78)(Mn_{ferrite})$

$0.78 = 0.01132 \times 4\ Mn_{ferrite} + 0.9758\ Mn_{ferrite}$

$0.78 = 1.0286\ Mn_{ferrite}$

$Mn_{ferrite} = 0.758$

Therefore, the Mn enrichment is

$0.78 - 0.758 = 0.022$ wt%

Table A2-1 summarized the Mn enrichment calculated.

* Pearlite contains 12 wt% of carbide.

Table A2-1

Table of Depth of Corrosion vs. Mn Enrichment n

Sample	$X_{pearlite}$	$X_{ferrite}$	Depth	Enrichment
1	.11	.89	.16 mm	.83
1a	.15	.85	.18 mm	.84
2	.1	.9	.16 mm	.83
3	.22	.78	.24 mm	.10
3a	.26	.74	.35 mm	.13
4	.17	.83	.25 mm	.08
5	.04	.96	.21 mm	.01
6	.04	.96	.41 mm	.01
7	.11	.89	.23 mm	.06
8	.08	.92	.49 mm	.05

APPENDIX 3

ANALYSIS OF FACTORIAL EXPERIMENTS

The anodic dissolution tests were performed to determine the importance of different variables such as chemical composition and heat input (HI) on the anodic dissolution characteristics of the heat affected zone (HAZ) in steel weldments. The experiment had four factors, each at two levels. Thus, it was a 2^4 factorial experiment. The experimental factors and levels are given below:

Table A3-1

Experimental Factors and Levels

Symbol	Factors	Levels
A	Carbon content	A_0 = 0.12 - 0.13 %
		A_1 = 0.052 - 0.057 %
B	Heat input	B_0 = 1.2 kJ/mm
		B_1 = 3.0 kJ/mm
C	Manganese content	C_0 = 0.77 - 0.8 %
		C_1 = 1.39 - 1.54 %
D	Niobium content	D_0 = 0.002 %
		D_1 = 0.035 - 0.04 %

The maximum depth, due to anodic dissolution of the HAZ, measured are given in Table A3-2. In this table, the conventional symbol representing the treatment combination appears beside the resulting observation.

Estimation of main Effects and Interactions

A systematic method for estimation of main effects and interactions for two-level factorials was originally described by Yates[1]. The method described here applies to factorials, blocked factorials and fractionals for which there are 2^n observations.

For the systematic procedure using the Yates method, a table was constructed with n+2 columns. The data given in Table A3-3 is for a 2^4 factorial (n=4) experiment. Thus, Table A3-

3 has six columns. In the first column, the treatment combinations are given. The treatment combinations are listed in the "standard order" in the first column. In column 2, The observed yield or response is entered that corresponds to each of the treatment combinations listed in column 1. In the top half of column 3, the sums of consecutive pairs of entries in column 2 are entered in order. In bottom half of the column, the differences between the same consecutive pairs of entries are entered in order; the second entry minus the first entry etc. Columns 4, 5 and 6 are obtained in the same manner as column 3 - by obtaining in each case the sums and differences of the pairs in the preceding columns.

The estimated main effects and interactions in the last column (column n+2 = 6) also appear in a standard order; where T corresponds to the overall average effect; A to the main effect of factor A, AB to the interaction of factors A and B etc. Estimates of main effects and interactions were obtained by dividing the appropriate g by $2^{(n-1)}$ (i.e. 2^3).

Testing for Significance of Main Effects and Interactions

The significance of main effects and interactions identified by the methods described above was evaluated in the following manner. Let the level of significance $\alpha = 0.05$. The sums of squares of the g's corresponding to interactions of three or more factors in Table A3-3 is:

$$g^2_{ABC} + g^2_{ABD} + g^2_{ACD} + g^2_{BCD} + g^2_{ABCD} = 0.1109$$

To obtain s^2, the sum of squares was divided by $2^n\nu$, where ν was the number of interactions included. In a 2^n factorial, the number of third and higher interactions were $2^n - (n^2 + n + 2)/2$.

$$\text{When } n = 4,\ \nu = 5,\ 2^n\nu = 80.$$
$$s^2 = 0.1109/80 = 0.001386$$
$$s = 0.037$$

Consulting Table A3-4, for $\nu = 5$ and for $t_{(1-\alpha/2)} = t_{0.975}$, one can compute:

$$w = (2^n)^{1/2}\, t_{(1-\alpha/2)}\, s$$
$$= 4\ (2.571)\ (0.037) = 0.38.$$

For any main effect or interaction X, if the absolute value g_X was greater than w, it was concluded that X was different from zero i.e. the effect of X was significant. From Table A3-3,

$$g_A = 1.25,\ g_C = 0.79,\ g_D = 0.81,\ g_{AD} = 0.85 > w = 0.38.$$

Therefore the main effects of carbon (A), manganese (C), niobium (D) and the interaction of carbon combined with niobium (AD) were believed to be significant in the anodic dissolution of HAZ.

Reference

1. Metals Hand Book, Ninth edition, Vol. 8, "Mechanical Testing", 1985, p. 653.

Table A3-2. Example of test data from a factorial experiment.

Maximum depth due to anodic dissolution of the HAZ, mm.

		A_0 (C_0)		A_1 (C_1)	
		B_0 (HI_0)	B_1 (HI_1)	B_0 (HI_0)	B_1 (HI_1)
C_0 (Mn_0)	D_0 (Nb_0)	0.16 (1)	0.14 b	0.21 a	0.18 ab
	D_1 (Nb_1)	0.16 a	0.15 bd	0.41 ad	0.36 abd
C_1 (Mn_1)	D_0 (Nb_0)	0.24 c	0.24 bc	0.23 ac	0.36 abc
	D_1 (Nb_1)	0.25 cd	0.20 bcd	0.49 acd	0.55 abcd

Table A3-3. Yates method of analysis using data from Table A3-2.

Treatment combination.	Response (yield)				
1	2	3	4	5	6
(1)	0.16	0.37	0.69	1.76	4.33 = g_T9
a	0.21	0.32	1.07	2.57	1.25 = g_A
b	0.14	0.47	1.08	0.20	0.03 = g_B
ab	0.18	0.60	1.49	1.05	0.19 = g_{AB}
c	0.24	0.57	0.09	0.08	0.79 = g_C
ac	0.23	0.51	0.11	- 0.05	0.15 = g_{AC}
bc	0.24	0.74	0.46	0.12	0.25 = g_{BC}
abc	0.36	0.75	0.59	0.07	0.29 = g_{ABC}
d	0.16	0.05	- 0.05	0.38	0.81 = g_D
ad	0.41	0.04	0.13	0.41	0.85 = g_{AD}
bd	0.15	- 0.01	- 0.06	0.02	- 0.13 = g_{BD}
abd	0.36	0.12	0.01	0.13	- 0.05 = g_{ABD}
cd	0.25	0.25	- 0.01	0.18	0.03 = g_{CD}
acd	0.49	0.21	0.13	0.07	0.11 = g_{ACD}
bcd	0.20	0.24	- 0.04	0.14	- 0.11 = g_{BCD}
abcd	0.55	0.35	0.11	0.15	0.01 = g_{ABCD}
Total	4.33				
Sum of Squares	1.4103				22.5648

Table A3-4. Percentiles of the t Distribution

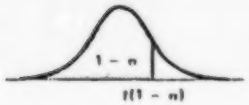

Entry is $t(1-\alpha, \nu)$, where $P[t(\nu) \le t(1-\alpha, \nu)] = 1-\alpha$.

	1 − α												
ν	0.55	0.60	0.65	0.70	0.75	0.80	0.85	0.90	0.95	0.975	0.99	0.995	0.9995
1	0.158	0.325	0.510	0.727	1.000	1.376	1.963	3.078	6.314	12.706	31.821	63.657	636.619
2	0.142	0.289	0.445	0.617	0.816	1.061	1.386	1.886	2.920	4.303	6.965	9.925	31.598
3	0.137	0.277	0.424	0.584	0.765	0.978	1.250	1.638	2.353	3.182	4.541	5.841	12.924
4	0.134	0.271	0.414	0.569	0.741	0.941	1.190	1.533	2.132	2.776	3.747	4.604	8.610
5	0.132	0.267	0.408	0.559	0.727	0.920	1.156	1.476	2.015	2.571	3.365	4.032	6.869
6	0.131	0.265	0.404	0.553	0.718	0.906	1.134	1.440	1.943	2.447	3.143	3.707	5.959
7	0.130	0.263	0.402	0.549	0.711	0.896	1.119	1.415	1.895	2.365	2.998	3.499	5.408
8	0.130	0.262	0.399	0.546	0.706	0.889	1.108	1.397	1.860	2.306	2.896	3.355	5.041
9	0.129	0.261	0.398	0.543	0.703	0.883	1.100	1.383	1.833	2.262	2.821	3.250	4.781
10	0.129	0.260	0.397	0.542	0.700	0.879	1.093	1.372	1.812	2.228	2.764	3.169	4.587
11	0.129	0.260	0.396	0.540	0.697	0.876	1.088	1.363	1.796	2.201	2.718	3.106	4.437
12	0.128	0.259	0.395	0.539	0.695	0.873	1.083	1.356	1.782	2.179	2.681	3.055	4.318
13	0.128	0.259	0.394	0.538	0.694	0.870	1.079	1.350	1.771	2.160	2.650	3.012	4.221
14	0.128	0.258	0.393	0.537	0.692	0.868	1.076	1.345	1.761	2.145	2.624	2.977	4.140
15	0.128	0.258	0.393	0.536	0.691	0.866	1.074	1.341	1.753	2.131	2.602	2.947	4.073
16	0.128	0.258	0.392	0.535	0.690	0.865	1.071	1.337	1.746	2.120	2.583	2.921	4.015
17	0.128	0.257	0.392	0.534	0.689	0.863	1.069	1.333	1.740	2.110	2.567	2.898	3.965
18	0.127	0.257	0.392	0.534	0.688	0.862	1.067	1.330	1.734	2.101	2.552	2.878	3.922
19	0.127	0.257	0.391	0.533	0.688	0.861	1.066	1.328	1.729	2.093	2.539	2.861	3.883
20	0.127	0.257	0.391	0.533	0.687	0.860	1.064	1.325	1.725	2.086	2.528	2.845	3.850
21	0.127	0.257	0.391	0.532	0.686	0.859	1.063	1.323	1.721	2.080	2.518	2.831	3.819
22	0.127	0.256	0.390	0.532	0.686	0.858	1.061	1.321	1.717	2.074	2.508	2.819	3.792
23	0.127	0.256	0.390	0.532	0.685	0.858	1.060	1.319	1.714	2.069	2.500	2.807	3.767
24	0.127	0.256	0.390	0.531	0.685	0.857	1.059	1.318	1.711	2.064	2.492	2.797	3.745
25	0.127	0.256	0.390	0.531	0.684	0.856	1.058	1.316	1.708	2.060	2.485	2.787	3.725
26	0.127	0.256	0.390	0.531	0.684	0.856	1.058	1.315	1.706	2.056	2.479	2.779	3.707
27	0.127	0.256	0.389	0.531	0.684	0.855	1.057	1.314	1.703	2.052	2.473	2.771	3.690
28	0.127	0.256	0.389	0.530	0.683	0.855	1.056	1.313	1.701	2.048	2.467	2.763	3.674
29	0.127	0.256	0.389	0.530	0.683	0.854	1.055	1.311	1.699	2.045	2.462	2.756	3.659
30	0.127	0.256	0.389	0.530	0.683	0.854	1.055	1.310	1.697	2.042	2.457	2.750	3.646
40	0.126	0.255	0.388	0.529	0.681	0.851	1.050	1.303	1.684	2.021	2.423	2.704	3.551
60	0.126	0.254	0.387	0.527	0.679	0.848	1.046	1.296	1.671	2.000	2.390	2.660	3.460
120	0.126	0.254	0.386	0.526	0.677	0.845	1.041	1.289	1.658	1.980	2.358	2.617	3.373
∞	0.126	0.253	0.385	0.524	0.674	0.842	1.036	1.282	1.645	1.960	2.326	2.576	3.291